XRF and RIS for semi-quantitative sub-surface layer detection and composition analysis of easel paintings

Luís Manuel de Almeida Nieto

September 2020

Abstract

The scientific analysis of historical paintings has been traditionally restricted to the analysis of paint cross-section samples. This invasive method provides extensive information but is inherently limited in scope due to the extreme heterogeneity of paintings. In the last decade, non-invasive spot analyses and spectral imaging methods have become increasingly widespread in cultural heritage science. Two of these methods are macroscopic X-ray fluorescence imaging spectroscopy (MA-XRF) and reflectance imaging spectroscopy (RIS). These methods allow for 2D-scanning the entire surface of a painting and provide complementary information on elemental and molecular composition and distribution of the paint. However, these methods are often used only for qualitative analysis of the paint based on relative distribution maps, revealing only limited information about the paint layer stratigraphy. This thesis is an exploration of a combined approach for quantitative analysis of paint composition and layer stratigraphy using MA-XRF and RIS.

The research used a set of specially prepared paint samples of mixtures and multiple layer applications based on historically relevant pigments which were scanned using MA-XRF and RIS in the visible and Near IR range (400-2500 nm). The spectral data acquired were processed and analyzed in a variety of ways, including Non-negative Matrix Factorization, Non-Linear Least Square Fitting, among other methods; in an attempt to gather quantitative compositional and stratigraphic data.

In these trials, using characteristic reflectance features in the visible range together with a comparison of highly and lightly absorbed X-ray fluorescence lines allowed for the identification and quantification of surface specific compounds related to the top paint layer. Further comparison of fluorescence lines and absorption features in the Near IR range provided a potential avenue for quantification of subsurface paint layers. The results confirm that the combination of these methods allows to reveal the paint stratigraphy. The project provides samples and data sets which may serve as the basis for the development of a robust algorithm to address this issue in the future.

Acknowledgements

This work is dedicated to Sander van Asperen and Saskia van der Meer, two people who were instrumental to my success throughout my studies. Ms. van der Meer not only supported and guided me as I dealt with all sorts of issues which popped up during my time in Delft, but always did so in a friendly and positive manner, for which I am extremely grateful. Mr. van Asperen, in his never-ending grace and patience, not only endured sharing his office with me and dealing with all my nonsense for the last two and a half years, but also provided me with sage-like guidance and the means to support myself during my studies, for which I will be forever grateful and deeply indebted.

This work would not have been possible without the guidance and support of my supervisors, Prof. Joris Dik, Dr. Matthias Alfeld, Dr. Annelies van Loon, Dr. Francesca Gabrieli and Dr. Victor Gonzalez. I would particularly like to thank Prof. Dik and Dr. Alfeld for introducing me to this field in the first place and helping me with the application for this project, and Dr. van Loon, Dr. Gabrieli and Dr. Gonzalez for giving me the opportunity to work alongside them in this and other projects, specially for allowing me to assist during Operation Nightwatch.

I would like to thank everyone at the Conservation and Science Department of the Rijksmuseum for their friendliness and eagerness to help during my project, in particular my fellow interns who provided much needed laughter during particularly difficult times. I never had such a lovely group of co-workers and they have set an unreasonably high standard for whoever I work with next.

I would also like to thank my girlfriend Maria and my friends Maurice, Will, Artemis, Tim, Xiao, Katja, Rohan, Ines, Jun and all the Britnis for keeping me sane during what has been a tumultuous time in my life.

Finally, I would like to thank Iantra Solari for his invaluable help during this entire project as well as for his constant companionship. I would not have made it this far without him.

Contents

List of Figures

List of Tables

Chapter 1

Introduction

1.1 What is a painting?

Paintings are complex things. As pictorial recordings they use symbolism, composition, color and other means to represent ideas, places, people, creatures, objects and events, real and imaginary alike. As cultural heritage objects they represent socio-cultural forces which help shape our understanding of history.[1] However, the complexity of paintings is not limited to the aesthetic nor the cultural. As physical objects, paintings tend to be complicated structures comprised of many different paints using many different pigments with different chemical composition and different physical properties combined in different ratios, all distributed heterogeneously throughout the surface and arranged in different layers applied in different orders and of different thicknesses.[2] This latter type of physical complexity is what this thesis is focused on.

To address this complexity, it is important to first define the terminology used to describe the structure of a painting. What follows is a summary of the structure of a painting based on the description of Taft and Mayer.[2] Figure 1.1 shows a cross sectional view of the structure of an average painting. First comes the support, which is the structural component on which the paint is applied. Painters have used a wide variety of supports throughout the ages, ranging from the more conventional wooden panels, canvases, and walls, all the way to turtle shells[3] and ivory panels.[4] The type of support used is one of the main characteristics used to classify paintings.[5] The type of support also greatly affects the structure of a painting and how it can be analyzed. The most common supports are the aforementioned wooden panels and canvases, which are the most common examples of what are known as easel paintings, which are the focus of this research.

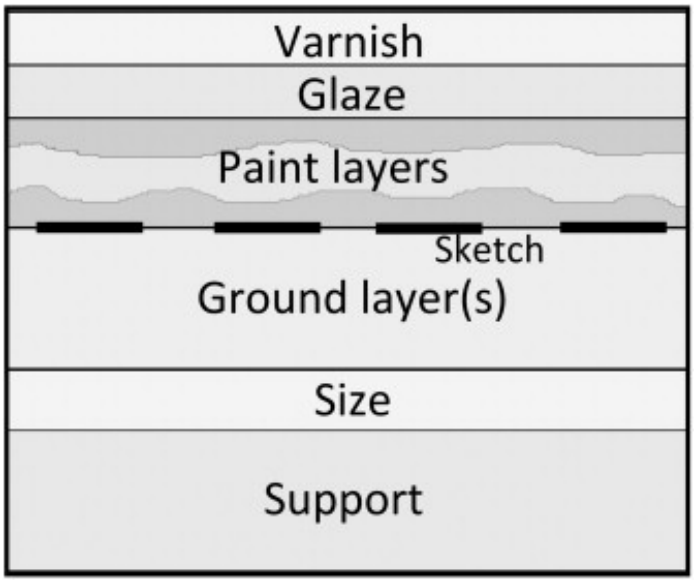

Figure 1.1: Cross-sectional view of the average structure of an easel painting.[6]

A wooden panel or a canvas are usually not very good to paint directly onto, hence a sizing layer is applied. The main purpose of this sizing layer is to prevent the absorption of subsequent ground or paint layers into the support, which would both weaken the painting and possibly have undesirable effects on the support. After the sizing, one or more ground layers are applied, which further protects the support, but most importantly provides a layer even in both color and topography upon which the painting can be made. The kind of ground used varies significantly depending on the artist, the geographical location and the support used.[2]

It is after the ground that the painting really starts to take shape. The artist would often prepare an underdrawing or painted sketch, as an initial description of the composition. What this sketch is made with depends on the kind of ground used. After the sketch was finished, all the different paint layers would be applied. Paint in its most simple form is a mixture of a pigment, which provides the color, and a binder, which joins the pigments together and to the support. At this point there is another major characteristic which is used to differentiate paintings, which is the type of binder used. From the 15th to the early 20th century, linseed oil was the most prominently used binder and is, therefore, the focus of this research.[2]

The way paint layers are distributed is inherently heterogeneous and is, ultimately, what defines the artwork. Paint can be applied in single thin

layers or in stacks of layers of differing thicknesses and opacities, depending on what the artist wishes to show. There can also be overpaint layers applied by later owners or conservators attempting to modify or conserve the painting. On top of the paint layers there can be a thin semi-transparent layer, referred to as a glaze, used to modify the appearance of an underlying paint layer without completely covering it. After all paint and glaze layers are finished, a clear varnish layer is often applied throughout the whole painting. This varnish both protects the paint layers, saturates the colors and gives the painting a uniformly glossy finish.[2]

1.2 Scientific Analysis of Paintings

This very heterogeneous structure makes the analysis of paintings an extremely complicated task. Historically, the study of paint layer stratigraphy would be done by taking small cross-section samples.[7] Figure 1.2 shows such a cross-section sample. Cross-section sampling is useful and can provide unparalleled insight into the stratigraphy and composition of paint layers. However, this method has significant drawbacks. Firstly, the information provided by such a sample is extremely localized at the micro-scale to where the sample was taken from. But most importantly, the method is invasive and thus cannot be done in large quantities without affecting the painting. Generally, this method provides invaluable information for conservators and researchers and leaves only microscopic damage, and thus is still a very commonly used method.

But as non-invasive spot analyses and imaging spectroscopy techniques have advanced and become more versatile, there has been strides at applying these non-invasive methods to the analysis of easel paintings.[8] Although these methods have become more common, they have not replaced cross-section sampling. Instead, they have helped identify areas of interest to take samples from, increasing the usefulness of any sample taken.[9] A description of some of these methods will be covered in chapter 2, but an important thing to point out is that these methods tend to provide different kinds of information and are, therefore, complementary techniques which can and are used in conjunction. However, when these methods are used in conjunction, the level of interaction between them tends to be limited to qualitative analysis based on processed data, as is exemplified by the recent analysis conducted on the pigment distribution of Johannes Vermeer's *Girl with a Pearl Earring*.[10]

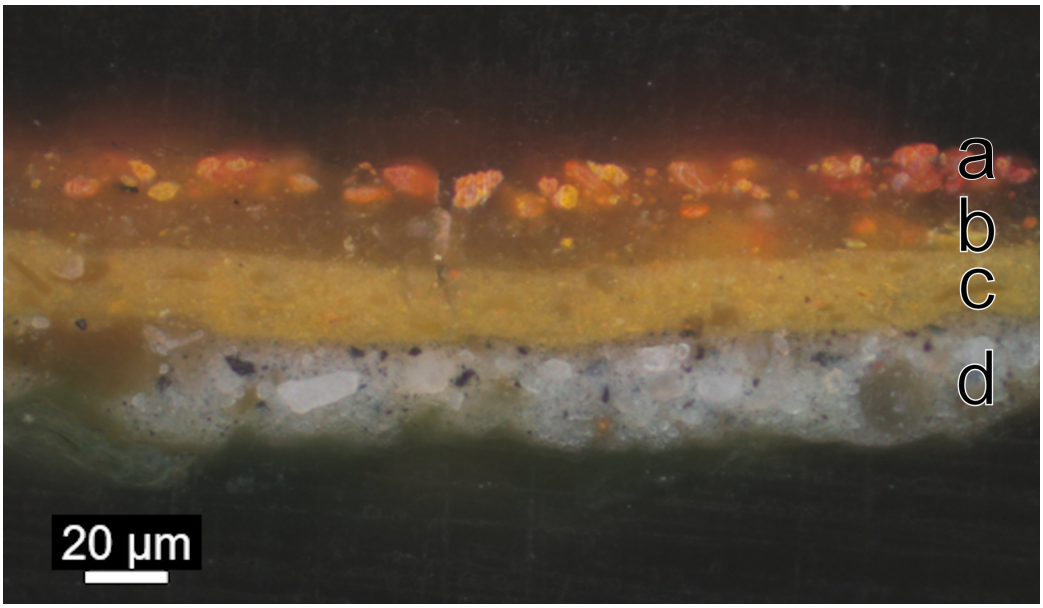

Figure 1.2: Example of a paint cross-section sample. **a-c** are different paint layers and **d** is the ground. Thanks to Dr. Victor Gonzalez from the Rijksmuseum for providing the image.

1.3 Research Goals

The goal of this thesis is to experimentally evaluate the viability of using a combined data analysis approach to gather semi-quantitative information on the stratigraphy and composition of paint layers using two of the most well developed techniques, macroscopic X-Ray fluorescence imaging spectroscopy (MA-XRF) and reflectance imaging spectroscopy (RIS). These methods are described in more detail in chapter 3, but in short, MA-XRF and RIS are surface scanning techniques which provide elemental and molecular information, respectively. The main challenge for quantitative analysis using these techniques is that the resulting data are 2D-projections of a 3D object. For painting analysis, this means that the contribution of each of the different layers cannot be easily distinguished. This research looks for possible methods of quantifying the layer contributions based on two important factors, layer composition and layer stratigraphy. As the contributions of these factors are expected to be rather complex, they were studied seperately using specially prepared layered paint systems and paint mixture samples. These samples were scanned using MA-XRF and RIS, and several quantification approaches were tested using the acquired measurement data.

This research followed roughly 5 stages and this text is therefore divided into that many chapters, plus an introduction and a conclusion. Chapter 2 is an overview of the most prevalent methods for non-destructive analysis of paintings, including their fundamental concepts and how they are useful for analysis. Chapter 3 is an in-depth description of the MA-XRF and RIS methods used in this research, describing the equipment used, the data they output and how it is normally processed. Chapter 4 is a description of the experiments used for this research and the reason these experiments were used. It describes the the preparation and scanning of the test samples. Chapter 5 focuses on the different attempts to produce semi-quantitative results from the acquired data. Chapter 6 provides a review of the acquired results and discusses the practical applicability of the developed data processing methods.

Chapter 2

Methods for Non-invasive Painting Analysis

Throughout the last century, art historians, conservators and scientists have applied many newly developed analytical techniques to the study of paintings. A thorough review of the most significant imaging methods used in the analysis of paintings has been conducted by Alfeld and Broekaert.[6] This chapter provides a summary of a selection of non-invasive methods for paintinig analysis which can provide information on layer stratigraphy and composition. These methods can roughly be divided into three main groups: traditional methods, spot analysis methods and spectral imaging methods. All the methods discussed here use electromagnetic radiation but differ in which part of the spectrum is used and what kind of interaction is recorded. Figure 2.1 provides a summary of the spectral ranges and the methods used in each. These methods also differ in their measurement geometries and their dimensionality, the different kinds of which are detailed in Figure 2.2.

2.1 Traditional Methods

X-ray radiography (XRR) is the oldest and most widely used painting analysis technique.[6] It is a transmission measurement based on the absorption of X-rays by the painting. An X-ray source emits the radiation onto the painting and a sensor or film records how much of the radiation manages to get through. Since the X-ray absorption of a paint layer depends on not only its composition but also its thickness, it is not possible to differentiate between a thin layer of a more absorbing element and a thick layer of a less absorbing element. This means XRR does not give quantitative data on the paint composition or layer thickness, but it can give some qualitative information

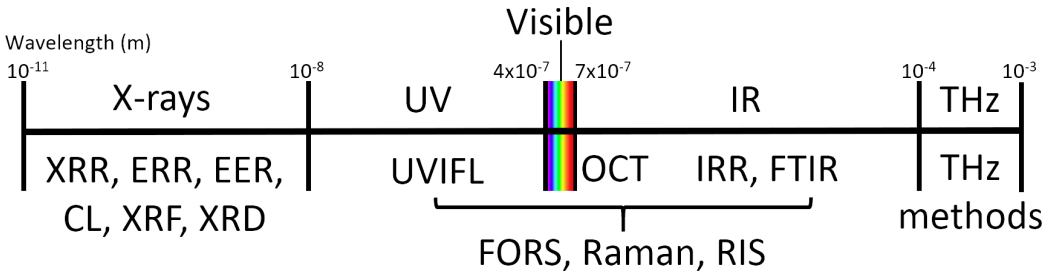

Figure 2.1: The range of the electromagnetic spectrum used for cultural heritage science and where the discussed methods fall within it.

on what pigments may be present and how they are distributed. This can be used to identify hidden paint layers and areas of restoration. Given its transmission geometry, the support of the painting contributes to the measurement and thus the measurement can provide useful information about the support.[11] If this contribution is not desired, there are variations of the method, such as strati-radiography and stereo-radiography, which reduce the influence of the support on the measurement.[6]

Nowadays, advancements in sensors and data processing have provided new applications for XRR which can provide other kind of information. Comparing XRR images acquired at different energies can be used to provide information not only on the number of photons transmitted through the sample, but also their energy. An example of this is a method known as dichromography, where two images acquired at different energies, generally above and below the absorption edge of a certain electron shell of a specific element, are compared to one another to understand the distribution of the element.[12] The resulting measurement is usually an elemental distribution map, useful for identifying pigments and studying their distribution. However, the elements visible with this method depend strongly on the sample. The prevalence of lead white in historical paintings makes the analysis of lighter elements impossible due to the strong X-ray absorption of Pb.[12] This method is only one of a larger group known as energy resolved radiography (ERR).

By capturing a number of XRR images whilst rotating the object, it is possible to create a virtual 3D reconstruction of said object. This method is known as computed tomography (CT). However, CT normally does not work well with planar objects due to the low transmission of X-rays along the object plane. To avoid this issue, a variation of this method called computed laminography (CL), which rotates the sample around an axis which

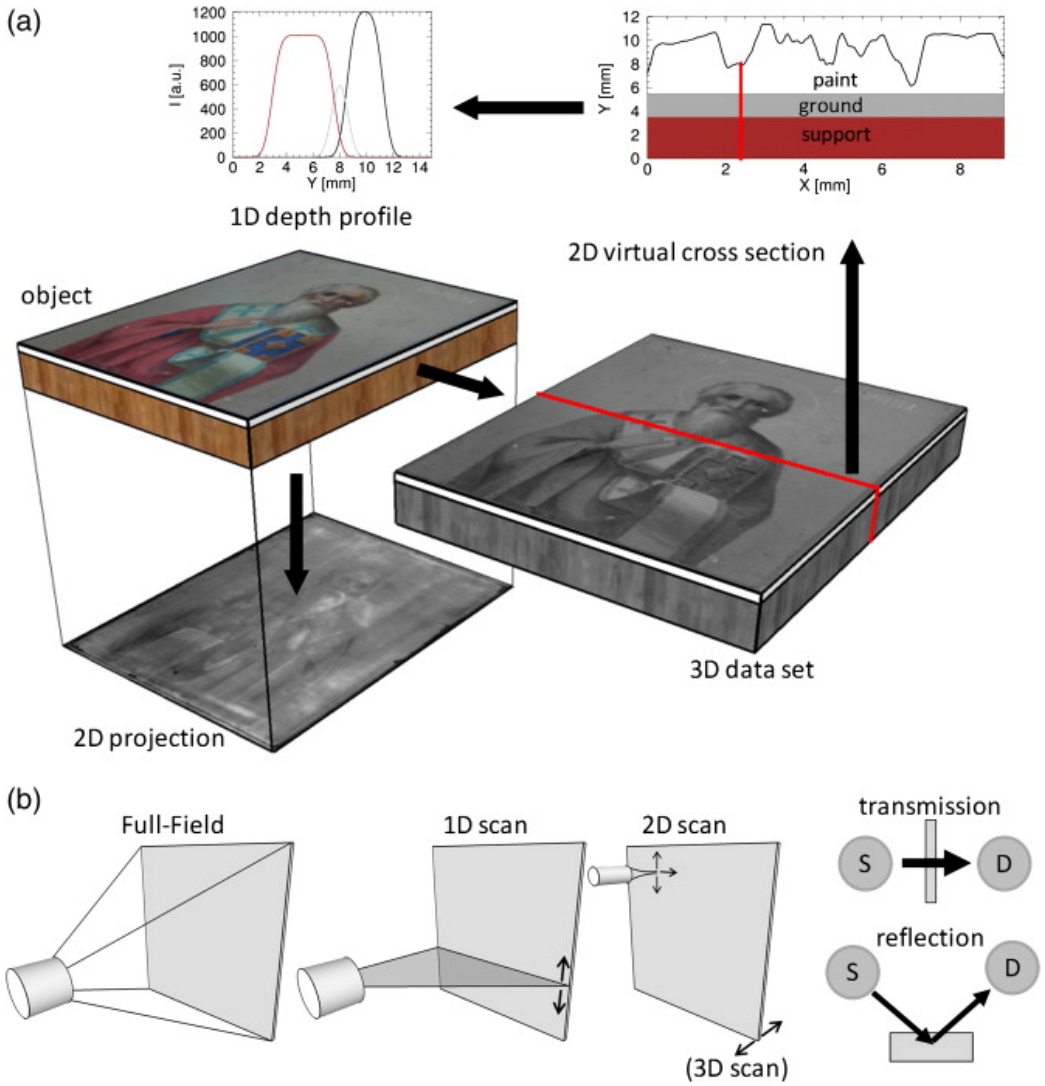

Figure 2.2: **a)**Different measurement dimensionalities, ranging from 1D depth profiles to full 3D data sets. **b)**Different measurement geometries and data acquisition procedures. Some analyitcal methods are restricted to a specific geometry and data acquisition procedure, whilst others can be used in multiple configurations.[6]

is not orthogonal to the beam direction, is used for the study of planar objects.[13] The resulting 3D measurement can provide valuable insight into the paint layer stratigraphy and stability problems.[14] However, the measurement has practical limitations as to the size of the objects studied and was until recently limited to synchrotron sources.[13]

Beyond XRR there are other methods which are used. Electron emission radiography (EER) is a reflective measurement method based on the emission of photoelectrons by surface paint layers when they are energetically excited.[15] The method uses a high energy X-Ray source to excite the surface elements, with a filter to absorb the lower energy part of the spectrum. The recording film is placed directly on the surface of the painting and is of a material that does not react to the high energy X-rays but does darken in reaction to the emitted photoelectrons. Since electrons are readily absorbed by paint layers, most of the electrons that react with the film are emitted from the surface paint layers. This allows the study of surface paint layers without considering the effects of underlying paint layers or the support. This method allows for the analysis paintings done on highly X-ray absorbing supports like copper plates, which is not possible with XRR.[16] The resulting measurements are similar to XRR, in that they provide only qualitative information on possible pigment distribution.

Infrared photography (IR-photography) is a method similar to analogue photography, but which uses a film sensitive to radiation in the infrared region (specifically 700-900 nm) rather than radiation in the visible region. This method can often provide insight into previous restorations, as paint mixtures made to match the colour of the painting often have different reflectance in IR.[6] Nowadays, IR-photography has been mostly replaced by its digital analogue, infrared reflectography (IRR), which expanded its spectral ranges, first further into the near-IR (NIR, 900-1100 nm) and later into the shortwave IR (SWIR, 1000-2400 nm), which offers the best results for analysis of underdrawings, as most paints tend to have high transparency in this range whilst the carbon-based black pigments often used for underdrawings are highly absorbing.[17]

UV-induced fluorescence photography (UVIFL) is another widespread analytical method applied to the study of paintings. It is based on the visible fluorescence emitted by certain materials when exposed to UV light.[18] This method allows for the study of materials which exhibit UV fluorescence, such as varnishes and certain kinds of paints.[19] This method is useful for determining areas of restoration and studying any present varnish layers which are invisible for the other described methods.[20]

2.2 Spot Analysis Methods

The development of non-invasive spot analyses allowed to perform actual chemical analysis on a painting without having to take cross-section samples.

X-ray fluorescence spectroscopy (XRF) is the spot analysis most relevant for this research. It is based on the emission of characteristic X-Rays when the sample is exposed to an X-ray beam. These emissions can be measured and used to identify the elements present.[21] There is a variant of this method, called confocal X-ray fluorescence spectroscopy (CXRF), which allows for depth discrimination during the measurement.[22] The measurement provides insight into paint layer stratigraphy and elemental composition. However, CXRF measurements normally take very long (about 1 hour per point),[23] which restricts its practical applications.

XRF is not the only X-ray based spot analysis method. X-ray diffraction (XRD) is a measurement method based on the diffraction of incoming X-Rays due to the crystal structure of the sample. The resulting diffraction patterns are unique to specific crystals and can be used to identify pigments.[24] Traditionally, XRD was restricted to the analysis of small samples using non-mobile diffractometers, but now portable varaints (p-XRD) are available. The measurement can be done in transmission or reflection geometry, but most portable equipment use a reflection geometry.[25] This method is restricted to the analysis of crystalline materials, and is therefore not suitable for all pigments.

Beyond X-rays, other sections of the electromagnetic spectrum are also used. The Near-UV, visible and Near-IR ranges are used in Raman spectroscopy. This is a method based on the Raman (inelastic) scattering of photons by the sample. The measurement uses a laser with a wavelength which is not absorbed by the sample to study its vibrational modes. These vibrational modes can function as molecular markers for different pigments and binders.[26] The most common issue encountered when using this method is sample fluorescence, which can block any of the actual Raman signal. There are variations such as subtracted shifted Raman spectroscopy (SSRS) and Fourier-transform Raman (FT-Raman) which can account for this.[26]

Fiber Optics Reflectance Spectroscopy (FORS) measures the reflectance spectra of a sample across a specific spectral range, which can go anywhere from Ultraviolet (UV) to Mid Infrared (MIR). The resulting spectra can be used to identify molecules based on characteristic absorption features.[27] Fourier-transform infrared spectroscopy (FTIR) is a similar concept, but uses a different acquisition method for the spectra. It gets it name from the fact that a Fourier-transform is necessary to interpret the acquired data.[28] The most significant challenge for these methods is the presence of both specular and diffuse reflection in the resulting spectra. The features used

for characterisation come from the diffuse reflection, but strong specular reflection can overshadow them.[28]

Terahertz (THz) spectroscopy is an umbrella term used to refer to a few methods based on the THz range of the electromagnetic spectrum (0.03-3 mm).[29] In the context of cultural heritage, the most common of these methods is THz Time Domain Spectroscopy (THz-TDS).[30] THz measurements can be used for pigment identification, study of paint layer stratigraphy and detection of defects.[31]

2.3 Spectral Imaging Methods

Spectral Imaging methods are based on forming an image in which every pixel has a full measurement spectrum. This image provides information not only on what elements and molecules are present, but also their distribution across the scanned surface. This allows for the identification of pigments, changes in composition and areas of restoration.[32,33,34] The nature of this spectrum varies from method to method. Several of these methods are basically just applications of the previously discussed spot analysis methods in scanning geometries. Macroscopic X-ray fluorescence imaging spectroscopy (MAXRF),[35] macroscopic X-ray powder diffraction (MA-XRPD)[36] and THz Imaging[30] are examples of this for XRF, XRD and THz spectroscopy, respectively. Other methods are unique for imaging applications.

Reflectance imaging spectroscopy (RIS)(sometimes referred to as hyperspectral imaging) consists of recording a full reflectance spectrum for every pixel in the acquired image. These spectra are similar to those acquired in FORS and FTIR, and include similar molecular information. However, RIS is a classification based on the resulting data, not a specific acquisition method. The acquisition of the spectra can be done using FTIR and FORS in scanning geometry,[37] but it can also be done using specific spectrometers commonly referd to as hyperspectral cameras.[38] This method is one of the more recent additions to paintings analysis, having been originally developed for remote sensing in geological applications,[39] and has therefore only recently become more widespread. The resulting measurements contain molecular information on the pigments present and their distribution. Depending on the spectral range covered in the measurement, the scans can also be used to identify changes in composition and restorations, as well as to analyze underdrawings.

A uniquely imaging method is optical coherence tomography (OCT),

which is a method based on the interference between electromagnetic waves. The most common configuration for this is based on a Michelson interferometer, where a single incoming beam is separated into a reference beam and a sample beam. The sample beam is reflected off the sample and then recombined with the reference beam, resulting in an interference signal.[40] The measurement results in a digital cross-section, where the interfaces between layers are visible. Several cross sections can then combined to form a 3D tomogram,[41] which includes information into the thickness and opacity of layers throughout the scanned surface. Given the low transparency of paint layers, this method is most often used to analyze superficial secondary layers (like varnish).[41] However, there are ongoing attempts to use different light wavelengths to make the method useful for studying paint layer stratigraphy.[42]

Chapter 3

MA-XRF and RIS

3.1 MA-XRF

As mentioned in section 2.2, XRF is based on the fact that when a sample is exposed to an X-ray beam, the atoms of the sample become excited and emit characteristic fluorescence radiation that provides quantitative and qualitative information on the elements present.[21] Therefore, an XRF device consists of three main parts: The X-ray source, which creates the X-ray beam used to excite the atoms of the sample; the beam defining optic, which guides the X-ray beam onto the sample; and the detector, which measures the fluorescence radiation emitted from the sample.[43]

MA-XRF consists of making many equidistant XRF measurements across the surface of an object to make elemental distribution maps. A MA-XRF device consists of the same three main parts as a normal XRF device, all integrated into a measurement head, but with the addition of a positioning system, which moves the sample relative to the measurement head.[35] Figure 3.1 shows a simplified diagram of the MA-XRF scanner used in this research.

In the context of this research, the scanning is performed using a custom Bruker M6 JETSTREAM MA-XRF scanner owned by the Rijksmuseum, pictured in figure 3.2. The scanner consists of a MCBM 50-0,6B metal ceramic X-ray tube with a Rhodium target and a 0.1 mm Be window as an X-ray source; a polycapillary lens with a minimum spot size of 100 µm as a beam defining optic; and two VH-Par-SDD as detectors positioned at 60° on either side of the X-ray beam.[44] The device uses a cartesian coordinate robot as a positioning system which moves the measurement head whilst the sample remains static. During scanning, the measurement head is moved along the x and y axes, whilst the z-axis remains static. The maximum scan dimensions

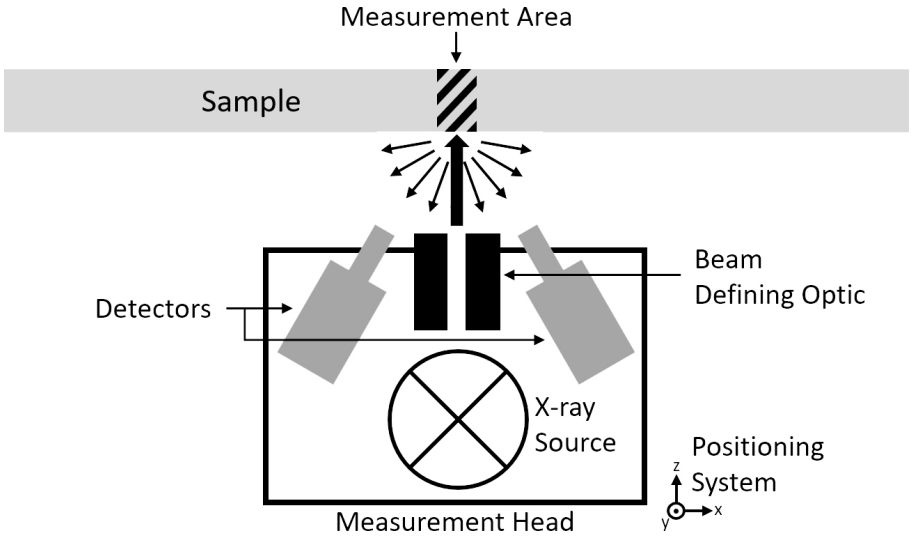

Figure 3.1: Simplified diagram of the MA-XRF measurement setup used in this research.

are 780x580 mm. For samples larger than these dimensions, it is possible to take multiple scans and stitch them together. The z-axis is only used to set the distance between the measurement head and the sample, which describes the actual X-ray beam spot size. In the instruction manual, the optimal distance between the measurement head and the sample is said to be of 9 mm , at which the beam spot size is of 100 µm.[44] Existing research using the device has found the minimum spot size to be around 40 µm, at a sample distance of 6 mm.[35] Whilst scanning objects at the museum, the sample distance is 10 mm to avoid possible damage to the sample. At this distance, the beam spot size is around 300 µm.[35]

The scanning is conducted as a raster, and there is an individual XRF measurement per pixel. However, the measurement head does not stop on each pixel, but is instead moved along the x-axis at a fixed speed, and a timer determines when the measurement for a certain pixel begins and ends. The speed at which the devices moves is a function of the scan step size (size of an individual pixel) and measurement dwell time. Once the scanning of a line is finished, the measurement head is moved back to the start of the line, moved one step along the y-axis and a new scan line is started. The y-distance between two scan lines is equal to the desired step size. This process is repeated until the defined surface is scanned in its entirety.

The resulting measurement data is a 2D projection of the scanned surface where each pixel has a full XRF spectrum. In the context of this research,

Figure 3.2: Bruker M6 JETSTREAM MA-XRF scanner with main components marked (A)Measurement Head (B)Positioning System (C)Sample.[45]

each XRF spectrum consists of 4096 channels. Figure 3.3 shows a comparison of different measurement spectra of the same sample pixel using different measurement dwell times. The longer the pixel dwell time, the better the quality of the resulting measurement, but the longer the scan takes.

3.1.1 MA-XRF Data Processing

To extract elemental distribution maps from these spectra it is necessary to separate the contribution of the characteristic fluorescence lines of each element from each other and from the background radiation, which is normally done via spectral deconvolution. However, given that a MA-XRF dataset can consist of upwards of a million spectra, analysis via standard spectral deconvolution strategies is often considered prohibitively long. To account for this, alternate strategies, as the one described by Alfeld and Janssens,[46] have been developed. However, for particularly complex spectra, analysis via standard spectral deconvolution strategies can still be done. In the context

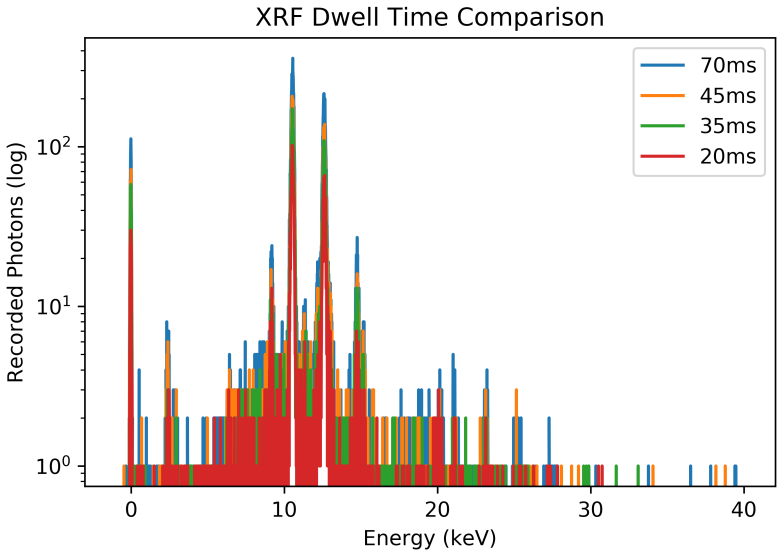

Figure 3.3: Comparison of XRF spectra acquired at different dwell times. These are single pixel measurements of the same point on a 17th Century painting. All spectra were acquired using the same settings (200 µm Tube Current, 50 kV Tube Voltage). Longer dwell times result in more accurate spectra with more pronounced elemental fluorescence peaks.

of this research, analysis of the data set is done using the software package Datamuncher[47] for the bulk of the analysis and PyMCA[48] to create the initial fit files.

This analysis outputs the signal intensity of each considered fluorescence line for each pixel. From these signal intensities, relative elemental distribution maps can be produced. Figure 3.4 shows some examples of these elemental distribution maps. The resulting maps are monochromatic representations of the elemental concentration per pixel. The brighter a pixel, the more intense the signal of the measured fluorescence line, and therefore the higher the concentration of the element in question.

3.1.2 Applications and Limitations of MA-XRF

MA-XRF has become fairly widespread since its introduction in 2008,[49] with many museums and research institutions using self-constructed scanners[37] or commercially available scanners.[35,49] For paintings analysis, this method can provide qualitative information regarding the pigments present in the painting and their distribution, which can provide insight into the painting's

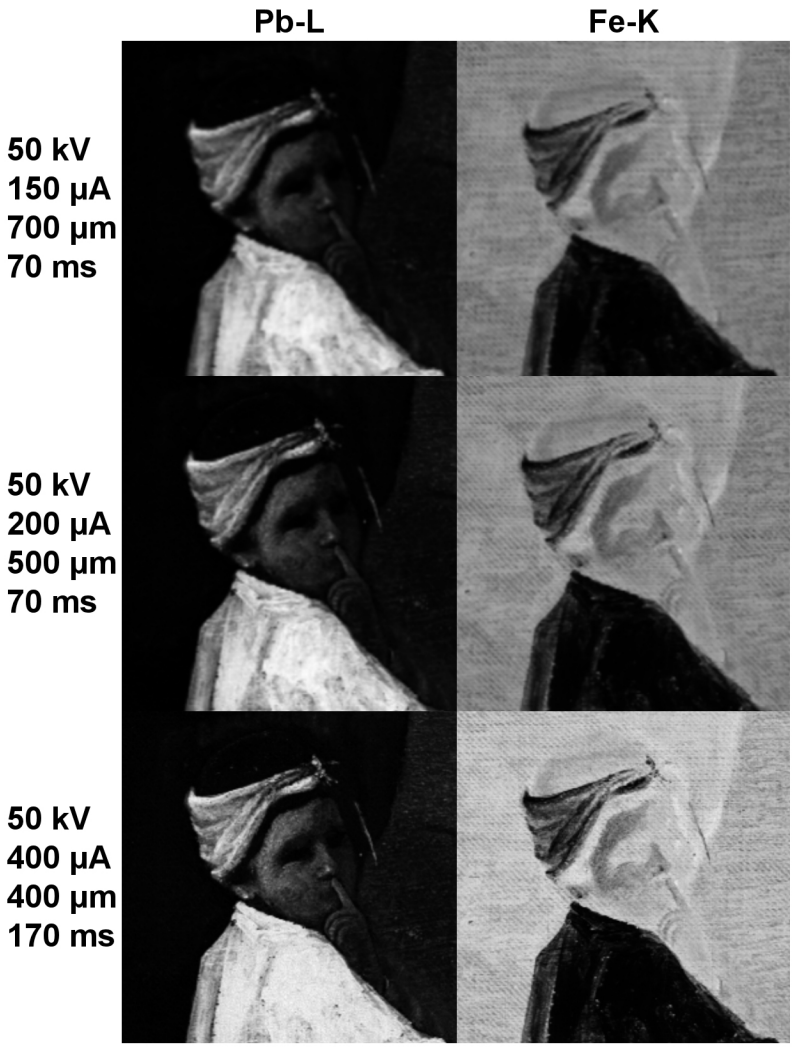

Figure 3.4: Examples of MA-XRF maps acquired at different step sizes, dwell times and tube currents. The maps show a figure of a boy painted using lead white on an Fe-including ground. Brighter areas denote a stronger elemental fluorescence signal. Increasing the dwell time or the tube current reduces the LODs, improving the maps in areas with low elemental concentration, as can be seen in the hand of the boy in the Pb-L maps, but it can also lead to sensor saturation, as can be seen in the boys shirt in the Pb-L maps. The lead white used to paint the boy blocks the signal of the Fe-including ground.

provenance, the artist's process, changes in composition, previous restoration campaigns, amongst others.[33] The method's great penetration depth makes it optimal for identification of hidden paint layers. However, the method has

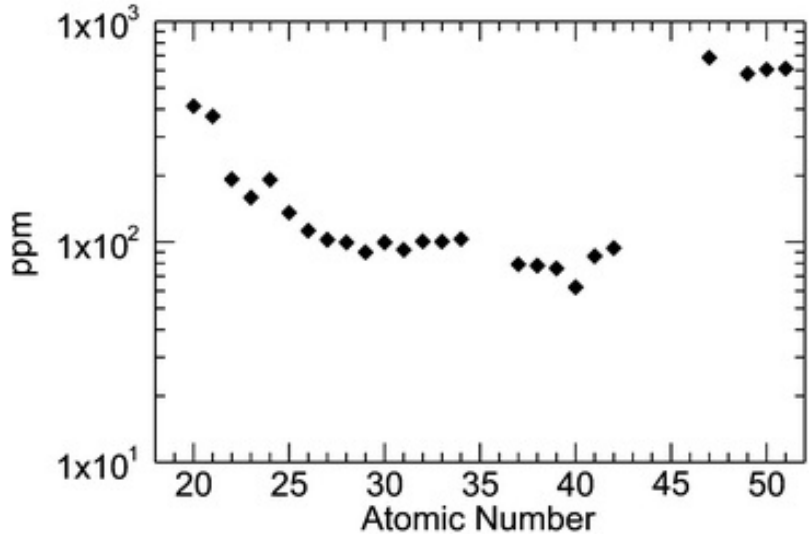

Figure 3.5: LOD of the M6 Jetstream based on K fluorescence lines at 50 kV and 600 µA. This denotes the minimum required mass concentration of the element for the system to reliably identify it in an XRF spectra. Lower LODs mean improved spectral accuracy of the measurement.[35]

some important limitations. Depending on the device used, the method can only accurately measure certain elements. The application of XRF to cultural heritage objects is considered to be practically limited to elements with atomic numbers above 11 (Na).[50] Given the low acquisition times, MA-XRF is often considered to be limited to elements with atomic numbers between 20 and 82 (Ca-Pb), although the limits of detection of all the elements are not equal.[43] The limits of detection (LOD) of the M6 Jetstream were researched by Alfeld et al.,[35] and are summarized in figure 3.5.

The method's high penetration depth also presents an issue for data processing and result interpretation. The resulting measurement data has contributions of many different layers, and since the method does not have depth discrimination, distinguishing each of these contributions is very difficult. Strategies for correcting for uneven background contributions, like that caused by the presence of stretchers in canvas paintings, have been developed.[46] However, algorithms for distinguishing the contributions of different paint layers have not been published so far. A significant challenge for the development of such algorithms are the complex matrix effects resulting from the very in-homogeneous paint composition and layering, which have a significant effect on the XRF signal. These effects and their implications are discussed in further detail in section 5.1.

However, the main practical limitation of this method is the slow data acquisition time. Single MA-XRF scans are most often several-hour-long endeavors, with the precise duration depending on the size of the scanned surface, the desired step size, and the pixel dwell time. Scans of larger objects, which require multiple smaller scans, can take several days or weeks.[51] Most often, the step size and pixel dwell time are determined on a case-by-case basis depending on what is the goal of the analysis and how much time there is available for a specific scan, as there is no widespread standard.

Ultimately, these scan settings determine the quality of a MA-XRF measurement, both with regards to the level of spatial detail present in the resulting maps and their spectral accuracy. Step size determines the level of detail of the acquired images and therefore the minimum size of features which can be visibly resolved. The smaller the step size, the smaller a feature can be whilst still being visibly resolved. Pixel dwell time, on the other hand, determines the spectral accuracy of the measurements. The longer the pixel dwell time, the lower the LODs of each element and therefore the higher the accuracy of the resulting measurement, specially for low intensity signals like those from Pb-M or K-K. In most practical cases, time constraints mean there is a trade-off between step size and dwell time. The X-ray tube current and voltage also play an important role in the spectral accuracy, as increasing either will increase the intensity of the X-ray beam and therefore increase the fluorescence of the sample. This will generally lower the LODs, but limitations of the detector mean that that is not always the case. Increasing the tube current and voltage also means the sample is exposed to a higher amount of radiation, which is generally not desired as it can induce changes in the sample.

3.2 RIS

As mentioned in section 2.3, this method is based on scanning a sample to acquire a reflectance spectrum for every pixel in the image, which can be used to identify present pigments and map their distribution. Figure 3.6 shows a simplified diagram of the RIS setup used in this research.

RIS can be conducted in different spectral ranges depending on the device used. In this research, two hyperspectral cameras were used, one over the visible and near infrared range (VNIR, 400-1000 nm) and another over the shortwave infrared range (SWIR, 900-2500 nm). The scanning process also differs depending on the exact device used. Some devices allow for full-field acquisition (also known as snapshot), in which the whole spectral data

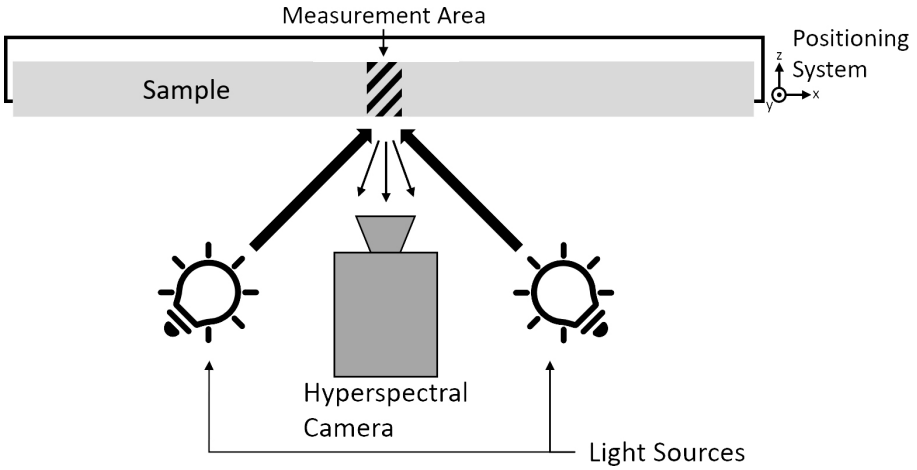

Figure 3.6: Simplified diagram of the RIS measurement setup used in this research.

cube is acquired instantaneously, whilst others incorporate different types of scanning procedures, like push-broom or whisk-broom.[8] In the context of this research, the used hyperspectral cameras are both operated in push-broom scanning, where the camera continuously outputs a full slit spectrum whilst the sample is moved at a set speed in front of the camera. The combination of push-broom scanning and low acquisition time makes RIS a relatively quick process when compared to MA-XRF.

The two hyperspectral cameras used for this research are the Surface Optics SOC710-E for the VNIR range (260 channels)[52] and the Headwall Micro-Hyperspec SWIR 640 for the SWIR range (267 channels).[53] The positioning system is a motorized easel custom-built by LG Motion UK. Figure 3.7 shows the scanning setup as used for this research.

3.2.1 RIS Data Processing

The resulting measurement data is a stack of images, one per spectral channel, referred to as a "datacube". The first thing to be done is to flat-field correct the datacubes, which is done using two calibration datacubes, one of a highly reflective white PTFE panel taken under the exact same lighting condition to correct for uneven illumination and camera response, and one of a dark frame to correct for detector dark current.[39,54] Each pixel then has a fully corrected apparent reflectance spectra, samples of which can be seen in figure 3.8. Given the limited vertical field of view of the cameras, it is often necessary to do several scans which are then stitched together to form

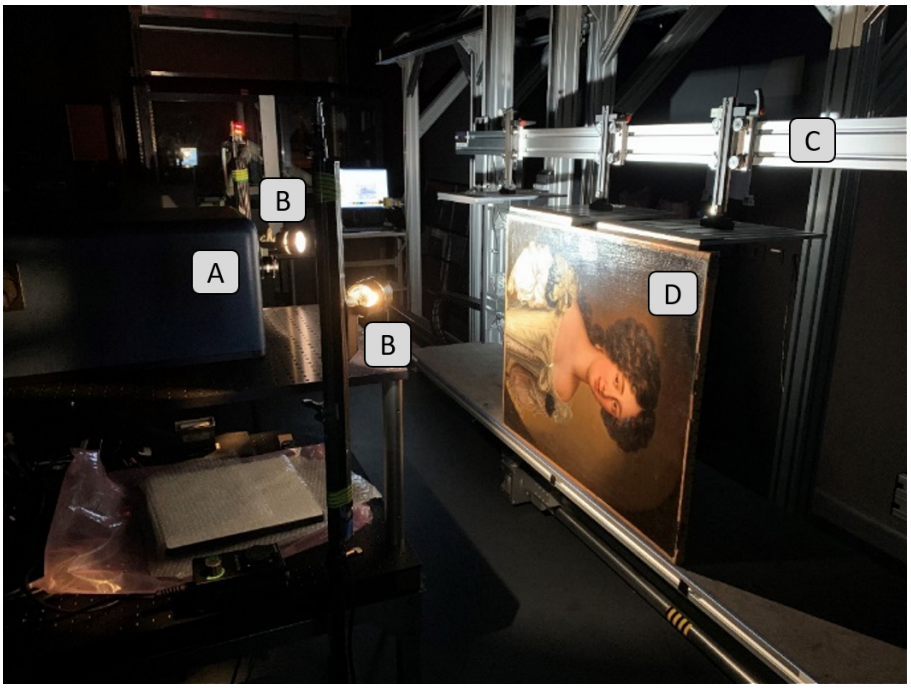

Figure 3.7: The VNIR-RIS scanning setup used in this research with main components marked (A)Hyperspectral Camera (B)Light Sources (C)Positioning System (D)Sample. The SWIR-RIS scanning setup is extremely similar, but uses a different camera and light sources. Thanks to Dr. Francesca Gabrieli from the Rijksmuseum for providing the image.

a datacube of the entire surface of the painting.

The analysis of the spectra is somewhat more complicated than for XRF. The spectra are a combination of the spectra of the present species but, unlike XRF, where the contribution of each fluorescence line is assumed to be a nearly-gaussian shaped peak,[55] the contribution of each species depends not only on the chemical composition of the pigment, but also the particle size, concentration and type of binding medium.[56] In the VNIR range, Kubelka-Munk theory[57] is often used to spectrally deconvolute the measurement spectra. In the SWIR range, Kubelka-Munk still can be used, but the assumption that the scattering coefficient is constant is not as applicable as it does vary slowly with wavelength.[58] Because of these complications, analysis of RIS measurements is often done in a more qualitative manner, based on extraction of endmembers from the dataset via either an automated process, like principal component analysis (PCA), or manually selecting specific pixel spectra. The endmembers can then be used to produce distribution maps

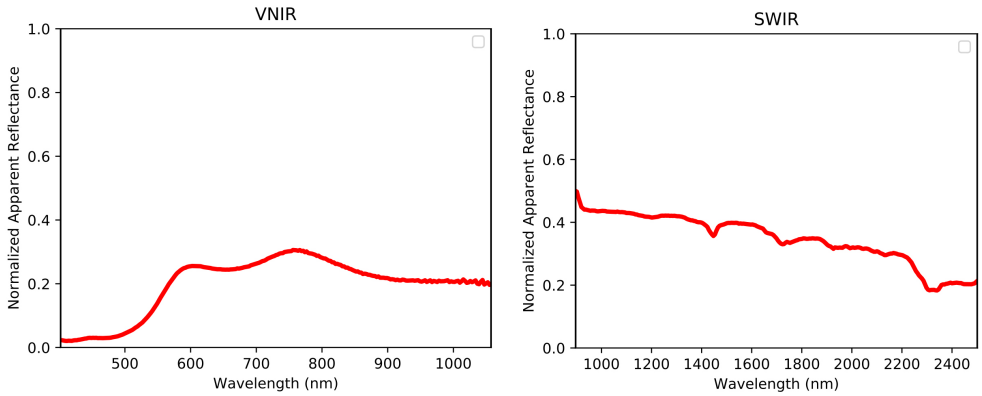

Figure 3.8: Example of RIS Spectra, as acquired by the VNIR and SWIR hyperspectral cameras used in this research.

using spectral angle mapping (SAM) and be compared to spectral databases for pigment identification.[54]

3.2.2 Applications and Limitations of RIS

RIS for paintings analysis has many applications including pigment identification and mapping,[38,59] binder identification and mapping,[37,60,61] colour rendering and condition monitoring.[56] The method is often used alongside MA-XRF, as they complement each other and result in a more reliable pigment identification.[9,10] The main limitations of the method mainly come down to the very labour-intensive data processing procedures. Scans must be flat-field corrected, stitched and then analyzed, and all these steps currently require significant user input. Another limitation in the analysis of reflectance spectra is the lack of a comprehensive, publicly-available database of reflectance spectra for pigments and dyes for spectral unmixing.[62]

Specific spectral ranges can also present specific challenges. For VNIR-RIS, the scanning of dark areas is difficult, as the signal-to-noise ratio becomes poor. This can be accounted for using different data processing measures, but this can be very labour-intensive.[10] For SWIR-RIS, the greater penetration depth creates a similar issue to that described previously for XRF, in that the contributions of individual layers are difficult to distinguish. The penetration depth is not as high as that of XRF, for which the contribution of an uneven background, like a stretcher for a canvas painting, is not as significant and easily identifiable.

Chapter 4

Experimental Methods

To better understand and differentiate the effects of paint mixing and paint layering on the MA-XRF and RIS measurements, a series of experiments were conducted. These formed the main body of this project. The experiments consisted of scanning well-defined painted objects using the museum's MA-XRF scanner and two hyperspectral cameras (SWIR and VNIR). Given that the ultimate objective of this research was to achieve semi-quantitative results on paint layer composition and stratigraphy, the objects scanned would have to be objects where this information is already available. Given that there is no painting in the Rijksmuseum collection which is fully defined in this way and can thus serve as a ground truth, it was decided that samples would be created specifically for this purpose. The preparation and scanning of the samples are discussed in this chapter.

4.1 Sample Preparation

The preparation of the experimental samples involved a lot of decision-making that would ultimately decide the applicability of the results. For simplicity, these decisions are divided into two main categories: what paint is used and how the paint is used. What follows is a description of the decision-making process of each category.

4.1.1 Paint Selection

As explained in section 1.1, a paint is a combination of a pigment and a binder. As previously stated, from the 15th to the early 20th century, linseed oil was the most common binder used in paintings and is therefore the binder chosen for the paint samples. The choice of binder is not expected to have a

significant effect on the MA-XRF and VNIR-RIS measurements, but it will have an effect on the SWIR-RIS measurement.[37] This effect must be kept in consideration during the analysis of the samples.

The selection of the pigments is a bit more complicated. There are hundreds of different pigments, each with their unique chemical footprints and usage history. The first choice was to limit the number of pigments used to three. It is believed that three pigments would provide a large enough selection to create a large number of unique samples without becoming overly complex. To aid in the selection, a few criteria were set out:

1. The pigments must be historically relevant. This is to ensure that the results acquired are applicable to as many paintings in the museum's collection as possible and still leaves a very wide range of pigments. Special consideration is given to pigments used in 17th century Dutch painting, as this time-period is one of the specialties of the Rijksmuseum.

2. The pigments must each have unique elemental footprints when compared to one another and their fluorescence lines should cover as broad an energy range as possible. This is not to mean that there cannot be any elemental overlap, but that there must be at least one measurable principal element which is unique to that pigment. This element would function as a marker for this pigment in the MA-XRF results.

3. The pigments must each have unique reflectance features in the visible and NIR spectrum when compared to one another. In contrast to the previous criterion, overlap in these reflectance features should be avoided if possible, as it significantly complicates the analysis of the data. These features would serve as markers for the related pigment in the RIS results.

Criterion 1 is the most limiting, as it removes the vast number of pigments created since the 18th century. Criterion 2 eliminates the possibility of using many organic pigments that do not have any elements that are measurable with MA-XRF. Besides that, criteria 2 and 3 do not really remove any pigments from the selection pool but they significantly limit the possible combinations to be considered. However, that still leaves too many combinations to consider, so it was decided to choose the pigments sequentially.

The first pigment selected was lead white, due to it being the ubiquitous white pigment in European art from roman times up until the 19th

century.[63] Pb also has both low energy fluorescence lines (Pb-M) and high energy fluorescence lines (Pb-L), which makes it particularly useful for the study of layering and matrix effects on MA-XRF signals, as the two lines would be affected to differing degrees. The primary components of lead white are lead carbonate hydroxide ($2PbCO_3 \cdot Pb(OH)_2$) (hereafter referred to as hydrocerussite, the name of its natural mineral form) and lead carbonate ($PbCO_3$) (hereafter referred to as cerussite, the name of its natural mineral form). Hydrocerussite has a hydroxyl stretching overtone feature at 1447 nm and a weak band in the region of the carbonate overtone ($3v_3$) and hydroxyl combination bands at ~2300 nm, which are used as identifiers for the pigment in NIR RIS.[64,65]

The visible spectrum part of criterion 3 requires all the pigments to have very distinguishable colors. Black pigments do not have any significant features in the visible spectrum which would aid in their identification and therefore it was decided to take two non-black pigments. To further aid in their differentiation, it was decided to take one pigment in the lower part of the visible spectrum (Red-Orange-Yellow) and one in the higher part (Green-Blue-Violet).

Based on criteria 1 and 2, it was decided that the second pigment would be an ochre pigment due to their near universal use throughout history and the presence of Fe as an elemental marker.[66] There are a wide variety of ochre pigments based on different iron oxides and hydroxides. An ochre based on goethite (α-FeO(OH)) was selected due to its features in the visible spectrum, namely reflectance peaks at ~600 and ~750 nm and a transition edge at 555 nm,[54] which give it an orange color. Goethite lacks any significant reflectance features in the NIR, but as a mineral pigment from a natural source, it tends to be mixed with other minerals that may have identifiable features.

For the third pigment, it was decided to use azurite, a blue Cu-based pigment. The main compound of the pigment is a form of basic copper carbonate ($Cu_3(CO_3)_2(OH)_2$). It is easily identifiable in RIS since it has a reflectance peak at 467 nm followed by a broad absorbance feature centered around 700 nm. It also has a hydroxyl stretching overtone feture at 1498 nm, and a strong doublet at 2245 and 2351 nm corresponding to the carbonate overtone ($3v_3$) and carbonate and hydroxyl combination features.[64] For clarity, azurite is the name given to both the base mineral and the pigment derived from it, and for simplicity, this paper will also refer to the main compound basic copper carbonate as azurite.

Having chosen what type of pigments would be used, it was still neces-

sary to decide from where to source the pigments. Different suppliers can have different manufacturing processes for synthetic pigments and different sources for natural pigments, which can affect the chemical composition of the pigment. To find the correct source, one candidate for each pigment type was acquired and analyzed to determine if it would work for this project. If a candidate were found to not be suitable, an alternative would be acquired and tested, repeating the process until a suitable candidate was found for each type of pigment. The tests used to analyze the products were XRF, XRD and FORS. The author would like to thank Dr. Richard Huizenga and Mr. Ruud Hendrikx from the Department of Materials Science and Engineering of Delft University of Technology for conducting the XRF and XRD analysis. For the XRF analysis, the measurements were performed using a Panalytical Axios Max WD-XRF spectrometer and the data evaluation was done using the SuperQ5.0i/Omnian software. For the XRD analysis, the measurements were performed using a Bruker D8 Advance diffractometer and the data evaluation was done using the Bruker DiffracSuite.EVA vs 5.1, Profex-BGMN software. For the FORS analysis, the measurements were performed using a Malvern Panalytical ASD FieldSpec 3 and the data was processed using its included data acquisition and visualization software. Following are the results of the pigment selection analysis, separated by type of pigment.

Lead White

The first lead white candidate to be tested was from an unknown manufacturer and available in the Rijksmuseum labs. The results of the XRD and FORS analysis can be seen in figure 4.1. The XRF analysis showed the sample was mostly Pb but also included a significant amount of Ca. The presence of Ca was concerning but not terribly unexpected as lead white is often adulterated with chalk, a Ca-based white pigment.[66] However, the presence of chalk could not be verified by either FORS or XRD. Instead, the XRD spectra verified the presence of hydrocerussite and cerussite, which are expected in traditionally produced lead white, as well as plumbonacrite ($Pb_5O(OH)_2(CO_3)_3$), which can be used as a marker for modern lead white production methods,[67] but which can appear in traditional lead white samples as well.[68] However, the spectra also matched the theoretical diffraction spectra of calcium lead (CaPb), which would account for the presence of Ca, but which to the authors best knowledge has not been found in lead white samples before. The FORS spectra presented a large reflectance peak at ~2150 nm which does not match any expected peak. From these unexpected results it was decided that this pigment was unsuitable for this project.

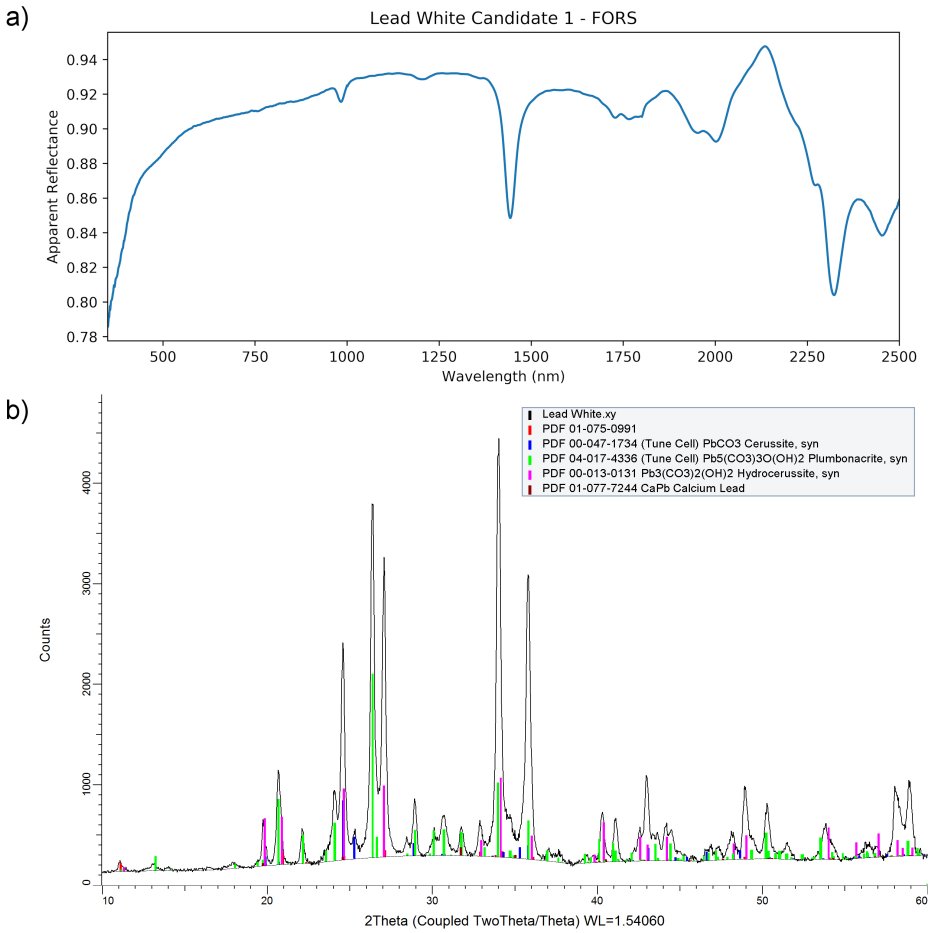

Figure 4.1: **a)**Results of the FORS analysis of the first lead white candidate (unknown source) **b)**Results of the XRD analysis of the first lead white candidate.

The second lead white candidate to be tested was Rublev Colours Stack Flake White. This product is advertised as being produced using the traditional Dutch method,[69] which would make it particularly useful for this project. The results of the analysis can be seen in figure 4.2 and table 4.1.

Table 4.1: Quantitative XRD results for the second lead white candidate (Rublev Colours Stack Flake White).

Compound	Formula	Weight Percentage (%)
Hydrocerussite	$2PbCO_3{\cdot}Pb(OH)_2$	98 ± 1
Cerussite	$PbCO_3$	2 ± 1

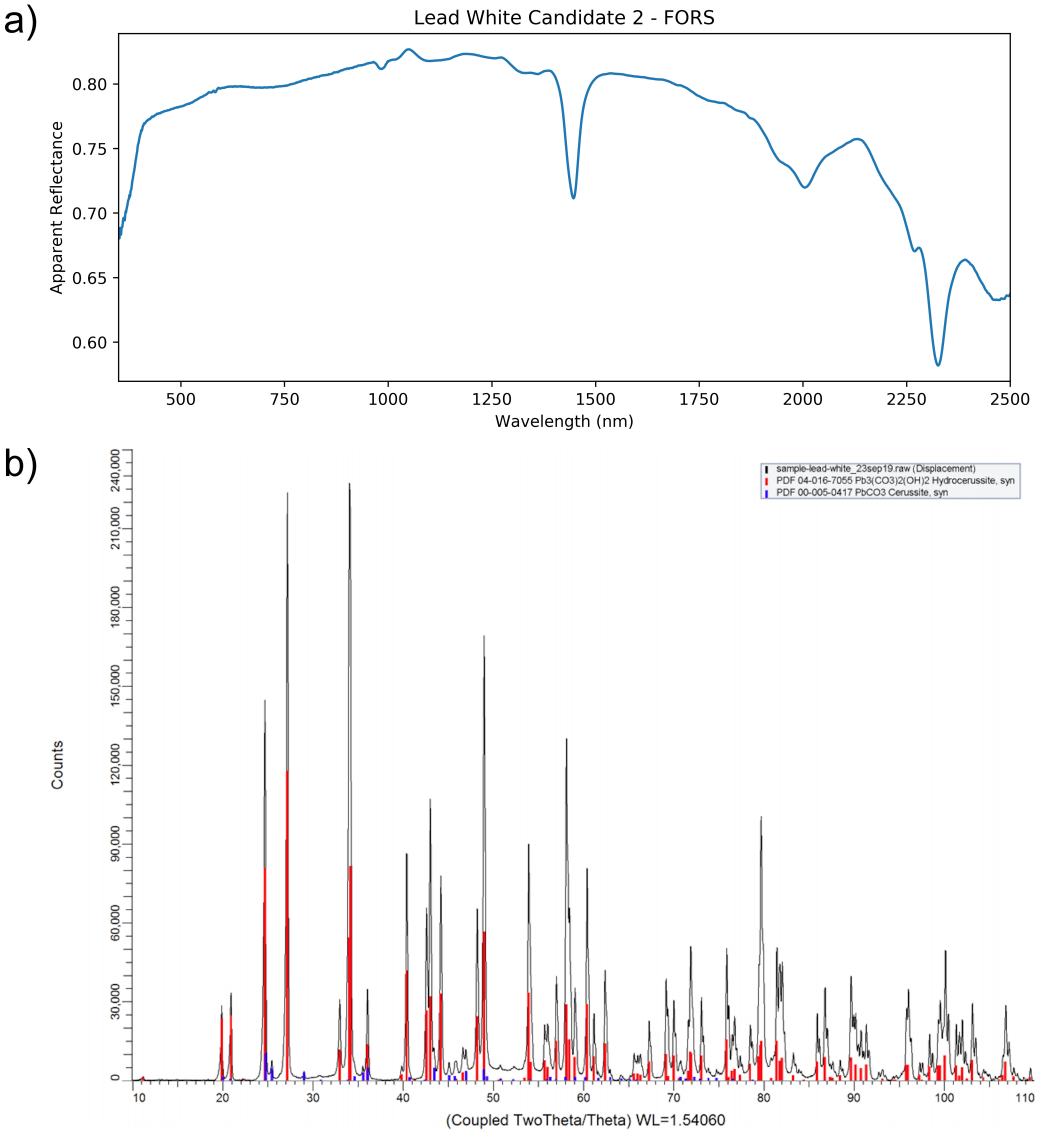

Figure 4.2: **a)**Results of the FORS analysis of the second lead white candidate (Rublev Colours Stack Flake White) **b)**Results of the XRD analysis of the second lead candidate.

The XRF found almost entirely Pb along some trace elements (Si, Mg, Cu and Al) and the XRD confirmed that the pigment was exclusively hydrocerussite and cerussite, as expected from a traditionally produced lead white.[67] The FORS spectra featured the two previously mentioned features at ~1450 and ~2300 nm. All this led to the decision that this would be the lead white pigment used for the samples.

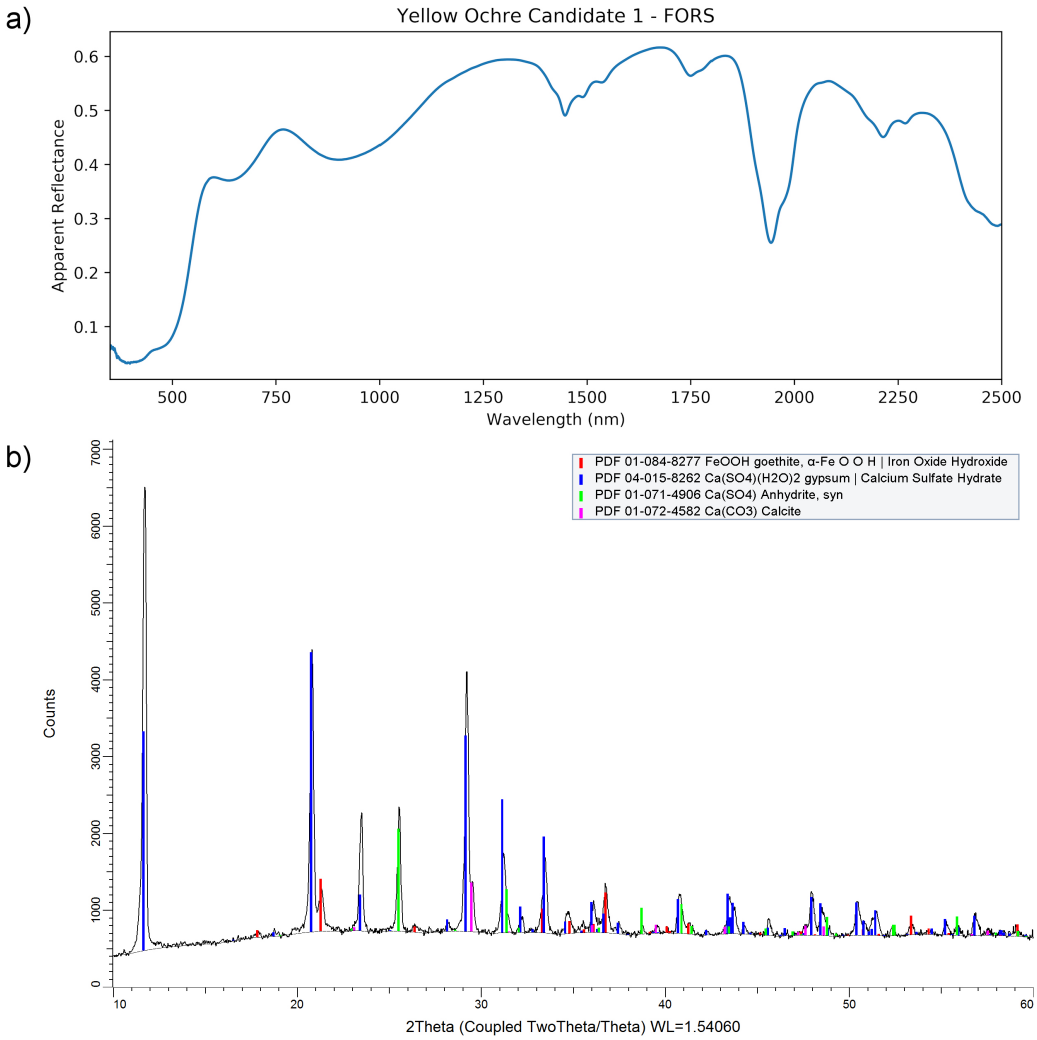

Figure 4.3: **a)**Results of the FORS analysis of the first yellow ochre candidate (Verfmolen "De Kat" Ochre Orange) **b)**Results of the XRD analysis of the first yellow ochre candidate.

Yellow Ochre

The first yellow ochre candidate tested was Ochre Orange from Verfmolen “De Kat”. The XRD and FORS results can be seen in figure 4.3. The XRF matched what would be expected from a natural ochre, with Fe alongside smaller amounts of a variety of other elements, like Ca, Ti and Mn. The XRD found that the pigment was a combination of goethite, chalk (calcite, $CaCO_3$) and gypsum ($CaSO_4{\cdot}2H_2O$). The FORS results confirmed the presence of gypsum through the presence of its characteristic three hydroxyl features

between 1445 and 1535 nm. The presence of gypsum is problematic because of the overlap between the first hydroxyl feature of gypsum with the hydroxyl feature of hydrocerussite, which, although a common scenario in the RIS analysis of paintings,[65] could complicate the quantitative RIS analysis. As this is only exploratory research into the possibility of quantitative analysis it was decided to avoid such complicated scenarios and therefore the candidate was found to not be suitable.

The second yellow ochre candidate to be tested was Yellow Ochre Dark from Rublev Colours. The results of the FORS analysis are presented in figure 4.4. The results of the XRD analysis are presented in table 4.2. The XRF results show significant differences to those of the previous candidate. Si and Al are present in considerable amounts whilst Ca is relegated to a minor element. The XRD identifies that quartz (SiO_2) and kaolinite-1A ($Al_2(OH)_4Si_2O_5$) are major components alongside goethite. However, it is also seen that the goethite present is not pure goethite, but instead an Al-substituted form of goethite, refered to as goethite aluminian. This form of goethite is very common in red soils,[70] specially when found with other Al-containing minerals, like kaolinite. This particular goethite aluminian seems to be 10 mol% Al ($Fe_{0.9}Al_{0.1}O(OH)$). The FORS results show that having this form of goethite does not significantly affect its reflectance spectra and also confirms the presence of kaolinite with its double hydroxyl overtone feature at ~1400nm.[71] The combination of goethite and kaolinite is particularly useful as it provides markers in both the VNIR and SWIR ranges. Thus, it was decided this was to be the yellow ochre pigment used for the samples.

Blue Verditer

The first blue verditer candidate to be tested was Rublev Colours Blue Verditer. Blue verditer is the name given to the synthetic alternative to azurite. Blue verditer is considered to have a paler color than azurite, but it is chemically identical,[66] which could make it a cheaper and more chemically uniform alternative. The results of the FORS and XRD analysis can

Table 4.2: Quantitative XRD results for the second yellow ochre candidate (Rublev Colours Yellow Ochre Dark).

Compound	Formula	Weight Percentage (%)
Quartz	SiO_2	37 ± 2
Goethite Aluminian	$Fe_{0.9}Al_{0.1}O(OH)$	33 ± 2
Kaolinite-1A	$Al_2(OH)_4Si_2O_5$	30 ± 2

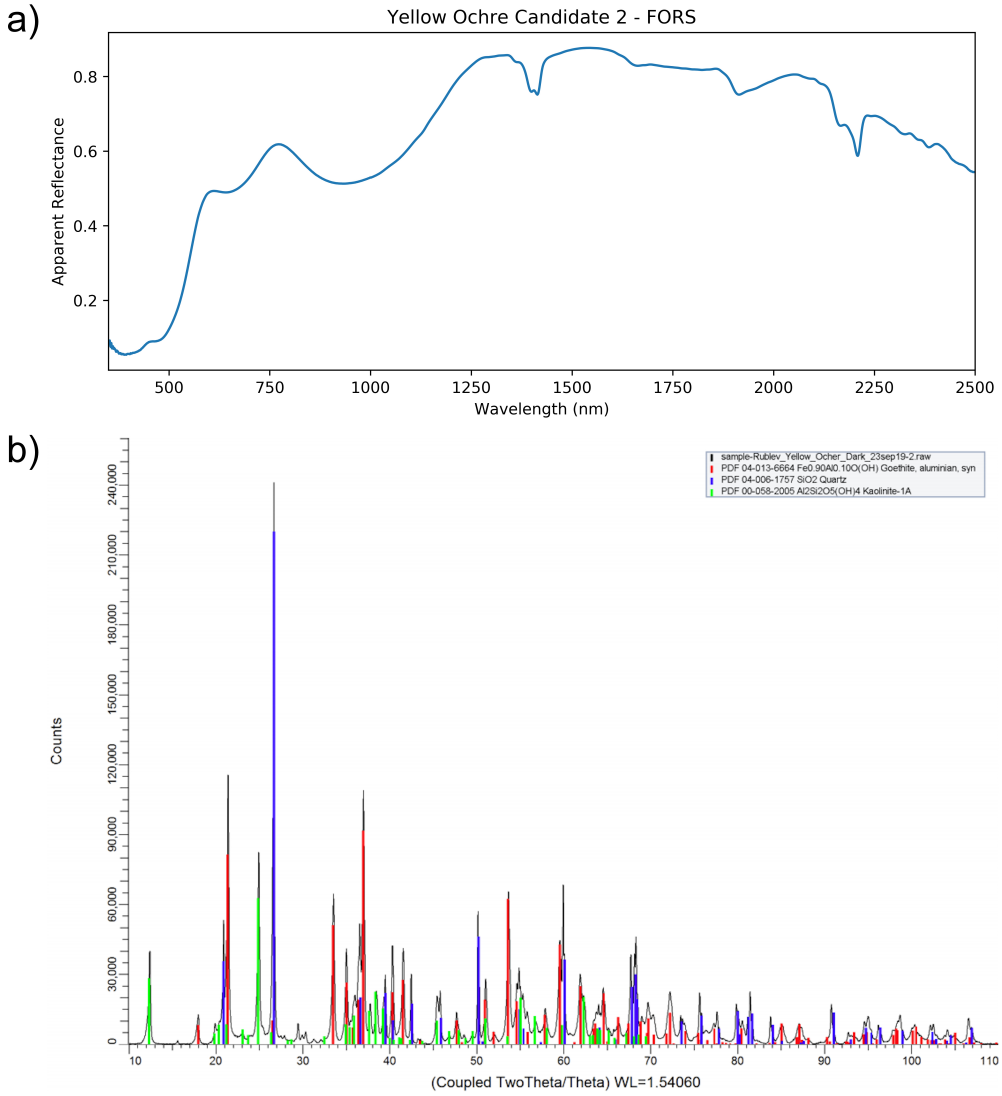

Figure 4.4: **a)**Results of the FORS analysis of the second yellow ochre candidate (Rublev Colours Yellow Ochre Dark) **b)**Results of the XRD analysis of the second yellow ochre candidate.

be seen in figure 4.5. The XRF found it to be almost purely Cu alongside minor amounts of Ca, Si, Al, P, K and Cl. The XRD found it to be pure azurite. The FORS results further reinforced that conclusion, showing all the reflectance features expected from azurite. The product was therefore chosen as the blue verditer pigment used for the samples. However, only a small amount was available and a new batch of it had to be ordered. Given that the initial sample was more than a decade old, it was decided to re-do

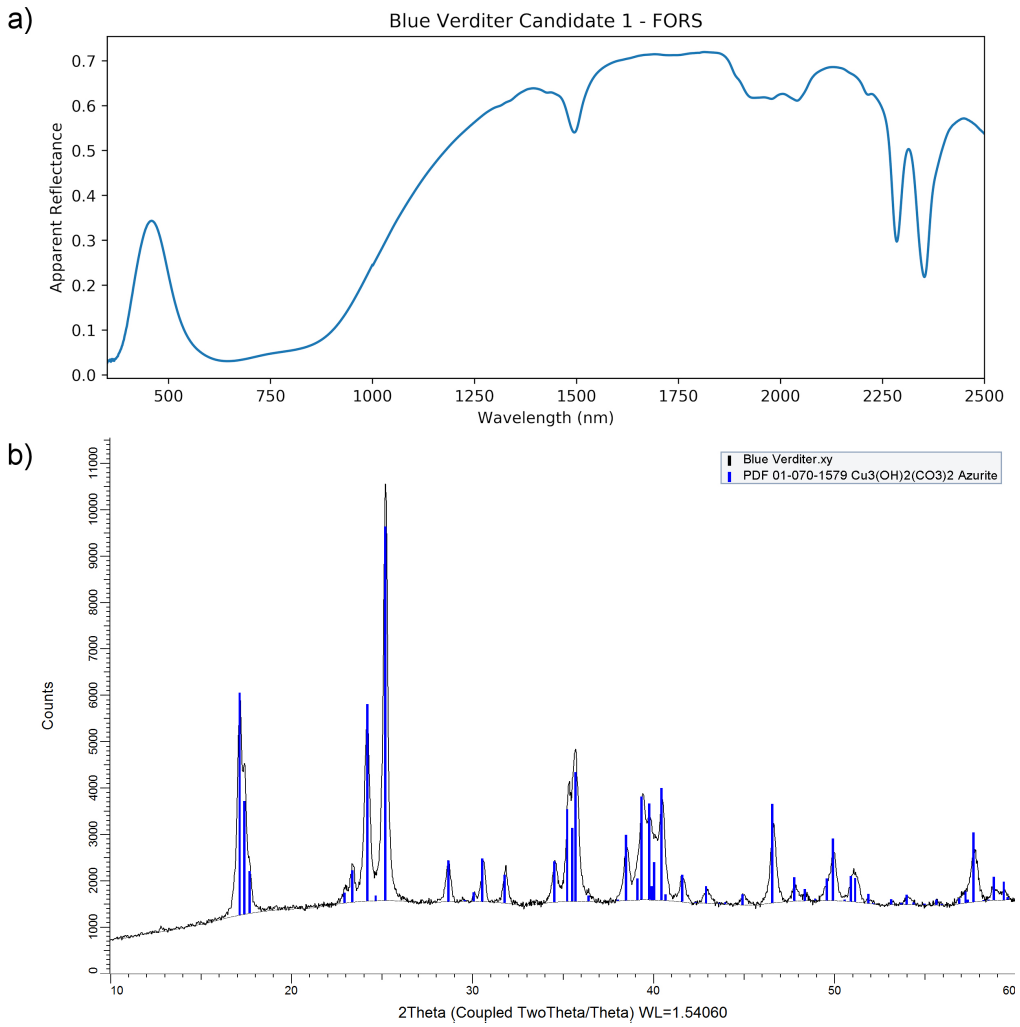

Figure 4.5: **a)**Results of the FORS analysis of the first blue verditer candidate (Rublev Colours Blue Verditer) **b)**Results of the XRD analysis of the first blue verditer candidate.

the analysis with the new batch, which was found to be identical to the original sample. The quantitative results of XRD analysis of the new batch can be found in table 4.3.

Table 4.3: Quantitative XRD results for the first blue verditer candidate (Rublev Colours Blue Verditer).

Compound	Formula	Weight Percentage (%)
Azurite	$Cu_3(CO_3)_2(OH)_2$	100

4.1.2 Paint Mixing

Having selected the source for each pigment, it was necessary to determine an appropriate paint mixing procedure as well as the appropriate pigment-to-binder ratios. The binder used was Kremer Raw Linseed Oil. The blue verditer and yellow ochre pigments came pre-ground, but the lead white came in a dry cake and had to be ground before mixing. To avoid any inconsistencies in the particle size distribution of the pigment, the entire amount of lead white pigment needed was ground in one process using a ceramic mortar and pestle. Characterization of the particle size distribution of the pigment in the paints was planned, but it was not possible to conduct due to logistical issues related to the 2020 COVID-19 pandemic.

The paint was mixed using a glass paint muller and it was decided to mix the paint in batches of 1-2g of pigment. The pigment was dispersed in the oil using the glass muller for about 5 minutes, after which the paint would be collected using a palette knife, and then dispersed again with the glass muller. This process would be repeated 3 times, at which point the paint was considered to be homogeneously mixed. For applications in which one of these batches would not provide enough paint, several batches would be prepared and then combined using a palette knife.

The pigment supplier provided a recommended pigment-to-binder ratio for each pigment. To verify whether this recommended ratio was appropriate, a test was conducted with the yellow ochre pigment. The recommended pigment-to-binder ratio for yellow ochre is 71:29 by weight (hereafter referred to as percentage of total paint weight, thus 29%). Paints using 25, 29, 35 and 40% were mixed and applied using a metal film applicator. The recommended ratio was found to have the best combination of handling and coverage when applied. It was therefore decided to use the recommended ratios for all the paints. However, the recommended ratio of 19% for blue verditer was found to be too dry requiring further testing. Ultimately, 22% was found to be a good ratio. The exact mixture ratios of the different paint batches are detailed in table 4.4. For paints which included more than one pigment, the corresponding pigments were first mixed into separate single-pigment paints using the method described earlier, and afterwards the separate paints were mixed together using a palette knife.

The paints are hereafter refered to by their constituent pigments using the abbreviations LW, YO and BV, for lead white, yellow ochre and blue verditer, respectively. Multi-pigment paints are refered to using the same pigment abbreviations separated by a slash (e.g. BV/YO).

4.1.3 Paint Application

As this research focuses on the effect of paint layering and composition on XRF and RIS spectra, it was decided to study these two aspects separately by creating one set of samples for each one. The two sets are referred to as the layer samples and the mixture samples. The design and preparation of each set of samples is now described.

The mixture samples consist of single-layer samples of different paint combinations at different ratios. To limit the number of samples, it was decided to test only combinations of two paints. Having three base paints to work with, 3 combination pairings are possible. 5 different mass ratios were chosen for each possible combination: 5%, 20%, 50%, 80% and 95%. It was decided to not do a uniform distribution, since that would provide little information on the edge cases, in which only a very small amount of one paint

Table 4.4: Paint Mixture ratios. The paints related to mixture samples were mixed in small batches in differing ratios and therefore an overall oil percentage is not applicable.

Application	Pigment type	Pigment (g)	Oil (g)	Oil Percentage (%)	Overall Oil Percentage (%)
Layer Samples (Underlying Layer)	YO	1.0	0.408	0.290	0.291
		1.2	0.493	0.291	
	BV	1.0	0.299	0.230	0.291
		1.4	0.395	0.220	
	LW	1.0	0.163	0.114	0.149
		1.8	0.326	0.153	
Layer Samples (Overlying Layer)	YO	1.5	0.608	0.288	0.288
		1.0	0.403	0.287	
	BV	1.5	0.422	0.220	0.220
		1.0	0.285	0.222	
	LW	1.5	0.245	0.140	0.142
		1.0	0.170	0.145	
Mixture Samples YO/BV	YO	1.7	0.703	0.293	n/a
	BV	1.7	0.472	0.217	
Mixture Samples YO/LW	YO	1.7	0.702	0.292	n/a
	LW	1.7	0.290	0.146	
Mixture Samples BV/LW	BV	1.8	0.508	0.220	n/a
	LW	2.0	0.346	0.147	

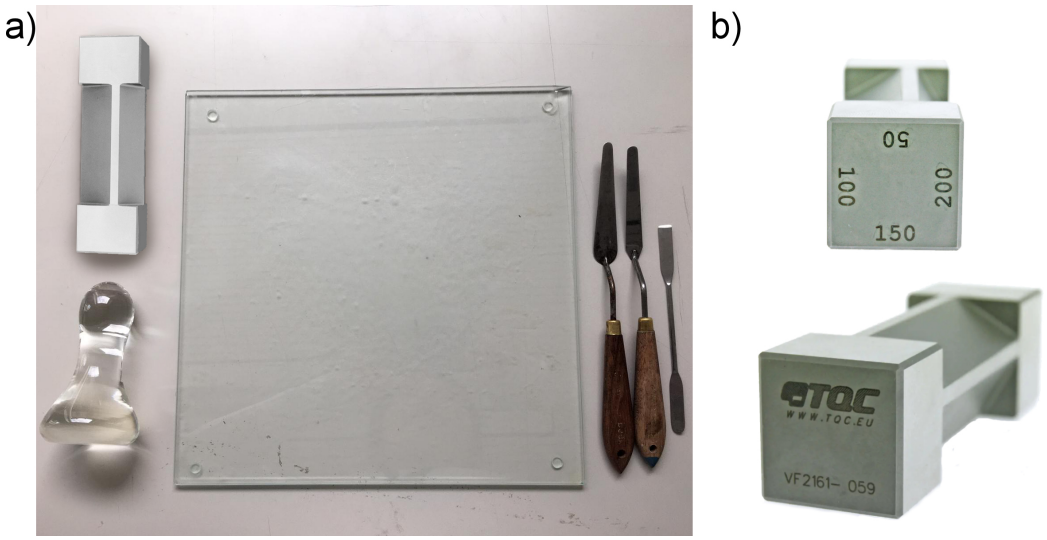

Figure 4.6: **a)**The equipment used for the paint mixing and application **b)**Detail views of the paint applicator.[72]

is mixed with a large amount of the other. For each mixture, 3 different paint layer thicknesses were applied: 50 µm, 100 µm and 150 µm. This resulted in a total of 45 discrete samples of varying thickness and composition.

All samples were produced using the same equipment, pictured in figure 4.6. To reduce the effect of the support on the XRF signal, a 50 µm Melinex film was used as support. The film was carefully cut into strips, ensuring as flat a surface as possible to avoid local variations in paint layer thickness. Each strip would be used for the three paint layer thickness samples for a specific paint mixture. The strips were attached to a white cardboard sheet for stability during application of the paint layers. The paint was applied using a metal 4-sided Bird-type film applicator with a fixed nominal film thickness on each side (50/100/150/200 µm). It is important to state that oil paint tends to shrink during drying, but how much the layer shrink depends on the composition of the paint. Therefore, for simplicity it was decided to refer to each sample using only the nominal thicknesses of the applicator used to apply the sample. Each sample is roughly 2x3 cm^2 in size. Once the paint was dry, the strips were detached from the cardboard sheet and cut to size. The strips were then attached to a 3 mm plexiglass sheet using photographic tape at both ends of the strip. The plexiglass sheet was expected to provide rigidity to the samples without greatly affecting the XRF results. The finished sample set can be seen in figure 4.7, together with a legend.

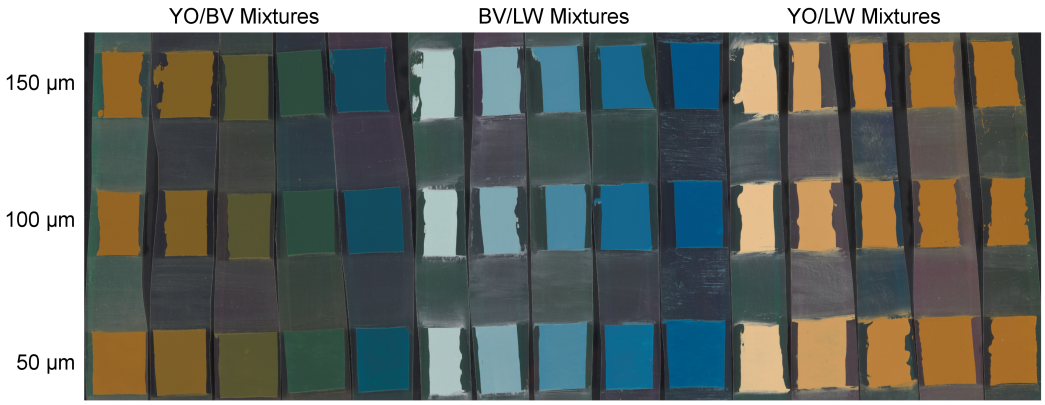

Figure 4.7: Visible light photograph of the mixture sample set. The samples are organized by their mixture and their thickness.

The layer samples consist of single-layer and double-layer samples of the base paints. The single layer samples are to provide a reference to compare the rest of the samples to. Three different layering arrangements were made: 50 µm over 50 µm, 50 µm over 100 µm and 100 µm over 50 µm. Since the order in which the paints are applied does matter, 3 base paints allow for 6 possible combination pairings. The layers were applied in two steps. First, the bottom layer was applied in the center and left to dry for a week. Second, at each end of the applied bottom layer, a top layer was applied, extending further than the edge of the bottom layer. The same film applicator used for the mixture samples was used. Given that the thickness of the applied film is measured with regards to the support, when applying the top layer it is necessary to consider the thickness of the already applied bottom layer. For example, when applying a 50 µm layer over a 50 µm layer, the applicator thickness used must be 100 µm (the sum of both layer thicknesses). The whole construct of the bottom layer and two top layers is referred to as a sample strip, a diagram of which can be seen in figure 4.8. Each sample strip has 5 samples, three single-layer samples and two double layer-samples. Each sample is roughly 2x2.5 cm^2 in size.

Since each sample strip includes two possible paint combination pairings, only one sample strip is required per layer arrangement per paint. However, as the two-step application process was more prone to failure, it was decided to prepare more sample strips than were strictly required, in case the application of the second layer did not work as expected. This was ultimately unnecessary as all layers were applied successfully, but it nevertheless proved useful at it provided more samples to verify the acquired data. Beyond the

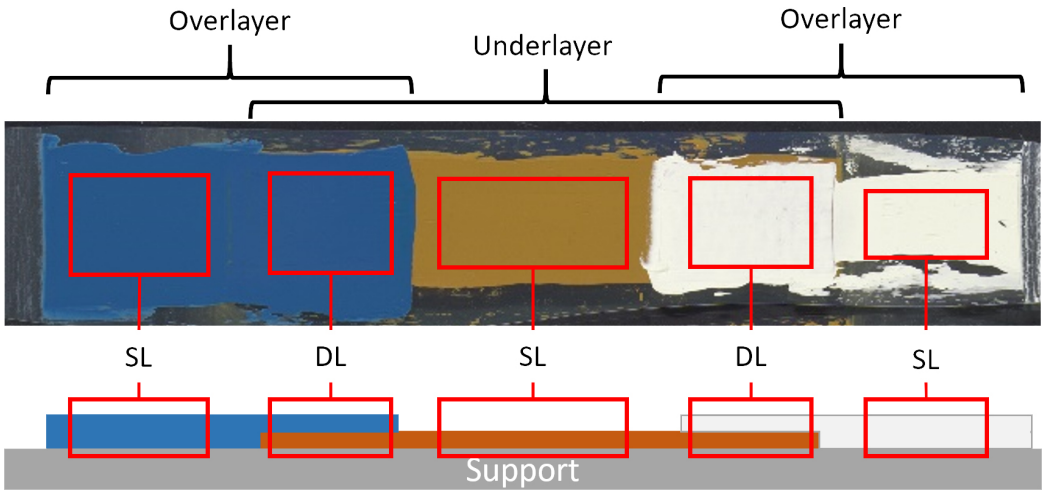

Figure 4.8: Diagram detailing the structure of the layer sample strips. Each sample strip has 3 single layer (SL) sampling areas and 2 double layer (DL) sampling areas.

two-step process, the samples were prepared using the same equipment and methods described for the mixture samples. The samples were organized by what paint was used for the bottom layer and for each paint there are two 50 µm over 50 µm samples, two 50 µm over 100 µm samples and one 100 µm over 50 µm sample. The finished sample set can be seen in figure 4.9, together with a legend. In total there are 75 samples, comprised of 27 different configurations. Because of how the samples were created, some sample configurations occur only once whilst others are repeated up to 6 times.

For part of the analysis, it was desired to know the areal density of both the pigments and the target elements present in the sample. This calculation was based on the concentration measurements from the XRD analysis, the recorded mixture ratios during the paint preparation and the nominal layer thicknesses. The pigment areal density of a sample $\rho_{A,C}$ is calculated using equation 4.1:

$$\rho_{A,C} = \sum_{l=L}^{H} w_{C,P,l} * \rho_{P,l} * d_l \tag{4.1}$$

Where the target paint component C (in this case the pigment) is composed of a number H of layers L of paint P, each with a target component concentration $w_{C,P,L}$ density $\rho_{P,L}$ and a thickness d_L. The paint density $\rho_{P,L}$ is calculated using equation 4.2:

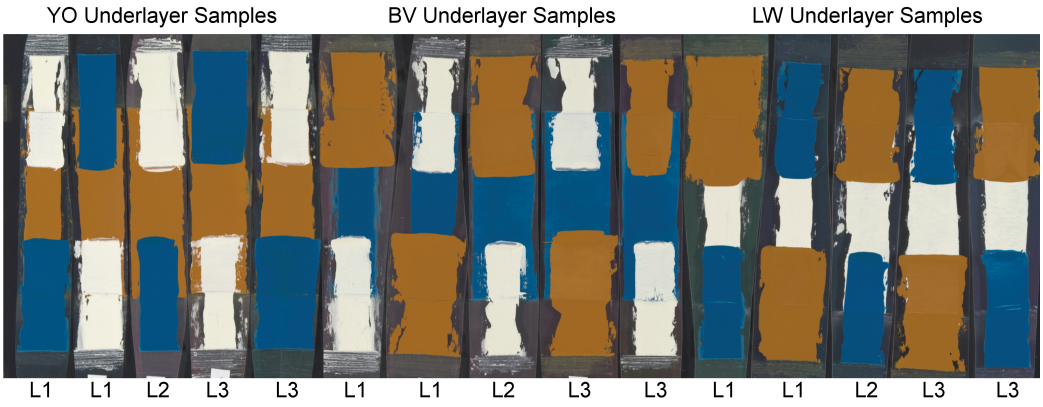

Figure 4.9: Visible light photograph of the layer sample set. The samples are organized by their underlayer and their layering configuration. (L1) denotes 50 µm over 100 µm, (L2) 100 µm over 50 µm and (L3) 50 µm over 50 µm.

$$\rho_{P,L} = \sum_{k=C}^{G} \rho_k * w_{k,P,L} \tag{4.2}$$

Where the paint P is composed of a number G of unique components C, each with a density ρ_C and concentration $w_{C,P,L}$. The paint component density ρ_C is calculated using equation 4.3:

$$\rho_C = \sum_{j=M}^{F} \rho_j * w_j \tag{4.3}$$

Where the paint component C is composed of a number F of unique molecules M, each with a density ρ_M and a concentration w_M. The values of ρ_M were taken from relevant databases.[73,74] For the areal density of a target element $\rho_{A,Z}$, equation 4.4 is used instead:

$$\rho_{A,Z} = \sum_{l=L}^{H} w_{Z,P,l} * \rho_{P,l} * d_l \tag{4.4}$$

Where the target element Z is present in a sample which is composed of a number H of layers L of paint P, each with a target element concentration $w_{Z,P,L}$, density $\rho_{P,L}$ and a thickness d_L. The concentration $w_{Z,P,L}$ is calculated using equation 4.5:

$$w_{Z,P,L} = \sum_{k=C}^{G} w_{Z,k} * w_k \tag{4.5}$$

Where the paint is composed of a number G of unique components C, each with a target element concentration $w_{Z,C}$, which is calculated using equation 4.6:

$$w_{Z,C} = \sum_{j=M}^{F} w_{Z,j} * w_j \tag{4.6}$$

Where the paint component is composed of a number F of unique molecules M, each with a target element concentration $w_{Z,M}$, which is calculated using equation 4.7:

$$w_{Z,M} = \frac{N_Z * m_Z}{\sum_{i=X}^{E} N_i * m_i} \tag{4.7}$$

Where the molecule M is composed of a number E of unique elements X, each present in an amount N_X and with an atomic mass m_X.

A sample of the calculated values can be seen in table 4.5, and the full results are availabe in Appendix A.

4.2 Scanning of Samples

The scan settings for the MA-XRF scans can be found in table 4.6. These settings were based on the settings chosen for the scanning campaign of Rembrandt van Rijn's *The Night Watch* currently ongoing at the Rijksmuseum.[51] The only difference was the pixel dwell time which was increased. This was done to provide the best possible statistics. These measurements could also be used to simulate lower dwell time measurements if it became necessary, but this was not the case. Initially, the samples were scanned in a horizontal position to avoid possible deformation of the samples due to gravity. The samples were placed on top of a stack of 6 plexiglass sheets (total thickness 12 mm) on a table. It was expected that the white coating on the table would include a white pigment, which would likely contain an element which would contribute to the XRF signal. It was therefore decided to include the stack of plexiglass sheets which were meant to separate the samples from the table and therefore reduce the possible contribution of the table on the

XRF signal. Although the plexiglass sheets were successful at reducing any elemental signal from the table, they also reflected a greater amount of the incident X-rays. A comparison of the XRF signal of a single plexiglass sheet and the stack of plexiglass sheets can be seen in figure 4.10.

One issue that arose during the scanning of the layer sample set was that the plexiglass sheets being used as a background were not large enough to support the entire sample set, meaning that there would not be a uniform effect on the background signal across the entire set. Although these differences in background signal would most likely be corrected by the SNIP filter during the fitting of the data, it was ultimately decided to play it safe and scan the sample sets vertically on an easel, which avoids this issue altogether.

Table 4.5: Calculated Pigment and Element Areal densities for the different paint mixtures. The single layer 100 µm samples have two possible values, depending on wether the layer was applied as an underlying layer or an overlying layer.

Sample	Thickness (µm)	Areal Density (g/cm^2)					
		YO	BV	LW	Fe	Cu	Pb
Single Layer YO	50	0.0094	0	0	0.0018	0	0
	100	0.0188	0	0	0.0036	0	0
		0.0189	0	0	0.0036	0	0
	150	0.0282	0	0	0.0055	0	0
Single Layer LW	50	0	0	0.0255	0	0	0.0204
	100	0	0	0.0509	0	0	0.0408
		0	0	0.0516	0	0	0.0413
	150	0	0	0.0768	0	0	0.0620
Underlayer YO	50	0.0094	0	0	0.0018	0	0
	100	0.0188	0	0	0.00362	0	0
Overlayer BV	50	0	0.0126	0	0	0.0070	0
	100	0	0.0252	0	0	0.0139	0
95% YO, 5% BV	50	0.0090	0.0005	0	0.0017	0.0003	0
	100	0.0180	0.0010	0	0.0035	0.0006	0
	150	0.0269	0.0016	0	0.0052	0.0009	0
80% YO, 20% BV	50	0.0078	0.0022	0	0.0015	0.0012	0
	100	0.0156	0.0043	0	0.0030	0.0024	0
	150	0.0234	0.0065	0	0.0045	0.0036	0
20% BV, 80% LW	50	0	0.0042	0.0185	0	0.0023	0.0149
	100	0	0.0085	0.0371	0	0.0047	0.0297
	150	0	0.0127	0.0556	0	0.0070	0.0446

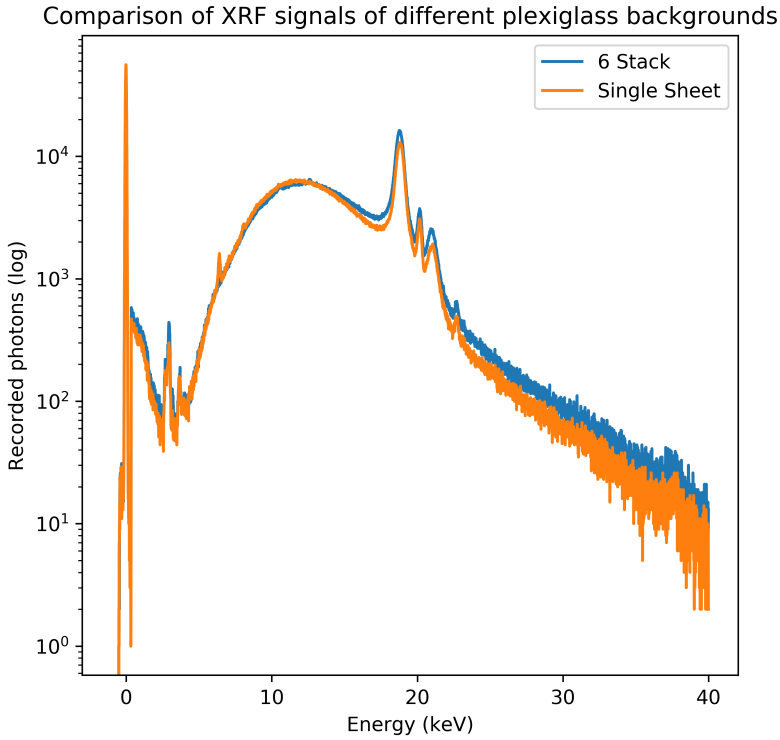

Figure 4.10: Comparison of the XRF signal of a single plexiglass sheet and a stack of plexiglass sheets. The 6 stack slightly increases the amount of reflected X-rays.

The deformation of the samples due to gravity is still a possibility, but it is considered to be unlikely enough that the benefits of vertical scanning outweigh such a risk. Particular care was taken during the data processing to account for possible deformations.

The scan setting for the RIS measurements can be found in table 4.7.

Table 4.6: MA-XRF Scan Settings. Values marked with * are default values

Settings	Value
Tube Current (µA)	200
Tube Voltage (kV)	50
Step Size (µm)	500
Dwell Time (ms)	400
Detector Range (keV)	40*
Optimal Countrate (kcps)	130*

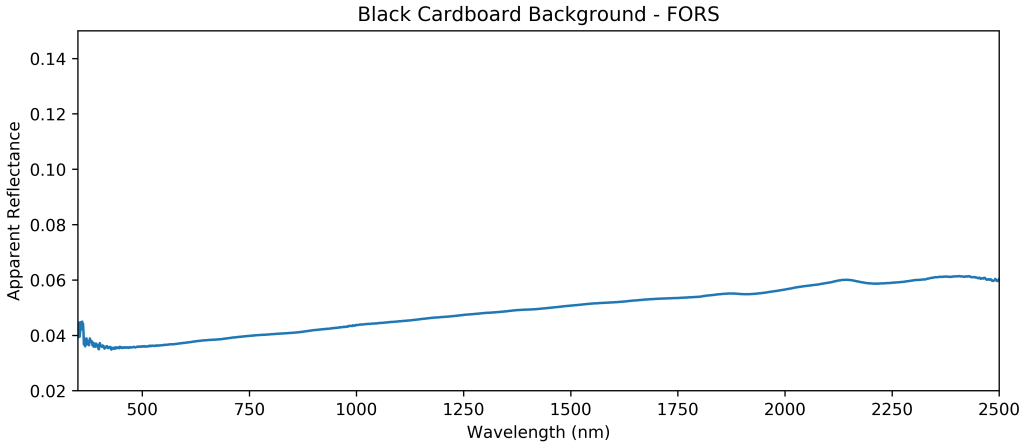

Figure 4.11: FORS measurement of the black cardboard used as a background for both sample sets.

These settings are the standard settings used for RIS analysis of paintings at the Rijksmuseum. The sample sets were scanned vertically using the automated easel. Because of the SWIR camera's vertical field of view being smaller than the height of the sample sets, the SWIR measurements required two scans per sample set. These two scans had a 20% vertical overlap to allow for stitching them into a single data set. The VNIR measurements did not have this problem and therefore required only one scan per sample set. Given that the melinex and plexiglass on which the samples are mounted are clear, a black cardboard was attached to the rear during the RIS scans to produce a consistent background. The black cardboard was analyzed with FORS to test its effect on the RIS signal before attaching and was found to have minimal signal in the VNIR and SWIR range. The resulting spectra is visible in figure 4.11. Even with the black cardboard, the melinex and plexiglass are expected to have an effect on the RIS signal, especially in the SWIR range, which must be considered during the analysis.

Table 4.7: RIS Scan Settings.

Setting	VNIR	SWIR
Camera Integration Time (ms)	200	120
Easel Integration Time (ms)	250	150
Easel Speed (mm/s)	0.72	1.12
Spatial Resolution (µm)	168	168
Light Intensity (lux)	1100	700

Chapter 5

Data Processing

This section covers the different data processing steps performed for the analysis of the MA-XRF and RIS data. After acquiring the data sets, the first thing to do was to align them, so that a direct comparison could be done between the different spectra. This was done using DataHandlerP's[75] OpenCV (Open Computer Vision library[76]) interface, which uses alignment features to perform the necessary transformations to align one data set onto another.[77] Given that the two acquired RIS data sets had a higher resolution than the MA-XRF data sets, it was decided to align the RIS data onto the MA-XRF data. This would decrease the size of the files significantly, making them much easier to use. The decrease in resolution also causes the averaging of the spectra of several pixels, which reduces the effect of measurement artifacts in single pixels.

The automatic feature detection of OpenCV did not provide enough unique features to properly align the data sets, for which some manual feature description was necessary. Around 30 alignment features were used to perform the transformations. The alignment of the data sets was not perfect and there were some deviations in the edges of the samples, but it was accurate enough to take the average spectra of each sample, given their homogeneity.

This alignment step was also used to stitch together the two SWIR measurements of each sample set. The two measurements of each sample set were aligned onto the corresponding MA-XRF datacube and these now aligned measurements were stitched together into a single datacube for each sample set. Since the measurements were now aligned onto a shared coordinate system, the stitching could be done using a very simple code which would find what pixels were empty in the first measurement and replace them with the corresponding pixel of the second measurement. This was done because it was believed that using a method like averaging the signal between the

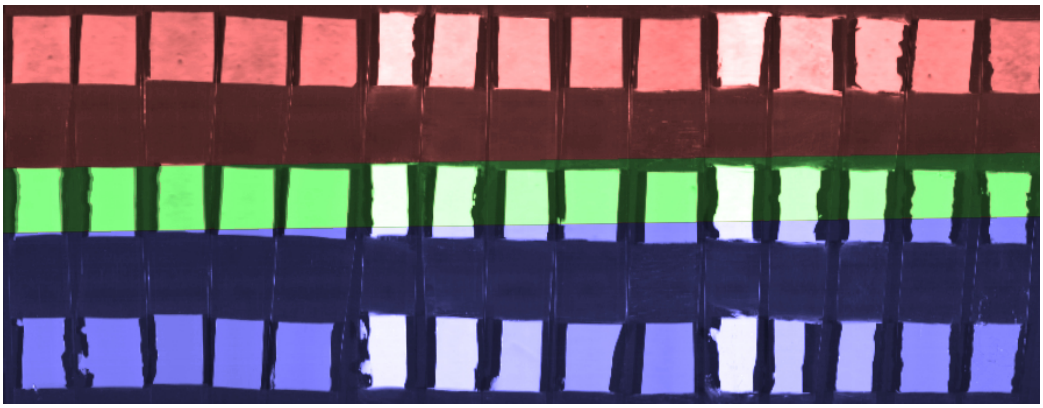

Figure 5.1: Diagram of SWIR dataset stitching method as applied to the scan of the mixture samples. The red and blue areas denote the two datasets and the green is their overlap. In the area of overlap, the values of the blue data set are disregarded and only the values of the red data set are used.

two measurements in the area of overlap could affect the amount of noise in the spectra in a manner which would make it inconsistent with the other areas of the datacube. Figure 5.1 shows a diagram exemplifying the stitching procedure.

Using the stitched RIS data sets it was possible to determine the reflectance spectra of the background. This is a combination of the Melinex, Plexiglass and black cardboard. These spectra are shown in figure 5.2. In the VNIR range, the background has almost no reflectance, with only around 0.05 normalized apparent reflectance throught the entire range. In the SWIR range, the background has a much more uneven reflectance, but it is still relatively low, staying below 0.2 normalized apparent reflectance, baring the high value at around 900 nm, This high value is an artifact and is present throughout the data set.

The MA-XRF data was processed as described in section 3.1.1. Given that the manual preparation of the samples left room for slight variations in the thickness of the applied paint layers, it was decided to define certain "sampling areas" which would provide relatively consistent paint areas for the analysis. These sampling areas were described using the processed MA-XRF maps, as they provided very clearly quantifiable comparison values. An initial estimation of these sampling areas was done manually, after which concentration maps were created for all the relevant elements for each sampling area and statistical data was collected. If an area was found to have clearly localized deviations, it would be slightly modified to remove them.

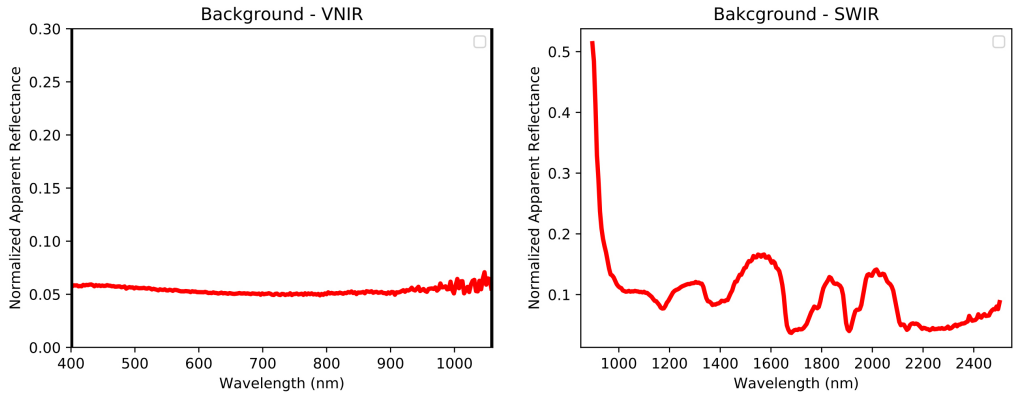

Figure 5.2: RIS measurement in VNIR and SWIR of the sample background (Melinex, Plexiglass and black cardboard).

A comparison between an initial area map and its modified version can be seen in figure 5.3. The final sampling areas can be seen in figure 5.4. Having these sampling areas defined, it was then possible to begin with the actual analysis of the results.

The data from the three methods are analyzed separately, in order to determine possible quantification procedures for each method.

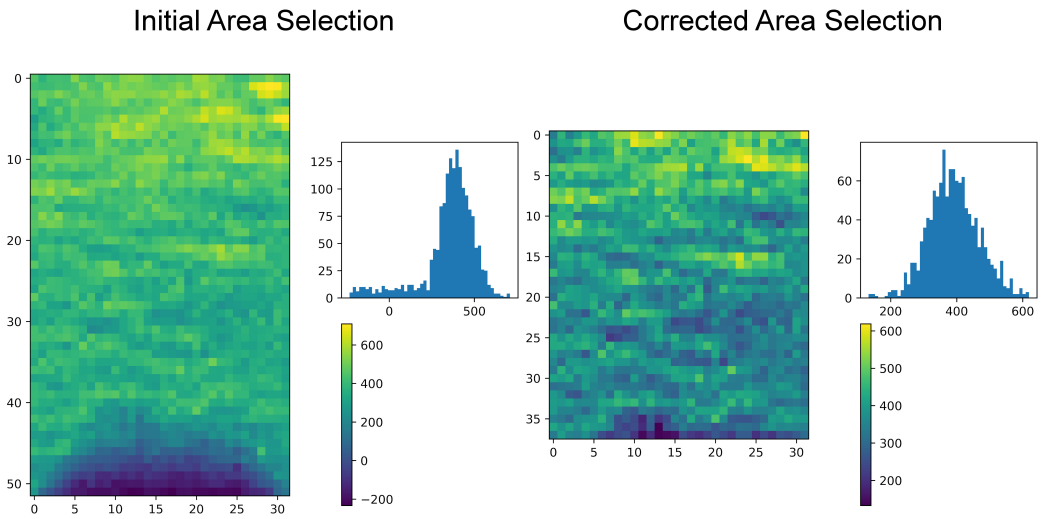

Figure 5.3: Example of sampling area selection procedure. First an initial area was manually defined. The area would then be modified based on the XRF maps to avoid sample irregularities.

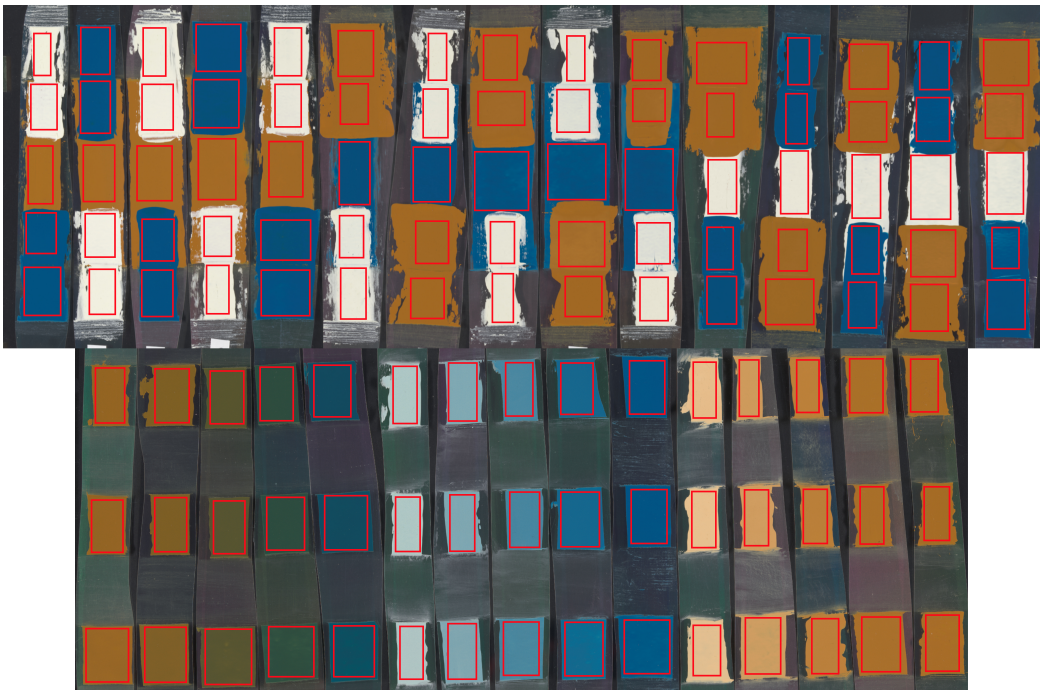

Figure 5.4: Map of the different sampling areas for layer and mixture samples.

5.1 MA-XRF

During the fitting of the data, 13 elements were identified in the spectra. For the analysis, only 3 elements will be taken into consideration, Fe, Cu and Pb, which are the marker elements for each pigment. Figure 5.5 includes the relevant elemental maps of the mixture samples, which show that the intensity of the XRF signal tends to be proportional to the areal density of each element (values of which are available in Appendix A). An exception to this is the Pb-M map which shows little change in intensity with increasing paint layer thickness and is instead only proportional to the elemental density of Pb in the paint.

The relation between elemental density in the paint can be more clearly seen in figure 5.6, which plots some paint mixture's XRF signal as a function of paint layer thickness. The behavior seen in these graphs is divided into two sections: the curved region, where the intensity of the signal is strongly related to the paint layer thickness, and the plateau region, where the intensity of the signal is not related to the paint layer thickness. These two sections are related to the self-absorption effect within the paint layers.

In the curved region, the entire depth of the paint layer contributes to the

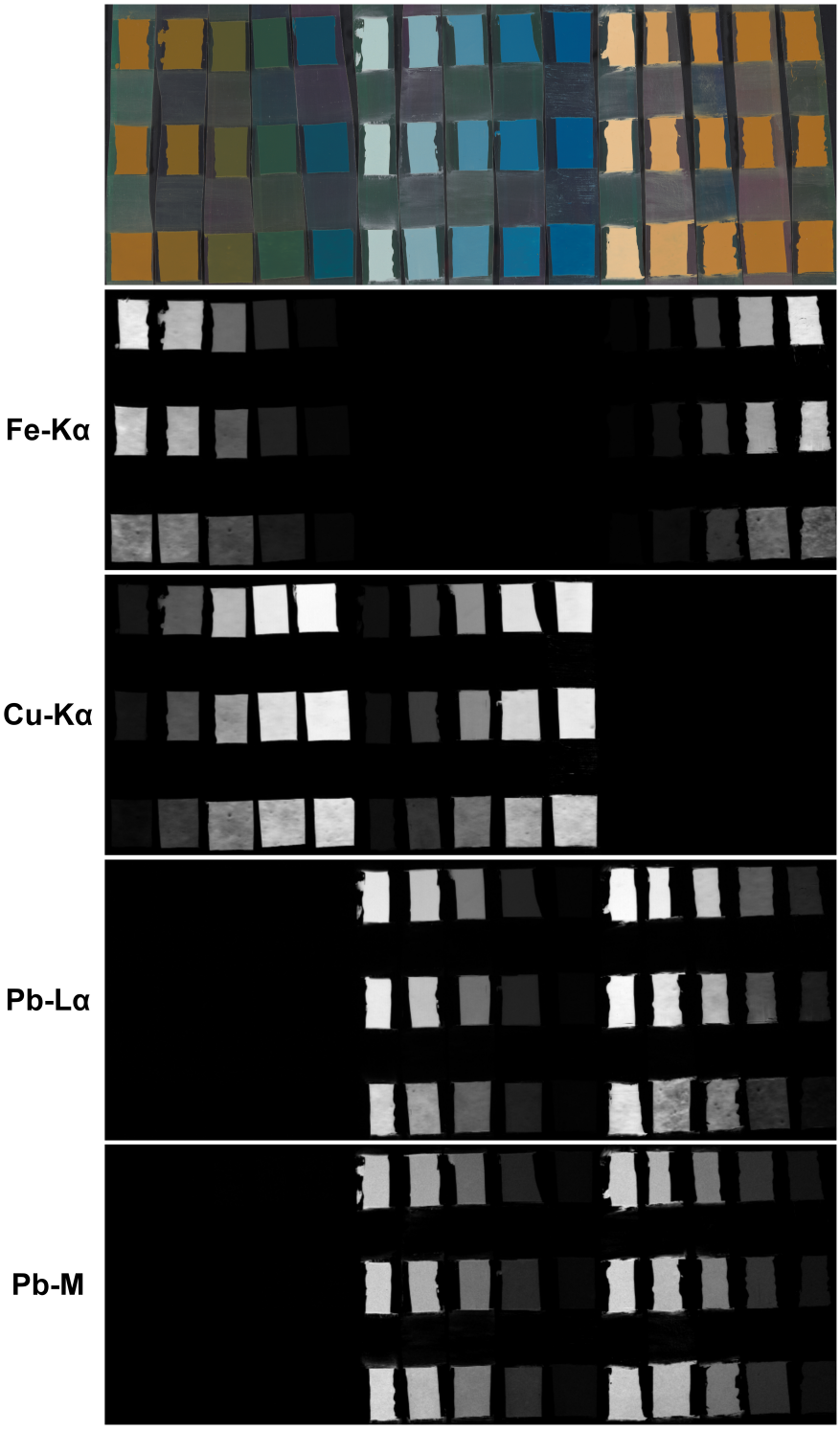

Figure 5.5: Most relevant MA-XRF maps of the mixture samples alongside a visible photograph for reference.

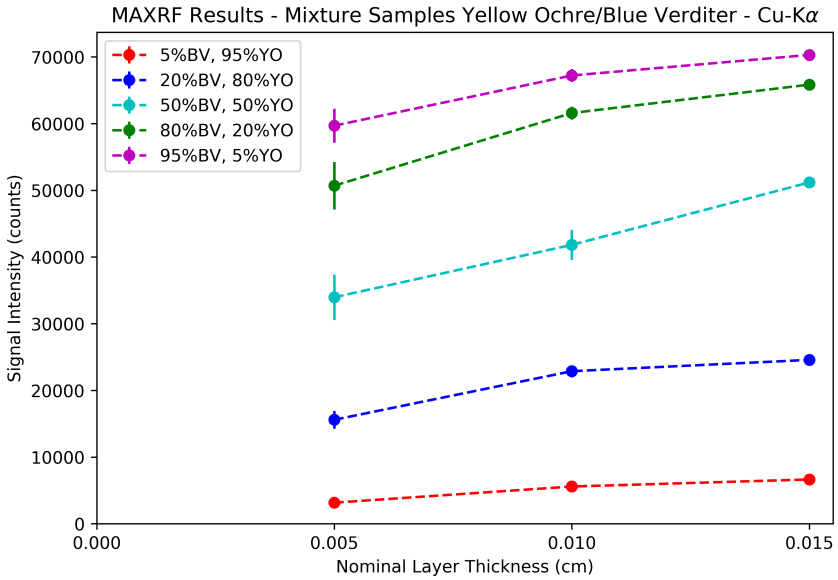

Figure 5.6: MA-XRF signal intensity of Cu-Kα for YO/BV samples.

signal. As the paint layer thickness increases, part of the characteristic X-rays emitted by the bottom parts of the paint layer begin to be absorbed by the top part of the paint layer. The thicker the paint layer, the more pronounced this absorption effect becomes, producing the curvature of this region. This continues until the point in which the characteristic X-rays emitted by the bottom part of the paint layer are fully absorbed by the top part of the paint layer. After this point, the plateau region is entered and an increase in paint layer thickness no longer directly affects the signal intensity. There are ways in which there can still be an indirect effect, but these will be covered later in this chapter. The width of the curved region and the height of the plateau region are characteristics dependent on certain fundamental factors related to the absorption and emission of X-rays by the elements present in the paint.

The first step in gathering quantitative values from the MA-XRF data was an attempt to model the behavior of the data using some of the known experimental variables and determine if it is possible to determine the remaining experimental variables using said model. The first attempt was based on a theoretical model for XRF signal intensity used by Alfeld for analysis of MA-XRF maps,[43] in which the signal intensity N_{ijk} (number of photons recorded) of a certain fluorescence line jk (transition k to a vacancy in shell j) of a certain element i in a paint layer can be described using equation 5.1:

$$N_{ijk} = t * m_i * Y_{ijk} * A_{ijk} \tag{5.1}$$

Where t is the measurement time, m_i is the irradiated mass, Y_{ijk} is the sensitivity and A_{ijk} is a term related to the self-absorption effect mentioned previously. m_i can be described using equation 5.2:

$$m_i = w_i * \left(\frac{b}{2}\right)^2 * \pi * \frac{d\rho}{\sin\alpha} \tag{5.2}$$

Where w_i is the weight fraction of the element, b is the beam spot diameter, d is the layer thickness, ρ is the density of the paint and α is the incidence angle of the primary beam on the paint surface. Y_{ijk} can be described using equation 5.3:

$$Y_{ijk} = \frac{\Omega}{4\pi} * \varepsilon\left(E_{ijk}\right) * \omega_{ijk} * p_{ijk} * \int_{E_{ij}^{Edge}}^{E_{max}} I_0\left(E\right) * \tau_{ij}\left(E\right) dE \tag{5.3}$$

Where Ω is the solid angle at which the radiation is recorded by the detector, E_{ijk} is the energy of the fluorescence line, $\varepsilon\left(E_{ijk}\right)$ is the detector efficiency for E_{ijk}, ω_{ijk} and p_{ijk} are the fluorescence yield and radiation rate of the measured transition, respectively. E_{max} is the maximum energy of a photon emitted by the source and E_{ij}^{Edge} is the energy of the elements absorption edge for the specific shell. $I_0\left(E\right)$ is the intensity of the primary beam and $\tau_{ij}\left(E\right)$ is the energy dependent elemental photoelectric cross section. The integral in the equation is a function of the emission profile of the X-ray source. Given that an emission profile for the X-ray source used was not available, equation 5.3 is simplified, and Y_{ijk} is instead described using equation 5.4:

$$Y_{ijk} = \frac{\Omega}{4\pi} * \varepsilon\left(E_{ijk}\right) * \omega_{ijk} * p_{ijk} * I_0\left(E_0\right) * \tau_{ij}\left(E_0\right) \tag{5.4}$$

Where E_0 is an assumed representative value for the energy of the primary beam. For this analysis, E_0 is taken as two times E_{ij}^{Edge}, which would ensure the assumed energy value is always able to trigger the transition and also provides somewhat of an average between lower energy X-rays, which are more strongly absorbed by the paint layers, and the higher energy X-rays, which are more weakly absorbed by the paint layers. $\varepsilon\left(E_{ijk}\right)$ depends on

the kind of detector used. For the SDD detector used in these experiments (described in section 3.1), $\varepsilon(E_{ijk})$ can be described using equation 5.5:

$$\varepsilon(E_{ijk}) = T_{Be}(E_{ijk}) * T_{DeadLayer}(E_{ijk}) * (1 - T_{volume}(E_{ijk})) \tag{5.5}$$

$T(E_{ijk})$ is the energy dependent transmission of the three layers of the detector ($T_{Be}(E_{ijk})$ for the Be window, $T_{DeadLayer}(E_{ijk})$ for the dead layer on the sensitive volume of the detector and $T_{volume}(E_{ijk})$ for the sensitive volume of the detector) and is described using equation 5.6:

$$T(E) = e^{-\mu(E)\rho d} \tag{5.6}$$

Where μ is the energy dependent mass absorption coefficient. Information on the thickness of the detector layers was unavailable and therefore assumed values were taken based on similar detectors and recommendations from scientists from the field. The thicknesses taken were 30 µm, 450 µm and 0.05 µm for the Be window, sensitive volume of the detector and the dead layer, respectively.

A_{ijk}, like Y_{ijk}, is also a function of the emission profile of the X-ray source, and therefore the same simplification was done, which results in equation 5.7:

$$A_{ijk} = \frac{1 - e^{-\chi\left(E_0, E_{ijk}\right)\rho d}}{\chi(E_0, E_{ijk})\,\rho d} \tag{5.7}$$

Where χ is a factor for the geometrically corrected mass absorption coefficients for primary and fluorescence radiation, described using equation 5.8:

$$\chi(E_0, E_{ijk}) = \mu(E_0)\frac{1}{\sin(\alpha)} + \mu(E_{ijk})\frac{1}{\sin(\beta)} \tag{5.8}$$

Where β is the angle between the paint surface and the detector. When calculating χ, the initial assumption of E_0 can have a significant effect on the accuracy of the calculated values, as the mass absorption coefficient of the paint can vary significantly between different energies.

Out of all the factors used in the calculation, most are known values or reasonable assumptions as to their value can be taken. The only two values where this is not the case are $I_0(E_0)$ and Ω. All other values are related

either to the sample, the measured fluorescence line or to the measurement settings. With that in mind, and given that writing the full formula would be cumbersome, for this research equation 5.1 is instead written as equation 5.9:

$$N_{ijk} = A * K_M * K_{ijk} * w_i * \frac{1 - e^{-\chi\left(E_0, E_{ijk}\right)\rho d}}{\chi\left(E_0, E_{ijk}\right)} \tag{5.9}$$

with

$$K_M = t * \left(\frac{b}{2}\right)^2 * \frac{1}{\sin\alpha} * \frac{1}{4} \tag{5.10}$$

$$K_{ijk} = \varepsilon\left(E_{ijk}\right) * \tau_{ij}\left(E_0\right) * \omega_{ijk} * p_{ijk} \tag{5.11}$$

$$A \propto I_0\left(E_0\right) * \Omega \tag{5.12}$$

K_M is a factor related to the test settings and is a constant throughout all measurements in this research. K_{ijk} is a factor related to the emission and detection measured fluorescence line and is a constant for each fluorescence line. A is an empirical factor which allows to fit the model to the acquired data and to correct for the unknown values $I_0\left(E_0\right)$ and Ω. The remaining terms in equation 5.9 are related to the specific sample. It is important to note that μ, and therefore χ, is a function of w_i. In the calculations for this research, the value of μ for each of the tested paint compositions is calculated using the library XRAYLIB,[78] the processes of which are described by Schoonjans et al.[79]

A code was written to determine the appropriate values for A. This code used a data set consisting of the average XRF signals of one fluorescence line for one group of the mixture samples (YO/BV, BV/LW or YO/LW) to find an appropriate value for A, which was initially assumed to be constant for each of these data sets. An example of these results can be seen in figure 5.7. It can be seen that the model lines have roughly the correct shape described earlier, but they fail to fit well with the data points used, either in the curvature or plateau region. Given that A should only have an effect on the overall height of the plateau region and not on the curvature of the curved region, it is believed that there was something wrong in the determination of χ. Several attempts were made to address these issues, but none were

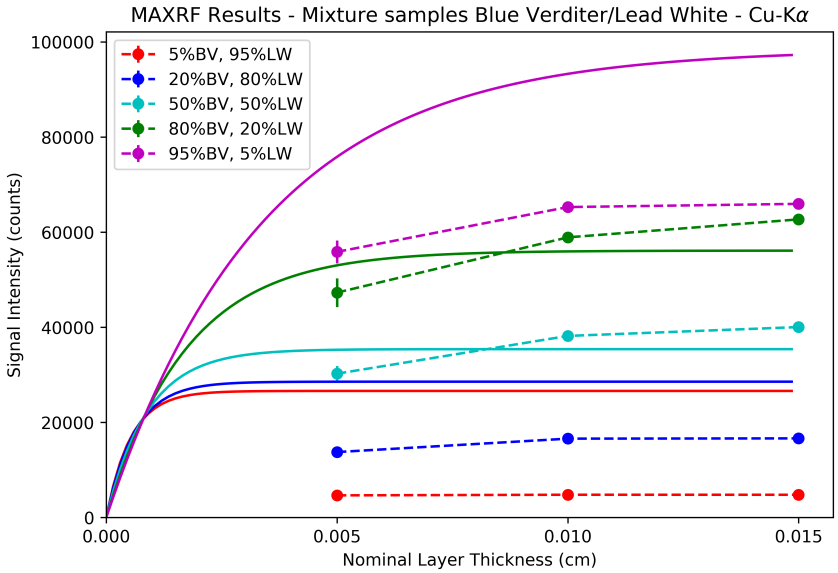

Figure 5.7: MA-XRF signal intensity of Cu-Kα for BV/LW samples and the initial model.

successful. It was assumed that this discrepancy is a result of the initial simplifications of the theoretical model and the assumptions made about the value of E_0. Because of this, it was decided to instead to use a further simplified version of the model which is only a function of d, fit it to the data using empirical factors, and determine if it is possible to extract certain known experimental values from these factors. The model is described by equation 5.13:

$$N = A * \left(1 - e^{-B*d}\right) \tag{5.13}$$

A and B are empirical factors which are calculated for each individual paint mixture. As can be seen in figure 5.8, the described system fits the data set more closely. Based on the relation between equation 5.9 and equation 5.13, the value of A should, in theory, be directly proportional to w_i and inversely proportional to χ. To verify this, the relation between the different A values was studied using equation 5.14:

$$w_{i,Th} = \frac{\frac{A_x}{\chi_{x,Th}}}{\frac{A_{95\%}}{\chi_{95\%,Th}}} \tag{5.14}$$

Where $w_{i,Th}$ is the theoretical calculated weight fraction for the measured

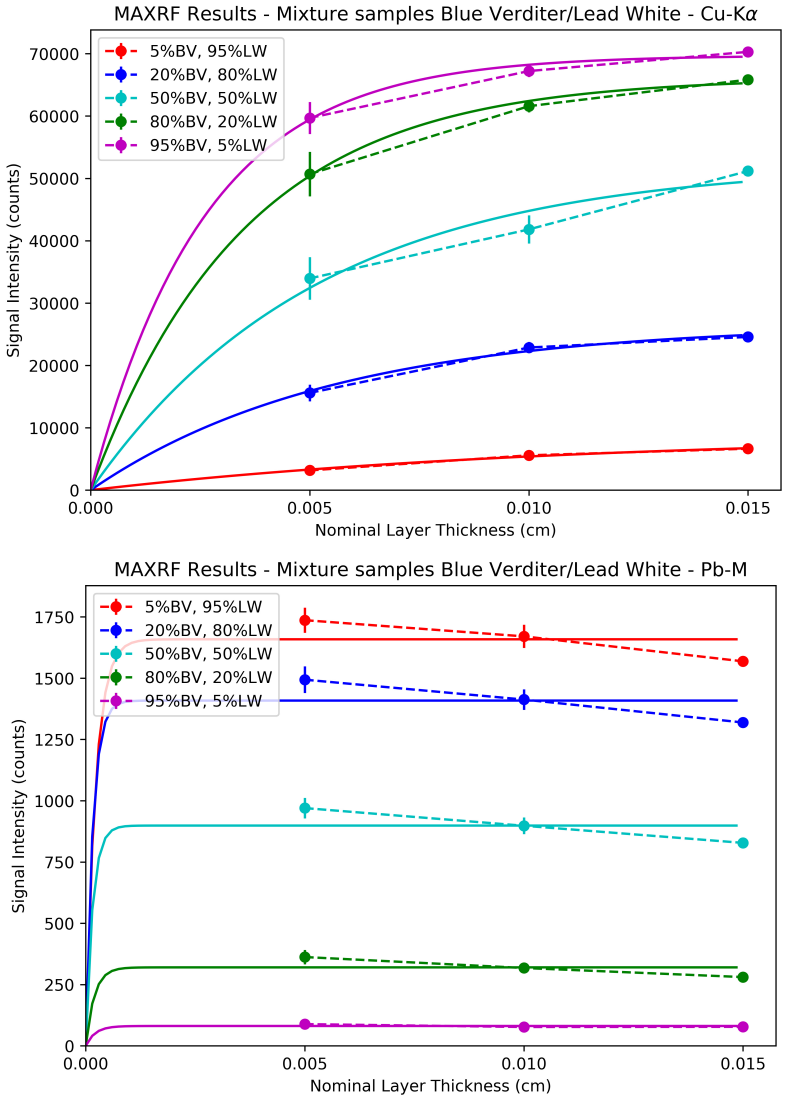

Figure 5.8: MA-XRF signal intensity of Cu-Kα and Pb-M for BV/LW samples and the improved model.

element, A_x is the A value for a given paint mixture in which the paint related to the measurement is at concentration x, $\chi_{x,Th}$ is the calculated χ value for the same paint, $A_{95\%}$ is the A value for the paint mixture of the corresponding group with a paint concentration of 95% and $\chi_{95\%,Th}$ is the calculated χ value for that paint. In order to make the results easier to read, the $w_{i,Th}$ values calculated are turned into paint concentration percentages by multiplying them by 0.95. Part of results can be seen in table 5.1. The full results can

be found in appendix B.

As can be seen, for certain elemental lines in certain paint combinations, like Fe-Kα in YO/BV or Pb-Lα in BV/LW, the results are relatively accurate, being only 7% off in the worst case. In some other cases, like Cu-Kα in YO/BV, the calculated values are not accurate, but they roughly follow the same increasing pattern of the real values. However, in other cases, like Cu-Kβ in BV/LW, the calculated values in no way relate to the real values.

A line which is of particular interest is Pb-M. The low energy (0.58-3.74 keV) of this line means that it is highly absorbed by a paint layer, which leads to the curvature region being very narrow. The results of the model, pictured in figure 5.8, show such a behavior. However, it is possible to see the model does not fit the measurement that well. In the measurement, the intensity of the Pb-M signal decreases with increasing layer thickness for all 5 paint mixtures. This behavior is not what is expected from any XRF signals and, as can be seen in figure 5.8, the used model does not allow for a decrease in signal. The reason behind this behavior is believed to be related to sensor dead time, which is the time in which the sensor is unable to record an event because it is busy recording a simultaneous event. In Pb containing paints, the increase in layer thickness leads to a dramatic increase in signal intensity for the Pb-L lines, which could be saturating the sensor. However, as can be seen in table 5.1, the calculated concentrations match the actual values fairly well, with the largest error being of $<5\%$. This would imply that either the effect of dead time is close to linear within the tested mixture groups or the fitting method used is not affected by it.

The dead time is most often expressed as the percentage of time in which the sensor is unresponsive and is a function of the input rate and their relation is non-linear.[43] Because of this, it is fairly unexpected for the dead time to have such a uniform effect across the different paint mixtures, as the different paints are expected to have significant differences in X-ray emission. Therefore, it would be safe to assume that dead time has a non-uniform effect across the measurement that affects the signal of all fluorescence lines in different ways. However, looking at figure 5.8, it can be seen that, at least for Pb-M, even though the intensity of the effect varies with the concentration, it seems to have a nearly linear relation with paint layer thickness.

Given the limited information on the X-ray source, it is not possible to accurately determine the exact effect of sensor dead time. However, during the later stages of this research, a new version of DataMuncher was released which included a function to correct for dead time. The data was processed

Table 5.1: Results of the concentration calculations based on the MA-XRF model.

Fluorescence Line	Mixture	Theoretical Composition (%)	Calculated Composition (%)	Error (%)
Fe-Kα	YO/LW	95	95.00	0.00
		80	99.66	19.66
		50	49.96	0.04
		20	16.57	3.43
		05	04.28	0.72
	YO/BV	95	95.00	0.00
		80	79.29	0.71
		50	53.83	3.83
		20	21.48	1.48
		05	05.59	0.59
Cu-Kα	BV/LW	95	95.00	0.00
		80	159.17	79.17
		50	162.09	112.09
		20	83.28	63.28
		05	25.32	20.32
	YO/BV	95	95.00	0.00
		80	89.50	9.50
		50	69.54	19.54
		20	34.37	14.37
		05	11.43	6.43
Cu-Kβ	BV/LW	95	95.00	0.00
		80	167.92	87.92
		50	181.80	130.80
		20	98.35	78.35
		05	32.59	27.59
	YO/BV	95	95.00	0.00
		80	89.76	9.76
		50	70.92	20.92
		20	33.51	13.51
		05	10.12	5.12
Pb-Lα	YO/LW	95	95.00	0.00
		80	96.07	16.07
		50	69.04	19.04
		20	26.08	6.08
		05	10.97	5.97
	BV/LW	95	95.00	0.00
		80	79.43	0.57
		50	45.72	4.28
		20	13.03	6.97
		05	01.83	3.17

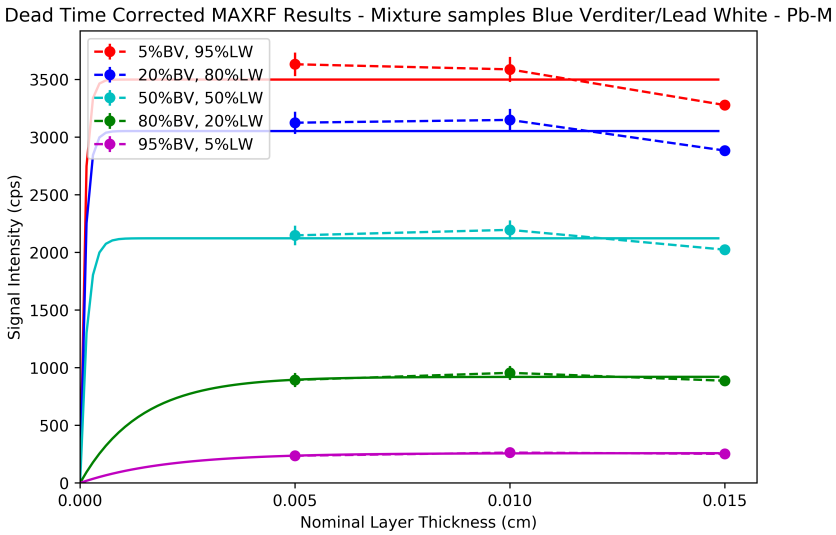

Figure 5.9: MA-XRF dead time corrected signal intensity for Pb-M in BV/LW samples and the improved model.

again using this dead time correction and the same analysis was conducted. Part results of this analysis are presented on table 5.2. The full results are available in appendix C. This correction helps increase the accuracy of some of the measurements, like Cu-Kα in YO/BV, but also decreases the accuracy in others, like Fe-Kα in YO/BV. The results which did not relate to the real values in any significant way were not greatly affected by this correction. Figure 5.9 shows the fitted lines for Pb-M in BV/LW, which makes it easy to see that the dead time correction does indeed make the values more closely resemble what would be expected of these signals, with the values either remaining stable or slightly increasing with an increase in thickness from 0.005 cm to 0.01 cm. However, the Pb-M signal still experiences a drop at 0.015 cm throughout all measurements, which means the dead time correction is not working quite as well as would be desired.

During the analysis of the single layer samples, the non-linear relation between the areal density of the elements and the intensity of the XRF signal was further proven. Figure 5.10 shows this relation for a few of the lines. Figure 5.10.a shows that it is not possible to determine areal density from the XRF signal intensity of a single element alone. It is also possible to see that the plotted results could be divided into groups related to the different paint layer thicknesses (most visible in the Pb-M signal). To better show the relation between the two factors, figure 5.10.b shows only the results for one paint layer thickness for the specific fluorescence lines. In all cases,

Table 5.2: Results of the concentration calculations based on the MA-XRF model using the dead time corrected data.

Fluorescence Line	Mixture	Theoretical Composition (%)	Calculated Composition (%)	Error (%)
Fe-Kα	YO/LW	95	95.00	0.00
		80	91.80	11.80
		50	47.09	2.91
		20	16.32	3.68
		05	04.19	0.81
	YO/BV	95	95.00	0.00
		80	87.92	7.92
		50	83.04	33.04
		20	39.91	19.91
		05	11.41	6.41
Cu-Kα	BV/LW	95	95.00	0.00
		80	168.94	88.94
		50	117.15	67.15
		20	52.93	32.93
		05	15.33	10.33
	YO/BV	95	95.00	0.00
		80	80.76	0.76
		50	52.83	2.83
		20	18.76	1.24
		05	05.64	0.64
Pb-Lα	YO/LW	95	95.00	0.00
		80	98.75	18.75
		50	68.52	18.52
		20	24.99	4.99
		05	12.46	7.46
	BV/LW	95	95.00	0.00
		80	83.55	3.55
		50	54.30	4.30
		20	20.28	0.28
		05	02.97	2.03
Pb-M	YO/LW	95	95.00	0.00
		80	80.17	0.17
		50	48.21	1.79
		20	16.18	3.82
		05	05.56	0.56
	BV/LW	95	95.00	0.00
		80	81.27	1.27
		50	53.55	3.55
		20	21.25	1.25
		05	05.55	0.55

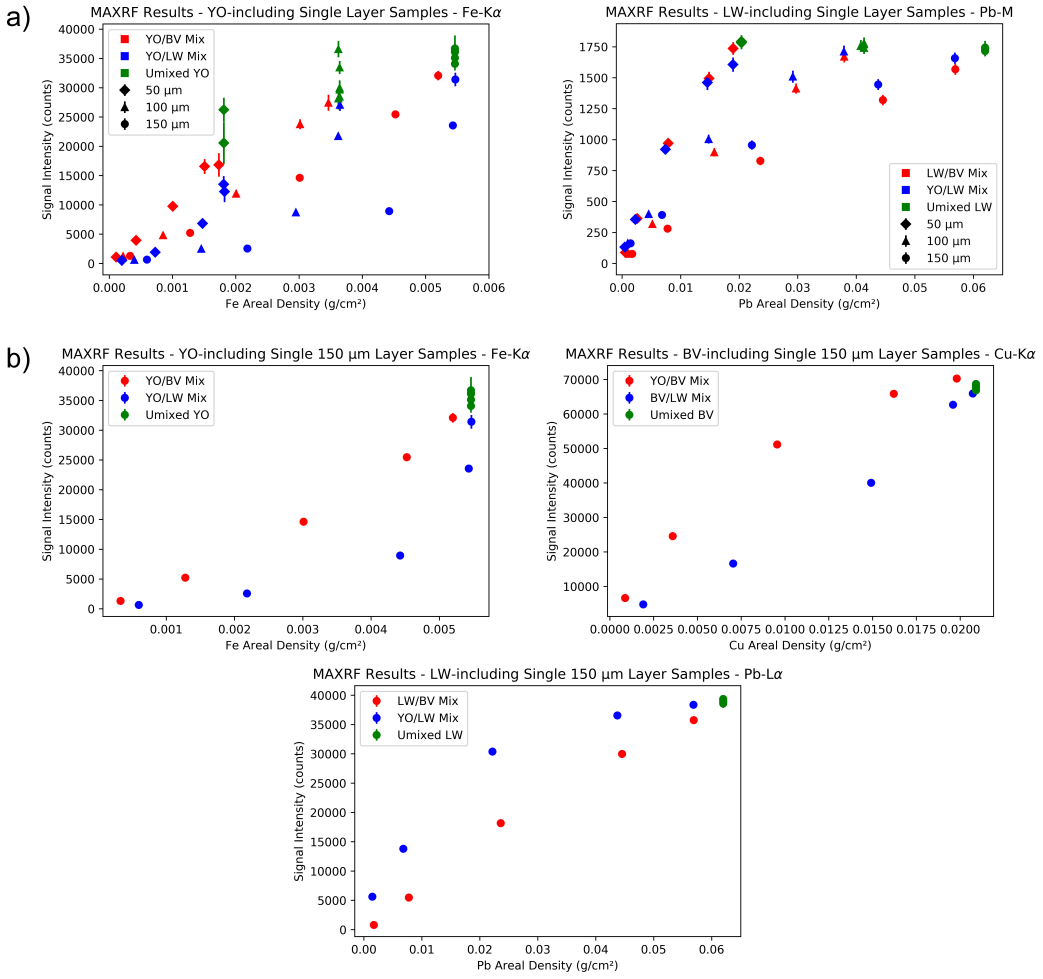

Figure 5.10: Relation between areal density and XRF signal intensity for **a)** all single-layer samples and **b)** 150 µm single layer samples.

the measurements follow a curve between the origin (0,0) and the signal of the single-pigment paint. The shape of the curve is determined by the mass absorption coefficients of the mixed paints. If the paint related to the element being measured is mixed with a paint with a lower mass absorption coefficient than its own, the curve is downward facing (concave downward or concave). If instead, it is mixed with a paint with a higher mass absorption coefficient, the curve is upward facing (concave upward or convex). How pronounced the curvature is depends on how high the absolute value of the difference of the mass absorption coefficients of the two paints are. In some cases, like YO/BV mixture, the effect on the signal intensity of the Cu-Kα line from a reduction of the mass absorption coefficient of the paint is more significant

than the effect from reducing the elemental density, leading to the highest signal intensity being related to a sample with a lower amount of Cu.

The MA-XRF maps of the layer samples, seen in figure 5.11, clearly show the effect of layering on the signal intensity. The presence of thick single-pigment paint layers provides a useful reference from which it is easily seen that the presence of an overlying layer reduces the signal intensity of the underlying layer and sometimes completely blocks it. The exact effect depends on the overlying layer's mass absorption coefficient and thickness. The results confirm that, as expected, increasing the thickness of the overlying layer or its mass absorption coefficient decreases the signal intensity of the underlying layer. However, the lack of a good reference point when analyzing a painting makes drawing such conclusions much more complicated.

Equation 5.15, a modified version of equation 5.1, allows for the consideration of the effect of overlying paint layers on the XRF signal intensity:[43]

$$N_{ijk} = t * m_i * Y_{ijk} * A_{ijk} * A'_{ijk} \tag{5.15}$$

With A'_{ijk} a term related to the absorption of the overlying layers defined by equation 5.16:

$$A'_{ijk} = e^{-\chi'\left(E_0, E_{ijk}\right)\rho' d'} \tag{5.16}$$

Where χ', ρ' and d' are the geometrically corrected mass absorption, the density and the thickness of the overlying layer, respectively. χ' is calculated using equation 5.8 but using the μ values of the overlying layer (μ').

From the previous attempt to model single layers, it was known that too many variables were unknown to be able to accurately describe the XRF signal behavior. Based on that fact and also the limited number of samples available, it was decided to not attempt to model this behavior as the results would, at best, be similar to those described for the single-layer samples. However, comparing the signal of the samples available does provide some valuable insight. Figure 5.12 shows a comparison between different samples containing 50 µm layers of the paint related to each elemental fluorescence line. Signals coming from underlying layers are less intense than those coming from surface layers and the degree by which the signal is blocked depends on the mass absorption coefficient of the overlying layer, which matches the theoretical model described earlier. The behavior of surface layers is slightly more complicated.

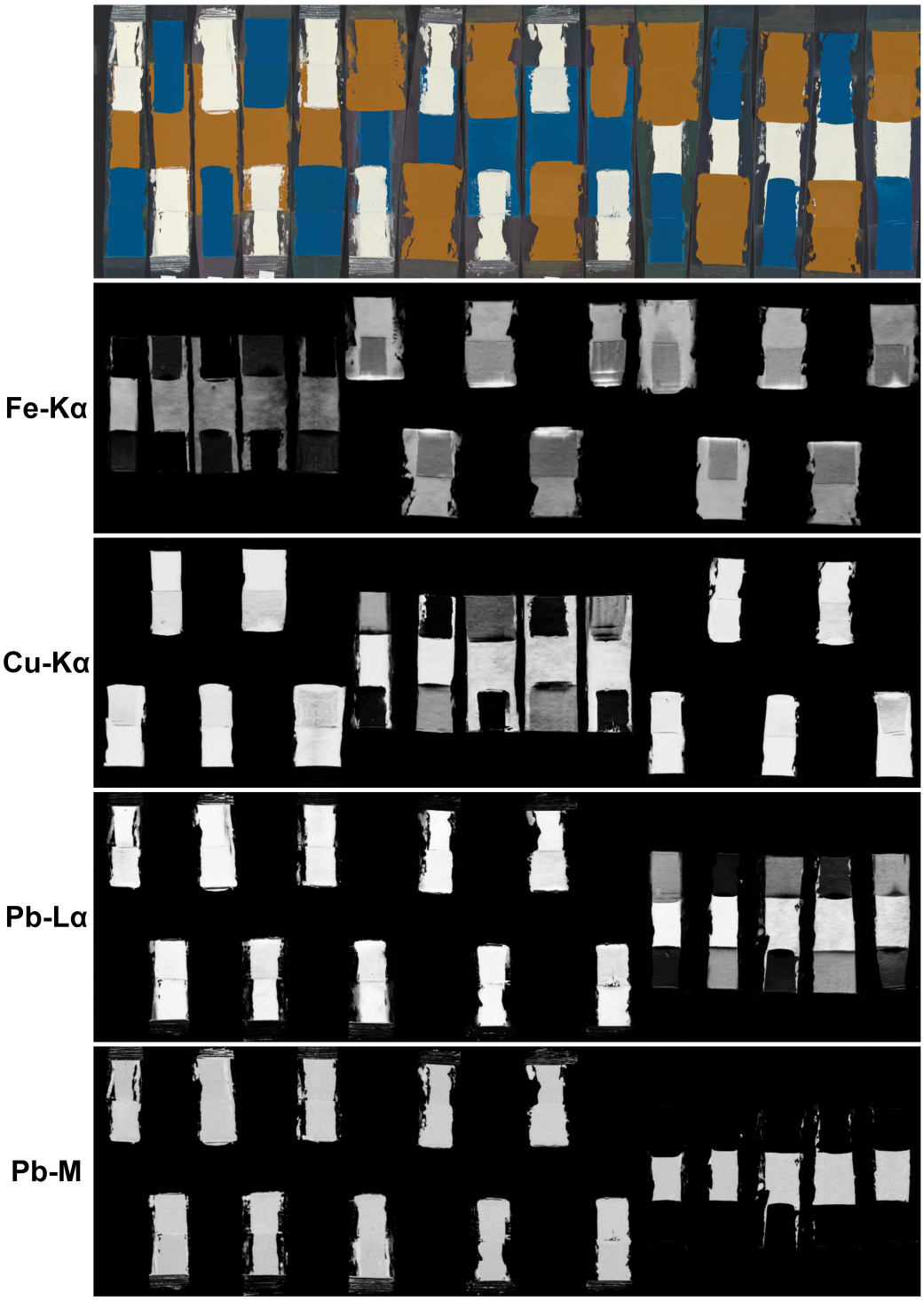

Figure 5.11: Most relevant MA-XRF maps of the layer samples alongside a visible photograph for reference.

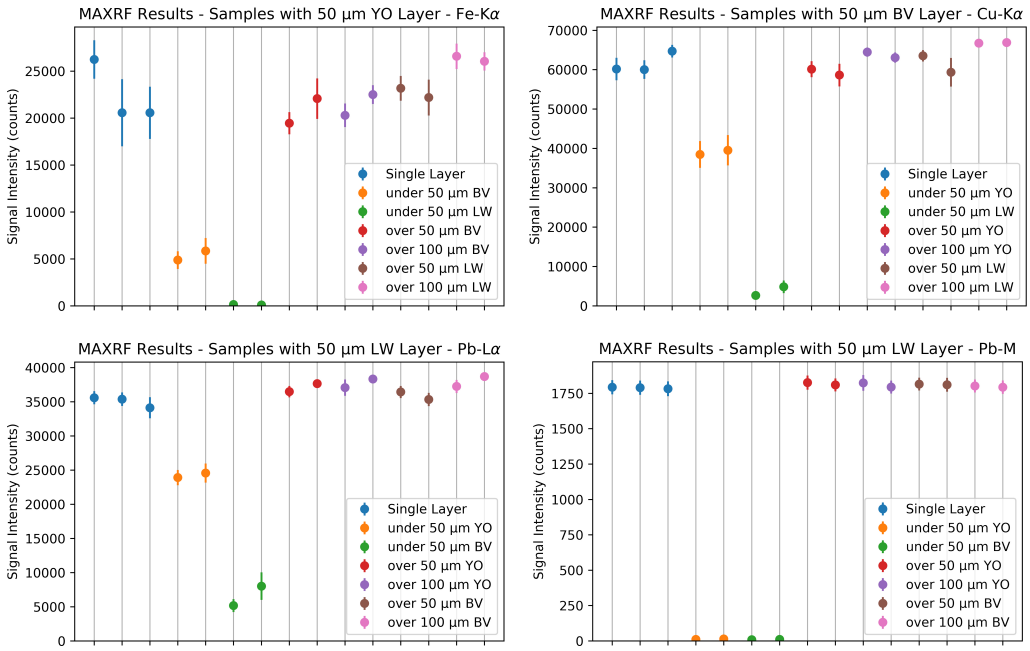

Figure 5.12: MA-XRF signal intensity for samples including 50 µm single-pigment layers.

Based on the issues previously noted with dead time, it is expected that the measurements from a single 50 µm layer would be different than those from a 50 µm overlying layer. However, if dead time were the only contributing factor, its effect would be expected to be a decrease in the signal intensity, as the overlying layer would emit a similar amount of photons, but the sensor would detect less of them due to the increased number of photons coming from the underlying layer. As can be seen in table 5.3, this is not quite the case. The average signal intensity of overlying layers is in some cases higher than that of single layers. It is believed that this effect is primarily due to a combination of two factors which have not been considered so far: reduction in layer thickness of paint layers during drying and secondary fluorescence.

Secondary fluorescence is the effect by which characteristic fluorescence is emited as a result of electrons being excited to higher energy states not by the radiation from the primary beam, but by the fluorescence radiation emitted by the atoms in the sample. For this to happen, the edge energy related to the fluorescence line being measured must be lower than the energy of the fluorescence radiation of another element in the sample (p.e. Fe-K fluorescence radiation can result from secondary excitation from Cu-K or Pb-L radiation, but not from Pb-M radiation). Given that the intensity of

fluorescence radiation is significantly lower than that of the primary beam, the effect of secondary fluorescence on the total signal intensity would be very low, but it is something which the model described in equation 5.15 does not account for. The effects of self-absorption and secondary fluorescence in the sample are jointly known as matrix effects, and are a common source of errors in quantitative XRF analysis.[80]

Reduction in layer thickness happens because, when oil paint dries, it

Table 5.3: Average signal intensities for samples including 50 µm single-pigment layers.

Fluorescence Line	Sample Layering	Average Signal Intensity (cps)
Fe-Kα	Single Layer	22456.040
	Over 50 µm BV	20761.574
	Over 100 µm BV	21399.473
	Over 50 µm LW	22677.082
	Over 100 µm LW	26306.800
	Under 50 µm BV	5366.441
	Under 50 µm LW	123.491
Cu-Kα	Single Layer	61640.970
	Over 50 µm BV	59385.875
	Over 100 µm BV	63773.023
	Over 50 µm LW	61441.900
	Over 100 µm LW	66817.730
	Under 50 µm BV	39010.830
	Under 50 µm LW	3736.820
Pb-Lα	Single Layer	35030.929
	Over 50 µm YO	37067.359
	Over 100 µm YO	37697.848
	Over 50 µm BV	35881.065
	Over 100 µm BV	37956.537
	Under 50 µm YO	24232.932
	Under 50 µm BV	6603.679
Pb-M	Single Layer	1788.405
	Over 50 µm YO	1817.866
	Over 100 µm YO	1808.883
	Over 50 µm BV	1813.048
	Over 100 µm BV	1797.864
	Under 50 µm YO	12.441
	Under 50 µm BV	9.640

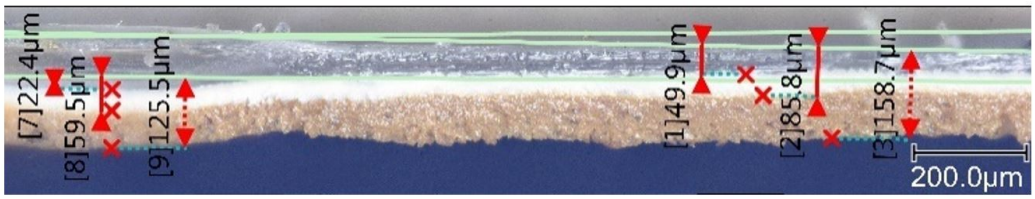

Figure 5.13: Cross-section view of a double layer sample including thickness measurements at two points.

experiences a reduction in volume and an increase in mass.[81] For the paint layer samples considered in this research, this leads to a reduction in the layer thickness. As far as XRF measurements are concerned, this shrinkage has little effect on the signal intensity, since the areal density of the pigments does not change. However, the shrinkage can have a significant effect during the sample preparation process for the double layer samples. Since it was necessary to wait for the underlying layers to dry before applying the overlying layers, the underlying layers would shrink. Given that the application thickness of the overlying layer was measured relative to the support rather than the top of the underlying layer, the actual thickness of the overlying layer would be directly dependent on the thickness of the dry underlying layer. Because of this, the actual thickness of the overlying layer might be higher than what was initially expected. It was originally planned to take cross sections of the different samples to determine the actual thickness of the constituent paint layers, but this was not possible due to the 2020 Covid-19 pandemic. A selection of 5 cross section samples were analyzed using a digital microscope as a trial right before the quarantine was put in place. An example of this analysis can be seen in figure 5.13 and the overall results can be seen in table 5.4. As can be seen, the results vary significantly, and the number of samples is far too limited to draw any strong conclusions. Existing research has found that linseed oil has a decrease in volume of around 8%, but which changed significantly between different types of oil,[81] and is very different from the measurements acquired during this research. Given that the oil ratio changes depending on the paint, the effect of shrinkage would be different for each paint. However, comparing the thickness measurements of a 100 µm single layer to a 100 µm overlying layer, it does seem to be that the overlying layer is thicker, implying that the shrinkage of the underlying layer did affect the final thickness of the overlying layer.

The unreliable layer thickness should have a much higher effect on the XRF signal intensity than secondary excitation, but without a comprehensive study of the paint layer thicknesses it is not possible to determine the exact

Table 5.4: Layer thickness measurements from optical microscopy.

Sample	Layer	Measurement (µm)	Average Shrinkage (%)
50 µm LW under 100 µm YO	LW	26.6	33.6
		37.1	
		35.9	
	YO	85.1	25.2
		66.0	
		73.2	
50 µm LW under 100 µm BV	LW	72.4	-24.3
		73.0	
		64.9	
		38.3	
	BV	104.6	-5.0
		132.0	
		129.8	
		53.5	
Mixture 5%BV, 95%YO	50 µm	30.0	44.7
		24.5	
		28.5	
	100 µm	68.5	45.5
		44.8	
		46.8	
		58.0	
	150 µm	113.4	22.5
		116.9	
		118.3	

magnitude of the two effects, which makes quantitative analysis impossible. However, a semi-quantitative determination of the stratigraphy could still be possible.

The first step in determining the stratigraphy would be to identify what elements are present in the surface of the samples. For some elements it is fairly simple to determine their presence on a paint surface as they have a low energy fluorescence line which is highly absorbed by any covering paint layer, like the M-lines for Pb and Hg. Setting a simple threshold already allows for identifying when the element is present on the surface. Figures 5.14 and 5.15 shows the results of this technique for identifying surface Pb in the mixture and layer samples. Several threshold values were tested but 50 counts was the highest one which would reliably identify the presence of

Pb, even the small amounts present in the small paint remains between the mixture samples.

For elements without such a fluorescence line it becomes slightly more difficult. Only setting a threshold would not work as a signal with low intensity could come either from a low amount of the element at the surface or from an underlying layer. A possible alternative would be to use the ratio between the signal intensities of two fluorescence lines of the same element to determine if a signal is being blocked by an overlying layer or not. The ratio between emitted intensities of fluorescence lines from a single element is a constant, but the measured intensity ratio depends on what lies between the sample and the detector. This phenomenon has already been used succesfully to account for the effect of a non-uniform overlying Pb layer on a Zn distribution map using the measured intensity ratio between the Zn-Kα and Zn-Kβ lines.[43] Using the deviation from the expected ratio to determine the effect of the overlying layer implies that the lack of a deviation could be used to determine the lack of an overlying layer. By mapping the deviation from the ratio, it is possible to determine the likelihood that the element is present at the surface.

This method would work for Fe and Cu, with their Kα and Kβ lines. It could also work with Pb using its Lα and Lβ lines, but given that it has already been proven to be possible to determine its surface presence using M-lines, it will not be considered. For Fe and Cu, the Kα/Kβ ratios are 7.443 and 7.472, respectively. For simplicity, both values are approximated to 7.5 for these calculations. For mapping, first a minimum signal threshold was applied to remove any pixels in which the signal was not intense enough to imply any presence of the element on the surface. Several values were tested based on the signal intensities from table 5.3. Ultimately, 100 counts was found to provide the most reliable results. Secondly, thresholds were applied to the line ratio limiting them to only values between 1 and 14, which eliminates unreasonable measurement values in case they were not removed by the signal threshold. Then the deviation of the line ratio from the expected value was scaled to half the range considered (6.5) and inverted using equation 5.17:

$$LR_{dev} = 1 - \frac{|LR - 7.5|}{6.5} \tag{5.17}$$

Where LR_{dev} is the scaled line ratio deviation and LR is the line ratio. Figures 5.14 and 5.15 show the results of this calculation for Fe and Cu in mixture and layer samples. For clarity, the normalized deviation results have

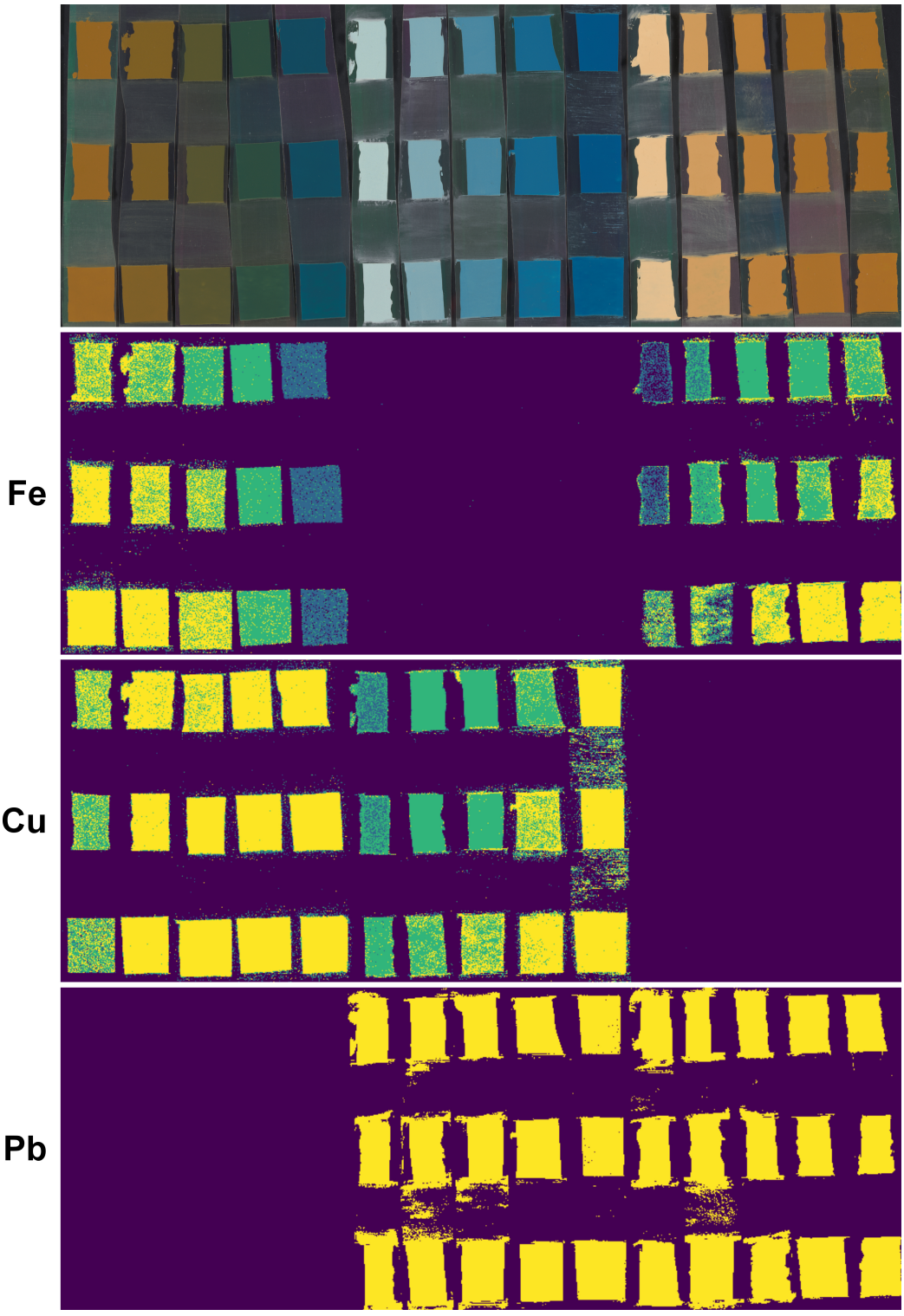

Figure 5.14: MA-XRF based surface maps of mixture samples. The brighter the area the more likely the respective elements presence at the surface.

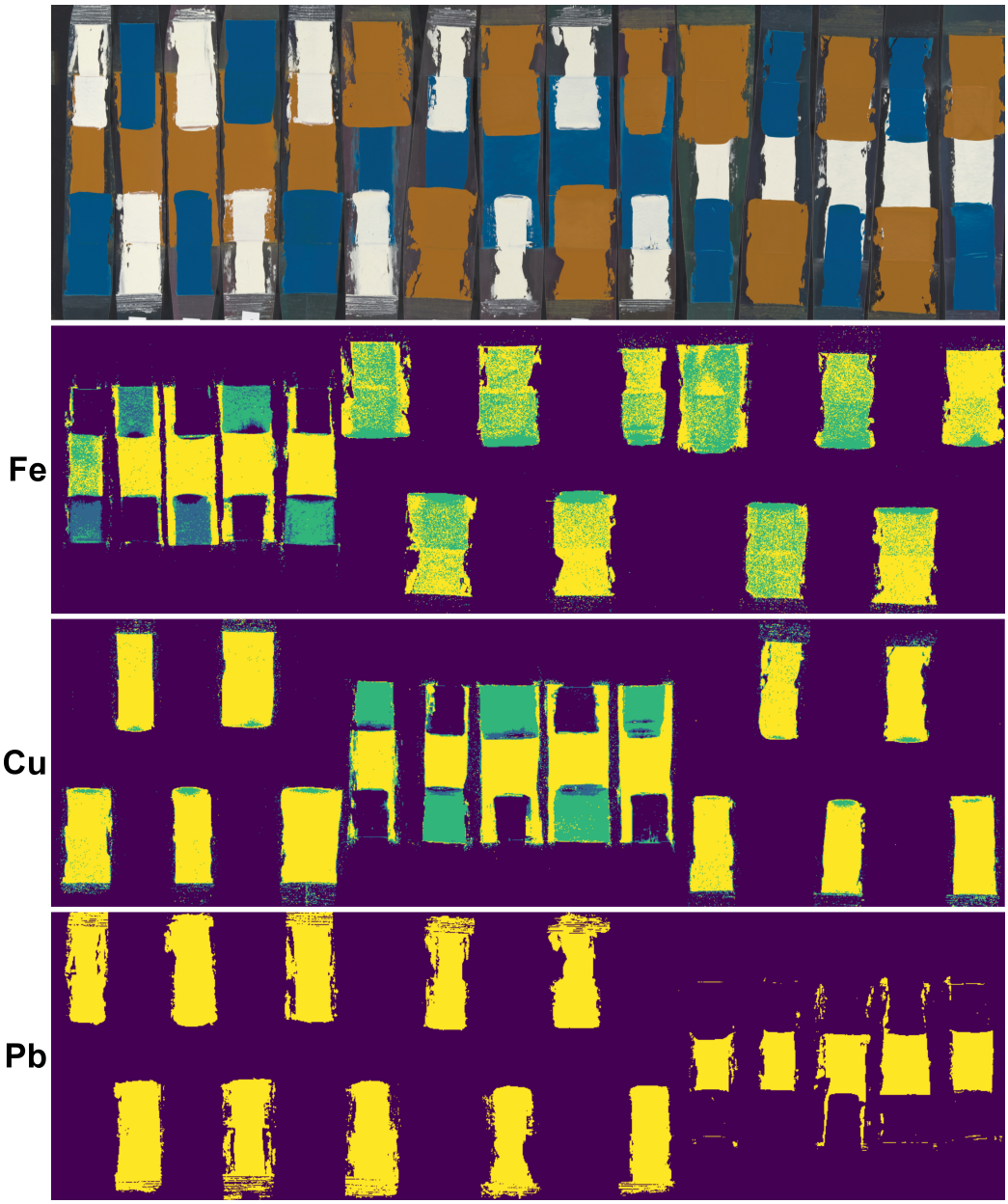

Figure 5.15: MA-XRF based surface maps of layer samples. The brighter the area the more likely the respective elements presence at the surface.

been grouped into ranges (0-0.5,0.5-0.7,0.7-0.9 and 0.9-1). It can be seen that this method works well at identifying surface presence of an element when the element is present in large amounts, but somewhat struggles with recognizing when the element is present at the surface only in low amounts or when it

is present in relatively thin layers. From figure 5.14 it is also possible to see that matrix effects have an effect on the accuracy of this method, as when Fe or Cu are mixed with the more strongly absorbing Pb, the accuracy decreases compared to when Fe and Cu are mixed together. When the element is in an underlying layer, the algorithm's ability to identify it as an underlying layer seems to depend on how absorbing the overlying layer is, with mixed success in the considered samples. However, all the areas in which a high likelihood of surface presence is found do match with areas in the sample where there is surface presence, so there are no false positives.

5.2 RIS - VNIR

The RIS data recorded in the VNIR range was initially handled using the more familiar methods, namely PCA and SAM, depending on the data set. The mixture samples were analyzed using PCA, the results of which can be seen in figure 5.16. It can be seen that it is possible to map most of the different paints correctly. However, it is shown that such a method struggles with LW in particular, as <20% LW when mixed in with either BV or YO does not result in individual clusters for the different mixtures. It is believed this is because LW has a lesser effect on the VNIR spectra than YO or BV. Given that VNIR reflection is strongly surface related, paint layer thickness does not affect the reflectance spectra and the samples are therefore clustered by the paint mixture. It is well known that it is possible to determine the ratio of the constituent pigments of a paint using the Kubelka-Munk theory of reflectance[57] if the constituent pigments are known. Rohani et al. recently applied an algorithm based on a neural network to perform non-linear unmixing of reflectance spectra, removing the requirement for previous knowledge of the constituent pigments.[62] Because of this previous success, quantitative compositional analysis based on VNIR was not attempted.

The same method was attempted with the layer samples, which, as can be seen in figure 5.17, resulted in clusters related to each surface paint. The cluster related to LW is significantly broader than the other two, which implies a greater variety in the spectra and led to the belief that it would be possible to differentiate between the single layer and double layer samples. However, there was no clear way of dividing the cluster to map the different areas. Because of this, a manual endmember selection and spectral angle mapping was attempted, the results of which can be seen in figure 5.18. It was found that it was somewhat possible to map double layer samples in which the overlying layer was LW. It is possible to see that the spectra for

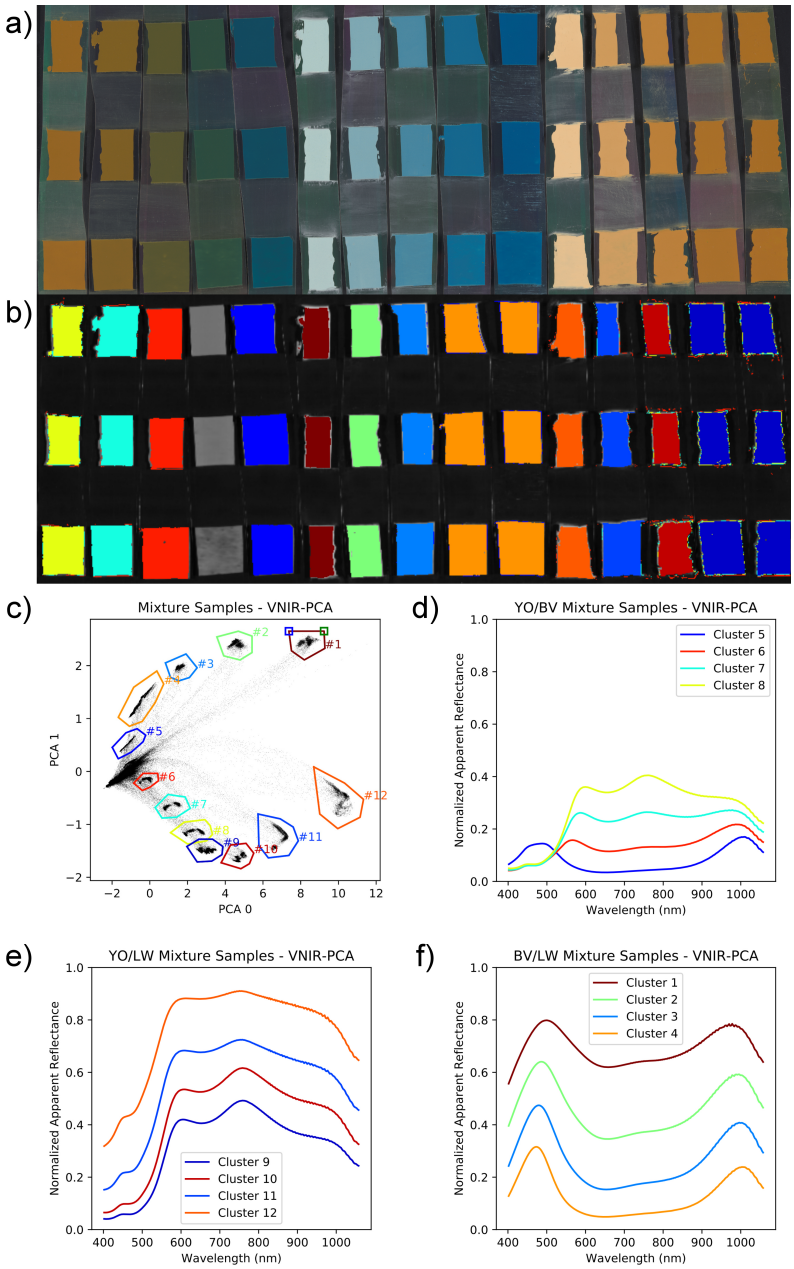

Figure 5.16: Results of the PCA analysis of the VNIR scan of the mixture samples **a)**Visible photograph **b)**Cluster maps **c)**PCA scatter plot from which clusters were defined. The missing column is clustered together with the background near the origin of the scatter plot **d)**Spectra of YO/BV clusters. Cluster 5 (C5) relates to 95% BV, 5% YO and later clusters increase YO amount **e)**Spectra of YO/LW clusters. C9 relates to 95% YO, 5% LW and later clusters increase LW amount **f)**Spectra of BV/LW clusters. C1 relates to 95% LW, 5% BV and later clusters increase BV amount.

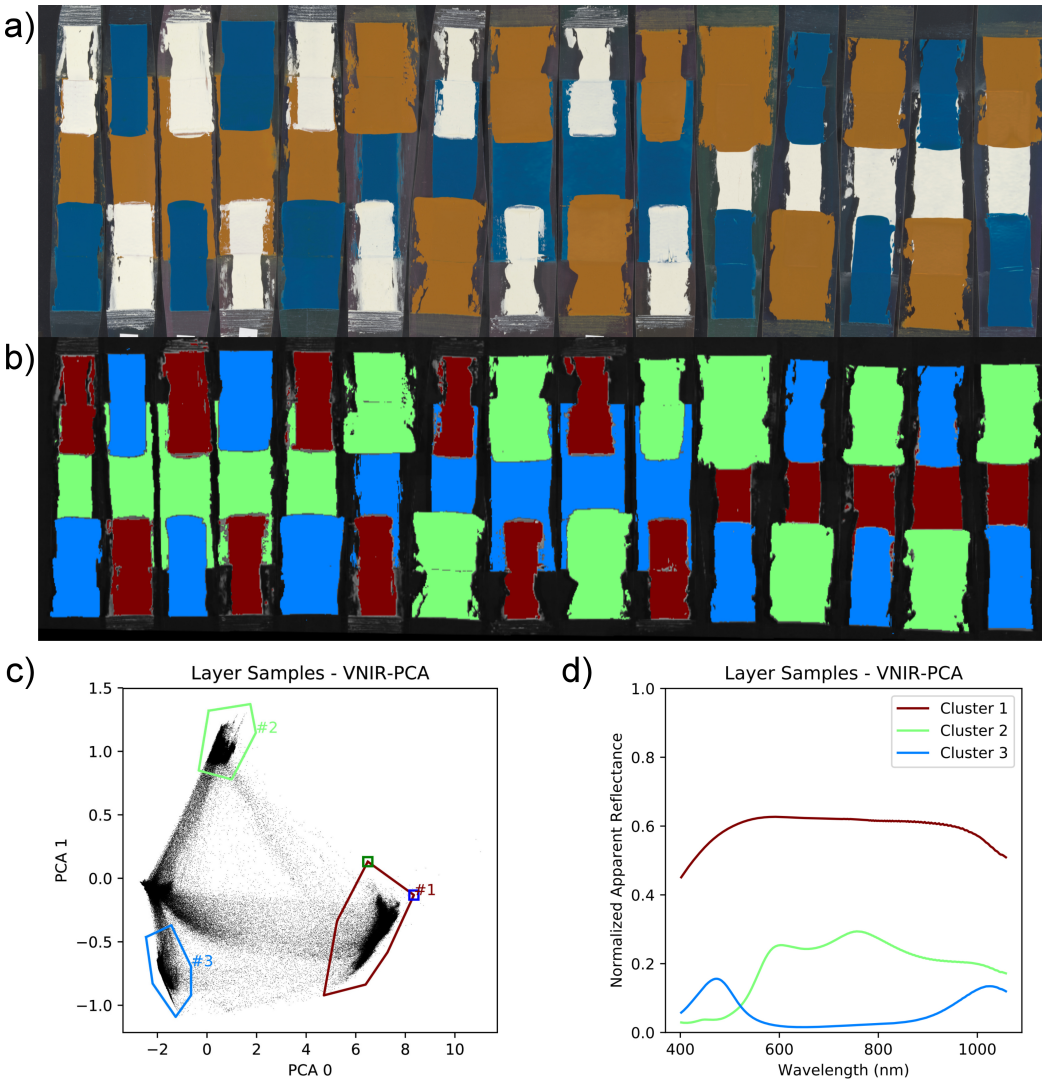

Figure 5.17: Results of the PCA analysis of the VNIR scan of the layer samples **a)**Visible photograph **b)**Cluster maps **c)**PCA scatter plot from which clusters were defined **d)**Spectra of the clusters. Each cluster relates to a pigment, C1 to LW, C2 to YO and C3 to BV.

these samples are very close to that of LW but also has minor reflectance features from the underlying layer as well, namely a maximum reflectance around 460 nm for the BV/LW samples and a minor peak around 750 nm for the YO/LW samples. However, the mapping of these samples has limited accuracy as the differences between the three spectra related to LW are very small and the manual selection of the spectra does not lead to the optimal

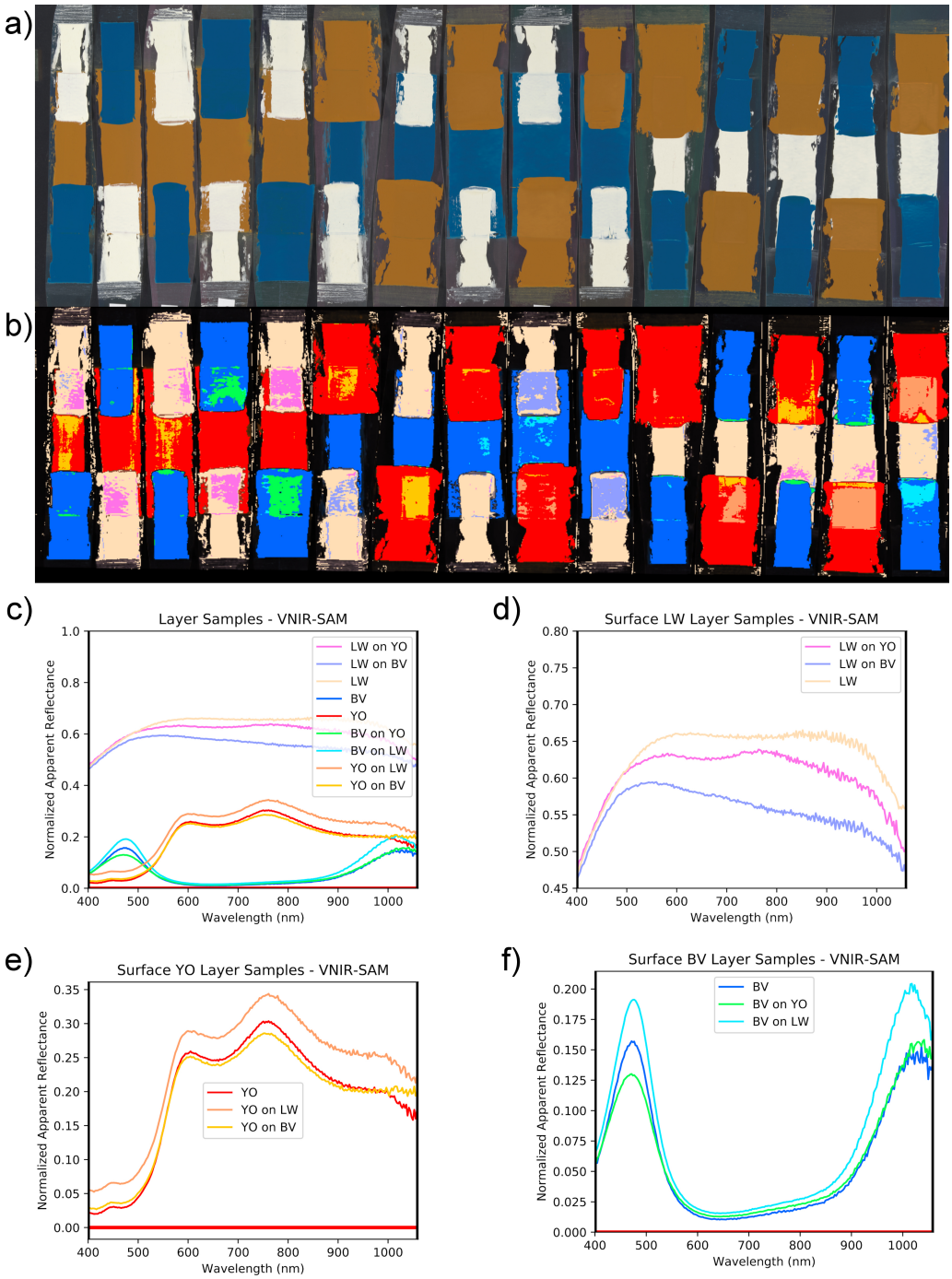

Figure 5.18: Results of the endmember analysis of the VNIR scan of the layer samples **a)**Visible photograph **b)**Spectral angle map **c)**The 9 manually selected spectral endmembers **d-f)**Detail view of the endmembers, divided by the surface layer. LW is the only pigment which shows identifiable features from underlying layers.

selection for the mapping. Attempting the same for samples with overlying BV or YO layers provided similarly mixed results, but the resulting spectra lack any characteristic features which could be used to identify the underlying paint layer.

5.3 RIS - SWIR

For the RIS data recorded in the SWIR range, the mixture samples were analyzed using PCA, the results of which can be seen in figure 5.19. The scatter plot shows small clusters grouped into larger streaks. The streaks relate to the different paint mixtures and the clusters relate to individual samples. In some cases, the thicker samples of a single paint mixture cluster together. The YO/BV mixtures are clustered too close together to accurately separate them, but it is still possible to recognize the same streaks that are formed for the other samples. The spectra shown in figure 5.19.d-f show the effect of paint composition and layer thickness for selected samples.

For the study of the layer samples, it is important to consider that SWIR has a greater penetration depth than VNIR and therefore has greater potential to provide more information about layer stratigraphy. However, this also means that the background could have a greater effect on the reflectance signal. Both the background and the binder present absorption features in the spectral region from 1500 to 2500 nm which overlap with the combination bands of the present pigments. Thus it was decided to focus on the spectral range between 1333 and 1584 nm, where the three considered pigments present OH stretching overtone features, whilst the linseed oil and background have limited contribution.[60] The same procedure using PCA was used and the results are detailed in figure 5.20. The resulting scatter plot did not present as clear clustering as the mixture samples, but still some clusters could be defined. The clusters were mostly related to different layering configurations, but they were not completely reliable and could not be used to accurately map different layer thicknesses.

It was hoped the depth of the features would provide information as to the areal density of the pigment. For the analysis, the spectra were cut to the desired spectral range and normalized to the highest value of the data set. In order to determine the depth of the features, several methods were tested.

First, a numerical integration for each feature was attempted. A specific channel range was defined for each feature and a simple trapezoidal inte-

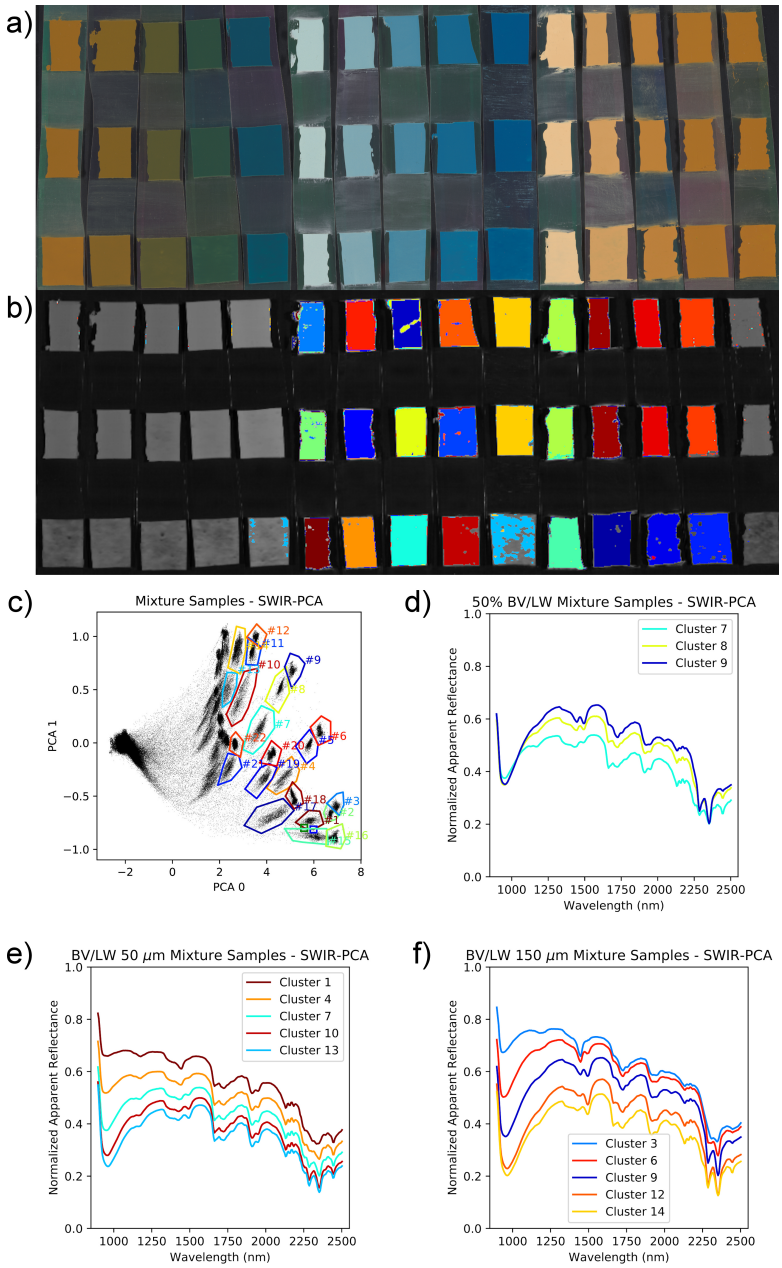

Figure 5.19: Results of the PCA analysis of the SWIR scan of the mixture samples **a)**Visible photograph **b)**Cluster maps **c)**PCA scatter plot from which clusters were defined **d)**Spectra of clusters related to the three 50% BV/LW samples. C7 relates to 50 µm and later clusters increase the layer thickness **e)**Spectra of clusters related to 50 µm samples of BV/LW mixtures. C1 relates to 95% LW, 5% BV and later clusters increase BV amount. **f)**Spectra of clusters related to 150 µm samples of BV/LW mixtures. C3 relates to 95% LW, 5% BV and later clusters increase BV amount.

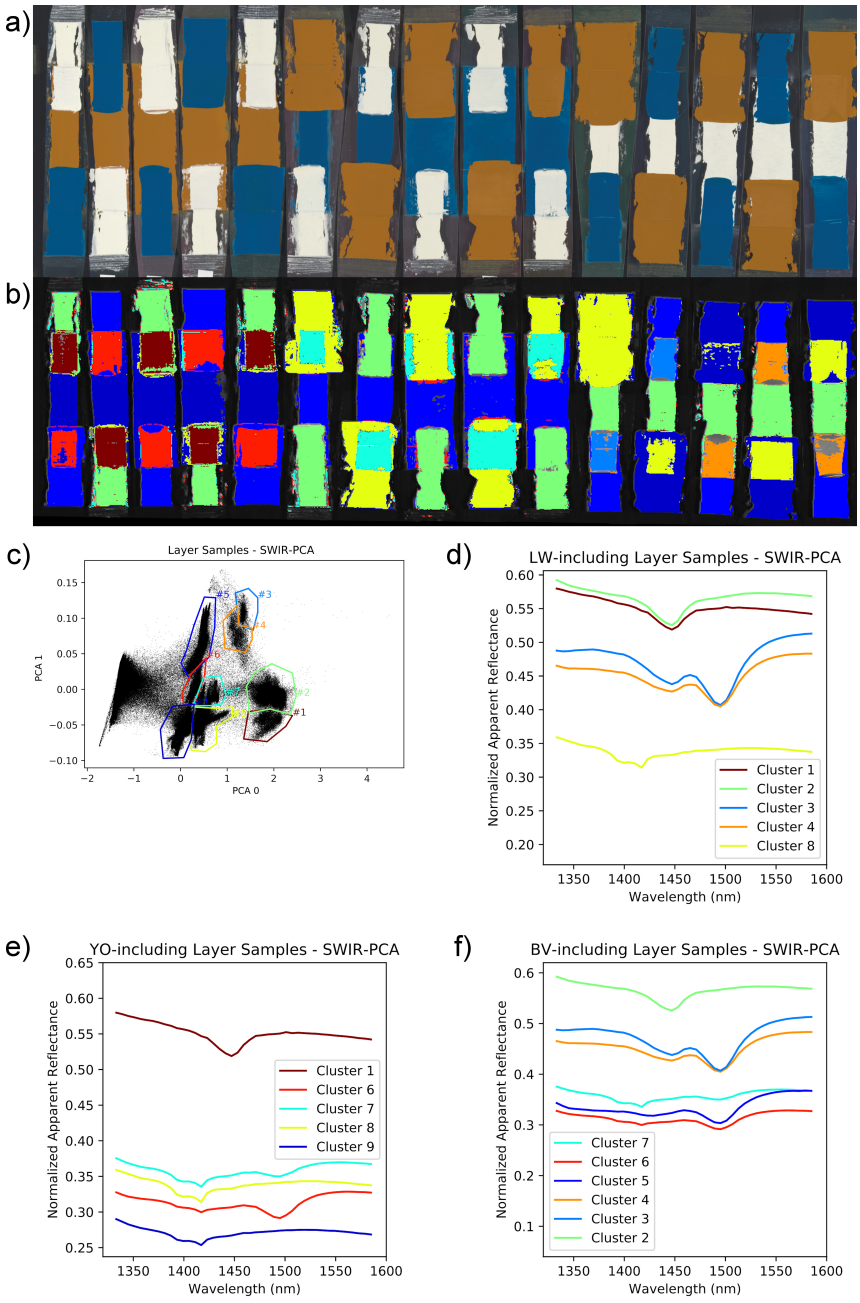

Figure 5.20: Results of the PCA analysis of the SWIR scan of the layer samples on the range 1333 and 1584 nm **a)**Visible photograph **b)**Cluster maps **c)**PCA scatter plot from which clusters were defined. A full legend for the spectra is committed as clusters were not well defined and did not always relate to a specific layer configuration **d)**Spectra of clusters related to LW-including samples. **e)**Spectra of clusters related to YO-including samples **f)**Spectra of clusters related BV-including samples.

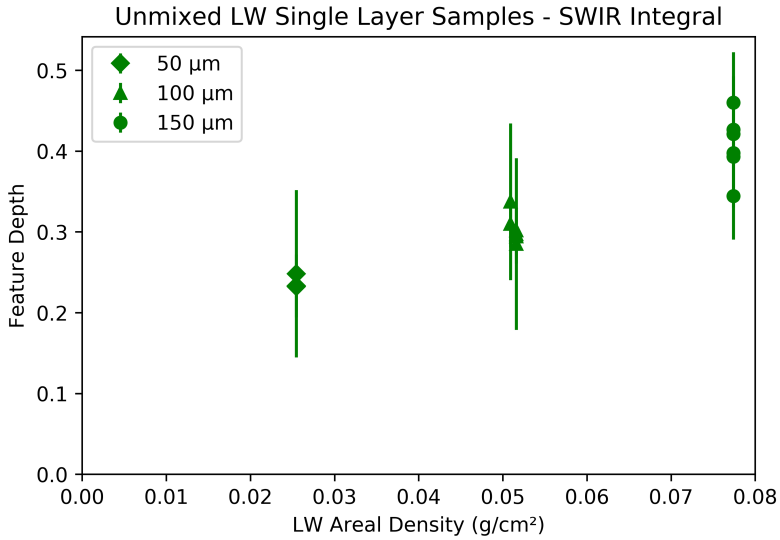

Figure 5.21: Results of the integral analysis of the SWIR data of single-layer LW samples.

gration was conducted. The integration ranges were: 1381-1447 nm for YO, 1405-1489 nm for LW and 1471-1519 nm for BV. This method did not present any reliable results, but some aspects, like Pb in single-layer samples, showed roughly the expected behavior, as seen in figure 5.21, with increasing feature depth for increasing areal density. The limited effectiveness of this method is believed to be related to the defined integration ranges. The integration ranges were defined to include the entire width of the features, which meant some were were slightly overlapping. However, the procedure would not distinguish between the contribution of the different features within the overlap areas and therefore any samples which included pigments with overlapping features would have inherently inaccurate results.

The next attempt was based on Non-negative least square (NNLS) fitting. A sample spectrum which would be used for the fitting was taken for each of the pigments from the acquired data set. The 150 µm single-layer single-pigment samples were expected to have the clearest representation of the reflectance features and were therefore selected as the fitting spectra. The fitting spectra can be seen in figure 5.22. The NNLS fitting was done using the Batch generator function of datahandlerp. The results of this showed a better correlation with the areal density, as can be seen in figure 5.23. The areal density of BV and LW in the mixture samples seems to have a roughly linear relation with the feature depth, whilst the depth of the feature for YO

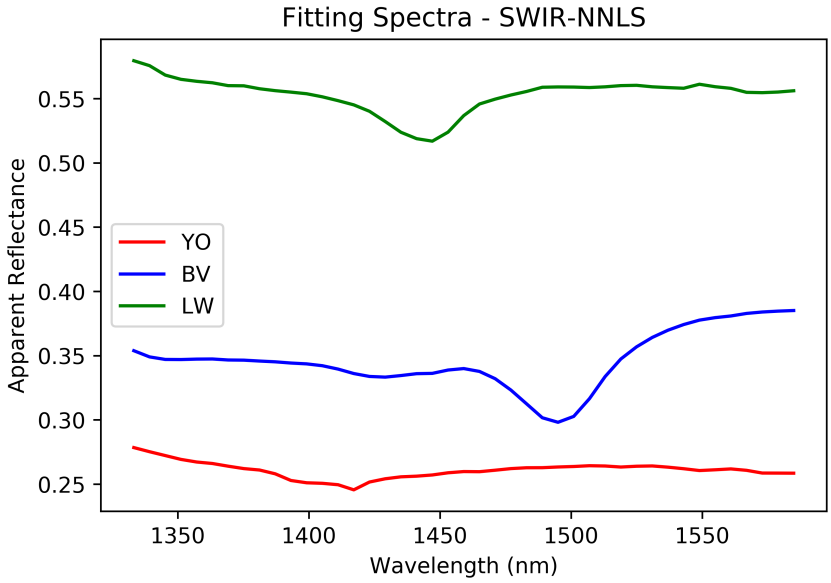

Figure 5.22: Fitting spectra for the NNLS analysis.

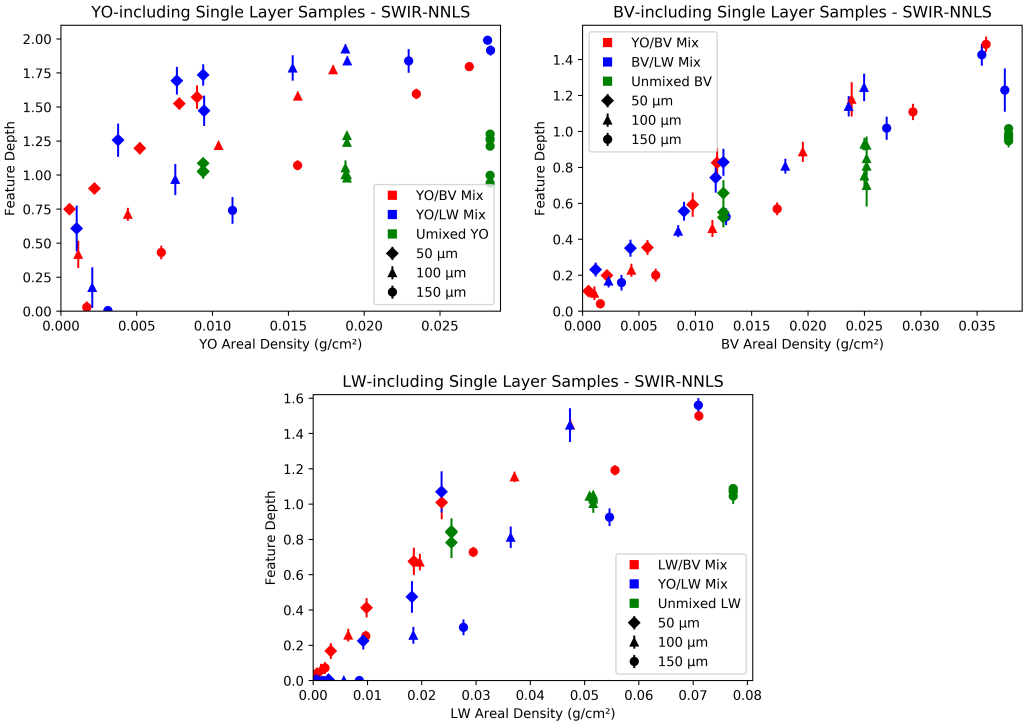

Figure 5.23: Results of the NNLS analysis of the SWIR data and their relation to pigment areal density.

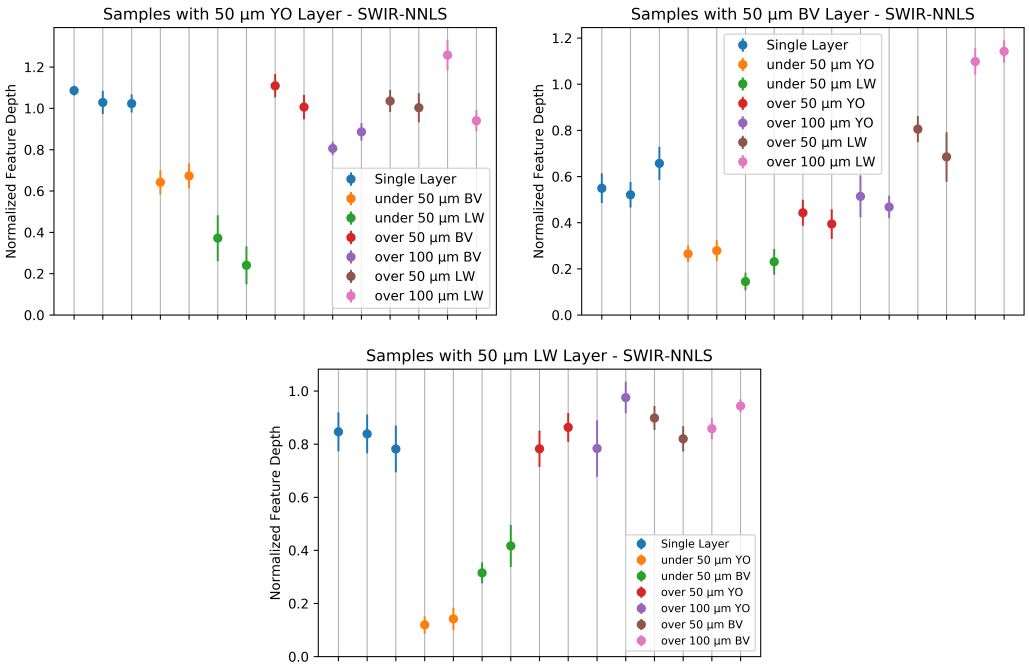

Figure 5.24: Results of the NNLS analysis of the SWIR data for samples including 50 µm single pigment layers.

seems to be proportional to the areal density but not linearly so. To verify this, the depth of the reflectance feature was normalized against the 95% sample in the same way as was done with the XRF signal intensity, the results of which are detailed in table 5.5. The calculated pigment concentrations for the 150 µm samples fell within 7% for the YO in YO/BV mix and 5% for the LW in LW/BV but was not particularly accurate for the other cases.

For single-layer single-pigment samples, the areal density of BV and LW in the mixture samples seem to be proportional to the feature depth, similarly to the mixture samples, but for YO these two factors do not seem to have any significant relation.

To study the effect of layering, figure 5.24 shows the feature depth for all samples including 50 µm layers of each corresponding paint. Underlying layers have a lowered feature depth, but overlying layers have mixed results, with some pigment combinations increasing feature depth (like BV in BV over LW) whilst others decrease it (like YO in YO over BV). Based on a manual analysis of the average spectra of the samples, these patterns do not quite match the real behavior. Whilst the BV feature depth is intensified by the presence of an underlying LW layer, the YO feature also becomes

Table 5.5: Quantification results of SWIR NNLS analysis.

Pigment	Mixture	Theoretical Composition (%)	Calculated Composition (%)	Error (%)
YO	YO/LW	95	95.00	0.00
		80	98.72	18.72
		50	91.18	41.18
		20	36.72	16.72
		05	00.00	5.00
	YO/BV	95	95.00	0.00
		80	84.43	4.43
		50	56.67	6.67
		20	22.83	2.83
		05	01.54	3.46
BV	BV/LW	95	95.00	0.00
		80	110.19	30.19
		50	78.65	28.65
		20	40.59	20.59
		05	12.26	7.26
	YO/BV	95	95.00	0.00
		80	70.92	9.08
		50	36.43	13.57
		20	12.81	7.19
		05	02.65	2.35
LW	YO/LW	95	95.00	0.00
		80	56.35	23.65
		50	18.34	31.66
		20	00.00	20.00
		05	00.00	5.00
	BV/LW	95	95.00	0.00
		80	75.49	4.51
		50	46.13	3.87
		20	16.00	4.00
		05	04.54	0.46

slightly deeper with an underlying BV layer. However, the average spectra vary somewhat between different samples of the same configuration, and the pixel spectra vary rather significantly within each sample, thus it is avoided to draw a conclusion as to how accurate these patterns actually are.

The next attempt was based on Non-negative matrix factorization (NMF), a method which has been used successfully for XRF analysis.[82] Unlike NNLS, NMF does not require the selection of fitting spectra but instead generates a feature matrix during the analysis. Another difference in this attempt was that instead of using the usual reflectance spectra, the spectra was mirrored vertically, such that the reflectance features were peaks rather than valleys. However, the term "depth" is still used to describe what would now technically be the hight of the features, for consistency. The NMF was conducted using the Batch generator function of datahandlerp with the settings detailed in table 5.6. Since the mixture samples and layer samples data sets were handled separately, the generated feature matrices were different for each data set. The features for each dataset are shown in figure 5.25.a. It is possible to see the resulting features are fairly different for the two data sets, but in both sets a single feature can be found that relates to each pigment, one feature relates to the background and the remaining one seems to be some combination, either constructive or destructive, of the other features. Because of the different feature matrices, the results of the two data sets are not comparable to each other and must be considered separately.

The results obtained were similar to previous ones, with some samples and pigments having better results as can be seen in figure 5.25.b. The areal

Table 5.6: Settings for the SWIR NMF analysis.

Setting	Value
N_components	5
init	nndsvd
solver	cd
beta_loss	frobenius
tol	0.0010
max_iter	2000
random_state	0
alpha	0.00
l1_ratio	0.00
verbose	Yes
shuffle	No

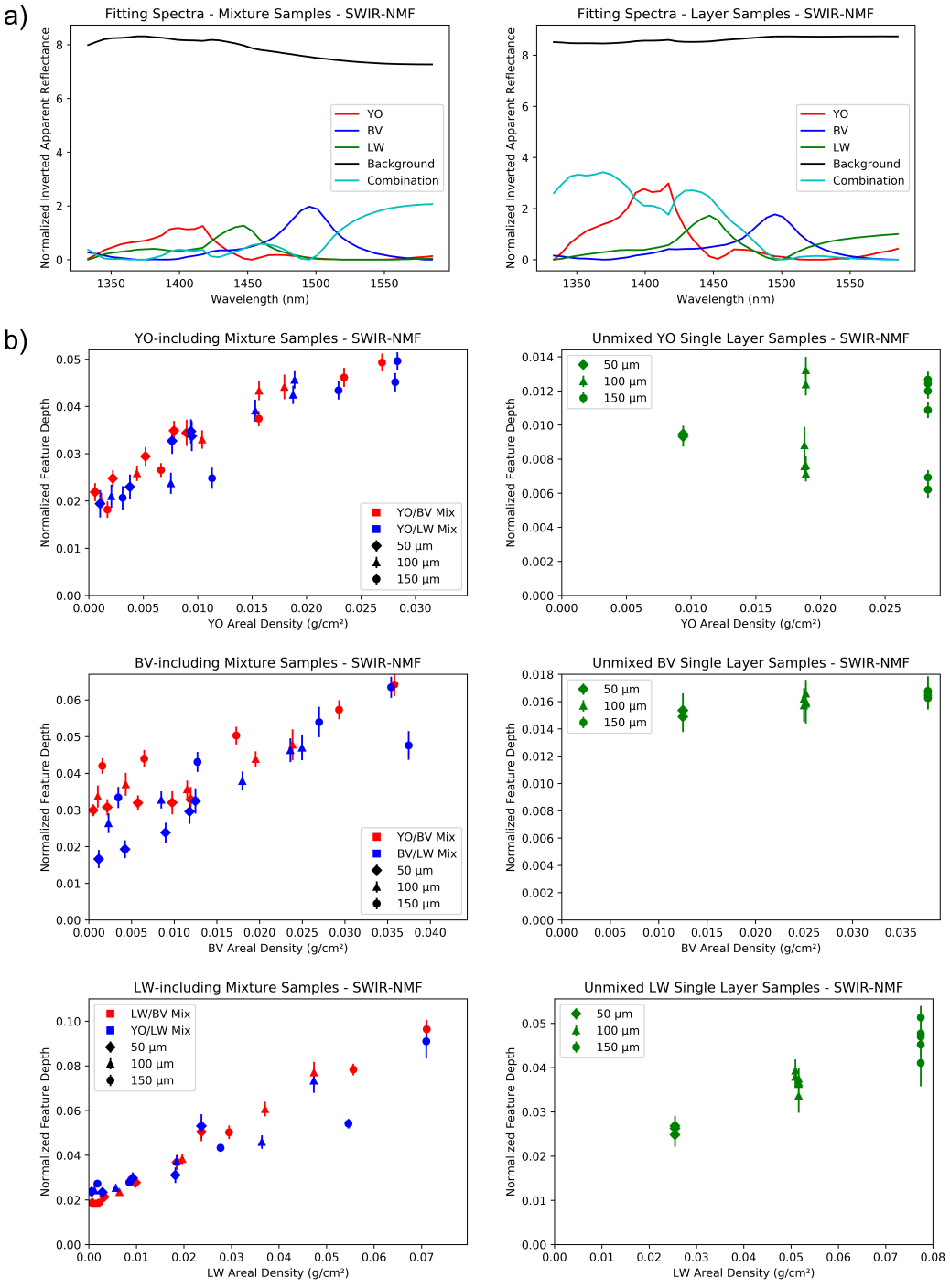

Figure 5.25: **a)**NMF fitting spectra for the two data sets **b)**Results of the NMF analysis of the SWIR data and their relation to pigment areal density.

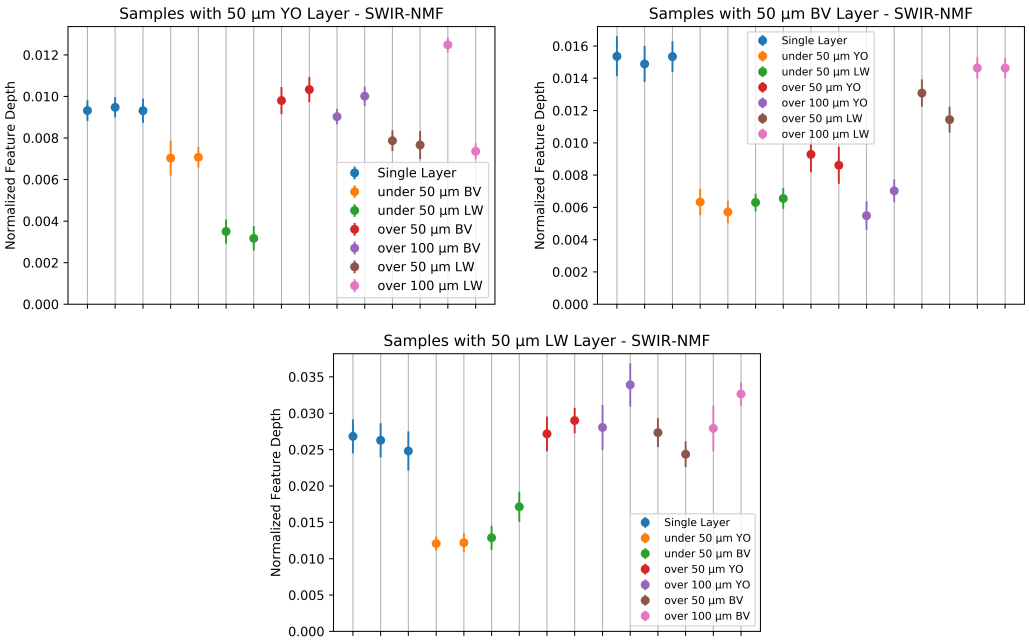

Figure 5.26: Results of the NMF analysis of the SWIR data for samples including 50 µm single pigment layers.

density of YO and LW in the mixture samples had a clearer correlation to the feature depth than those achieved using NNLS, but BV had worse. YO single-layer samples have a greater spread in their results, but BV and LW single-layer samples show a very strong correlation. It is believed the better correlation of the results has to do with the use of a "background" feature, which NNLS did not use. For comparison, the same quantification method used with the NNLS results was done with these results, having the depth of the reflectance feature normalized against the 95% sample, but the results are less accurate, as can be seen in table 5.7. The decrease in accuracy is believed to be due to the extra "combination" feature affecting the relation between the other features.

To observe if similar patterns arise regarding the effect of layering, the same was done as was done earlier for the NNLS results, comparing the results of all samples which included a 50 µm layer of the corresponding paint. The result of this can be seen in figure 5.26. Again, underlying layers have a lower feature depth and overlying layers do not have any consistent pattern, and those identified in the NNLS analysis are no longer present.

To attempt to improve the results, another NMF analysis was conducted

Table 5.7: Quantification results of SWIR NMF analysis.

Pigment	Mixture	Theoretical Composition (%)	Calculated Composition (%)	Error (%)
YO	YO/LW	95	95.00	0.00
		80	86.46	6.46
		50	83.10	33.10
		20	47.55	27.55
		05	39.59	34.59
	YO/BV	95	95.00	0.00
		80	88.92	8.92
		50	72.09	22.09
		20	51.16	31.16
		05	34.99	29.99
BV	BV/LW	95	95.00	0.00
		80	126.66	46.66
		50	107.72	57.72
		20	86.04	66.04
		05	66.64	61.64
	YO/BV	95	95.00	0.00
		80	84.84	4.84
		50	74.41	24.41
		20	65.06	45.06
		05	62.17	57.17
LW	YO/LW	95	95.00	0.00
		80	56.51	23.49
		50	45.23	4.77
		20	29.12	9.12
		05	28.49	23.49
	BV/LW	95	95.00	0.00
		80	77.24	2.76
		50	49.56	0.44
		20	27.19	7.19
		05	18.58	13.58

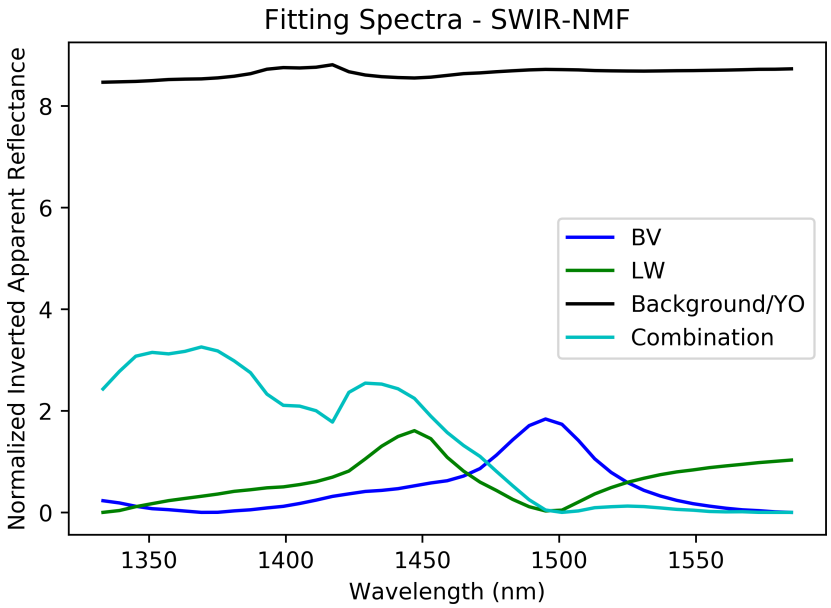

Figure 5.27: Feature matrix for a 4 component NMF analysis of the layer samples.

using 4 components instead of 5, hoping that this would remove the combination feature. However, this was not the case, as can be seen in figure 5.27. Instead of removing the combination feature, it kept it and somewhat combined the YO feature with the background feature.

Based on the improved results of the NMF, it was decided to attempt the NNLS a second time, but this time using the modified spectra used in the NMF trial rather than the reflectance spectra and a different selection procedure for the fitting spectra. Instead of having only three fitting spectra, one for each pigment, four spectra were used as to also include a possible background contribution. The selected fitting spectra can be seen in figure 5.28. The background contribution was taken as a constant across the considered bands for simplicity. The pigment spectra were normalized as to remove the differences in base reflectance which were very noticeable in the previous NNLS attempt, but which should now be accounted for by the background spectra.

The results of the procedure are visible in figure 5.29. The relation between feature depth and areal density is slightly improved for mixture and single-layer samples, except for unmixed YO single-layer samples which continue to lack any strong relation. The same quantification method was again

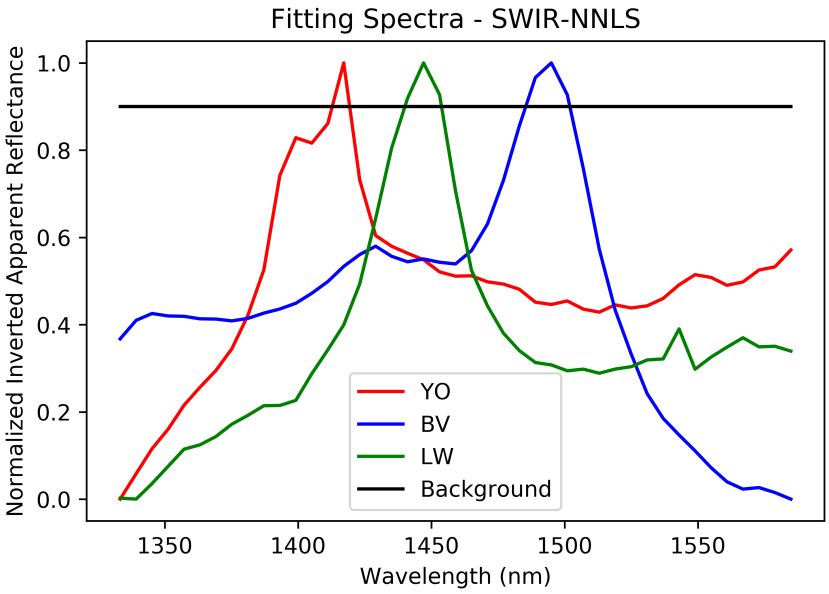

Figure 5.28: Fitting spectra for the second NNLS analysis.

attempted with these results, but the calculated values are less accurate than those achieved in the first NNLS attempt, as can be seen in table 5.8. The results from the double-layer samples, which can be seen in figure 5.30, did not exhibit a significant change in the pattern previously observed.

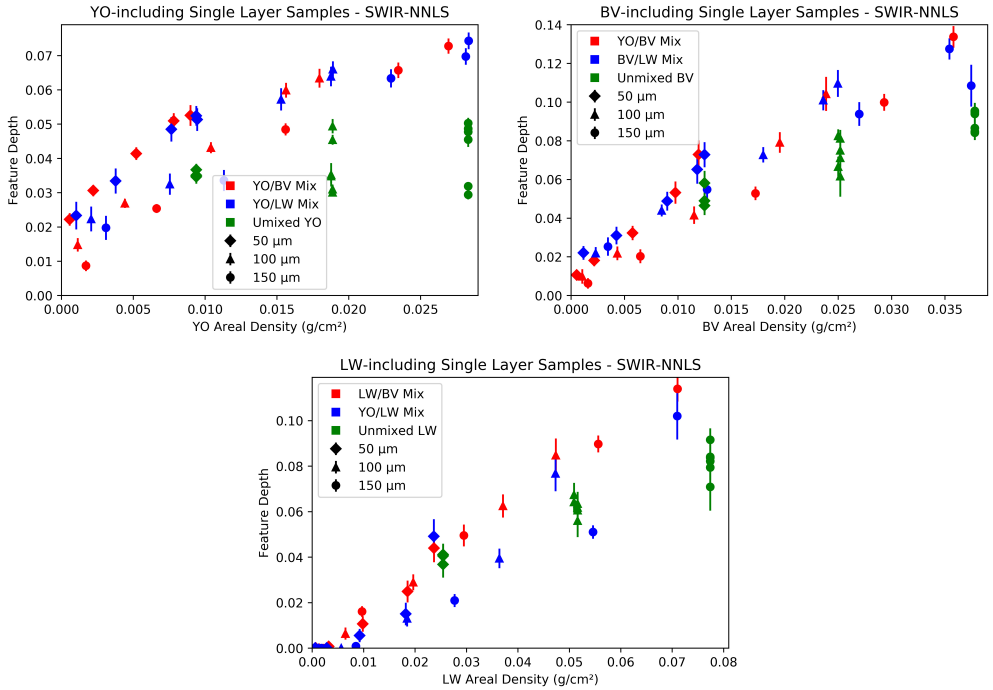

Figure 5.29: Results of the second NNLS analysis of the SWIR data and their relation to pigment areal density.

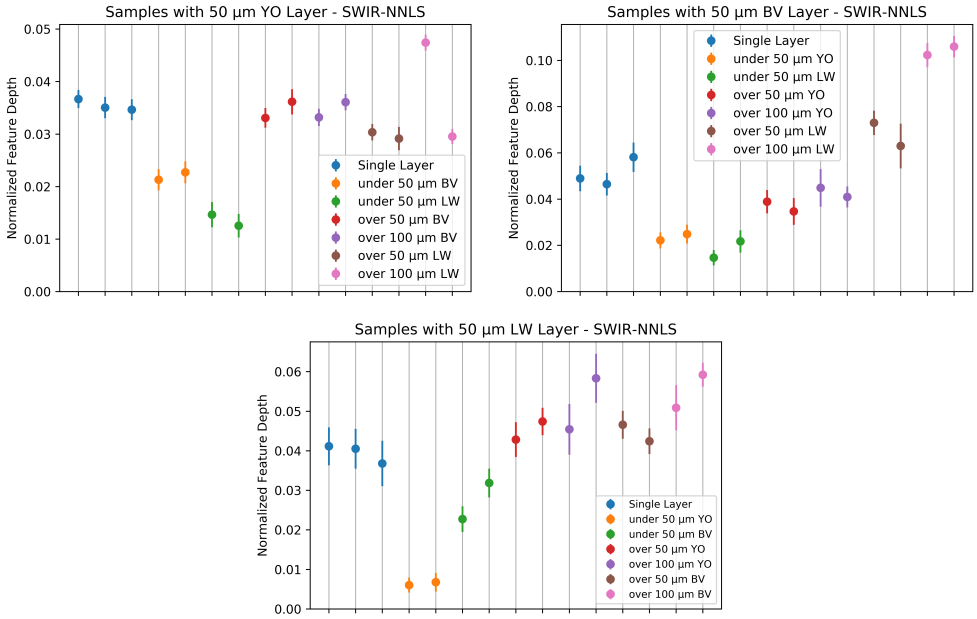

Figure 5.30: Results of the second NNLS analysis of the SWIR data for samples including 50 µm single pigment layers.

Table 5.8: Quantification results of the second SWIR NNLS analysis.

Pigment	Mixture	Theoretical Composition (%)	Calculated Composition (%)	Error (%)
YO	YO/LW	95	95.00	0.00
		80	89.18	9.18
		50	81.03	31.03
		20	42.92	22.92
		05	25.25	20.25
	YO/BV	95	95.00	0.00
		80	85.79	5.79
		50	63.26	13.26
		20	33.14	13.14
		05	11.32	6.32
BV	BV/LW	95	95.00	0.00
		80	111.62	31.62
		50	82.17	32.17
		20	47.95	27.95
		05	22.14	17.14
	YO/BV	95	95.00	0.00
		80	70.95	9.05
		50	37.52	12.48
		20	14.41	5.59
		05	04.47	0.53
LW	YO/LW	95	95.00	0.00
		80	47.52	32.48
		50	19.50	30.50
		20	00.82	19.18
		05	00.00	5.00
	BV/LW	95	95.00	0.00
		80	74.81	5.19
		50	41.30	8.70
		20	13.42	6.58
		05	00.00	5.00

Chapter 6

Discussion

This research aimed to provide quantitative data regarding two factors of paint layers: paint composition and paint stratigraphy. These two factors are inherently tied and affect one another, but for the sake of simplicity, they will first be considered separately for the evaluation of the efficacy of the tested quantification methods.

6.1 Paint Composition

The methods tested for quantifying paint composition had mixed results. Both the methods through RIS and through MA-XRF had some successes but were not completely reliable.

It is well known that a single XRF measurement can deliver concentration information of analyzed samples.[80,83] The results acquired in this research seem to imply that a collection of XRF measurements conducted under the same circumstances can provide relative concentration information as well. It is believed that the lack of information regarding the radiation source significantly hindered the quantification methods based on XRF measurements attempted in this research and that accurate quantitative analysis of paint composition is unlikely to be successful without it. However, it is clear that there are other factors, like dead time, which further complicate the quantification due to their uneven effect across the measured samples.

VNIR-RIS, particularly in the visible range (400-750 nm), has long been proven to be able to provide information on the composition of surface paint layers. However, without any previous information on pigments present, quantitative analysis based spectral unmixing is considered too computationally intensive for practical use.[62] AI-driven methods have proven successful

at addressing these issues. However, these methods have thus far only been used for identifying pigments present in considerable amounts but have not been tested for pigments present in small amounts (<10%).

SWIR-RIS, being a much more recent addition to the painting's analysis toolbox, still requires a lot more work on the data analysis procedures before it can be practically useful in quantitative analysis. Even though this technique suffers from the same setbacks as its VNIR counterpart, requiring previous information on pigments present, the tests prove that it is possible to gather some quantitative information from the acquired spectra. However, the tested quantification methods require the analyzed pigments to have specific reflectance features, which somewhat limits their applicability. The effect of the binder could also further limit the applicability of these methods, as its reflectance features could overlap those of the present pigments.

Given the specific strengths of each technique, it is strongly believed that a mixed MA-XRF/RIS approach would provide more accurate quantitative data, as XRF results could be used to verify the results from quantitative RIS analysis or vice versa.

6.2 Paint Stratigraphy

A full quantitative determination of paint layer stratigraphy was not possible with the tested methods, but it was possible to distinguish between surface and subsurface paint layers using XRF and VNIR-RIS but not SWIR-RIS.

In most cases, XRF measurements will not allow distinguishing between an element being present in large amounts in a subsurface layer or in small amounts in a surface layer from the intensity of a single fluorescence line. There are some elements, like Pb and Hg, which have very surface specific fluorescence lines, that allow for identifying their presence in a surface layer. For elements that do not have these kinds of fluorescence lines, using the relative intensity of different lines from that element in combination with the absolute intensity of the lines, it becomes possible to determine the likelihood of that element being present at the surface. If knowledge of the paint composition is available, a description of the paint layer thickness is also possible.

VNIR-RIS is the most reliable method for identifying surface layers, but it does not provide any further information. However, if the pigments on

the surface layer are not strongly blocking, like LW, some features from underlying layers might be slightly visible in the spectra, obfuscating the results.

SWIR-RIS proved useful to distinguish areas with different paint layer stratigraphy, but the results acquired were not entirely accurate and it was not possible to gather further quantitative information on the stratigraphy using the tested methods. The greater penetration depth of the method makes it suffer from a similar issues as MA-XRF, as it is difficult to distinguish if a feature is coming from a pigment being present in large amounts in a subsurface layer or in small amounts in a surface layer. A comparison of magnitudes of different features of the same pigment, similar to what is proposed for MA-XRF, would be extremely complicated for RIS analysis and is not currently considered a practical solution. However, if the VNIR and SWIR spectra are combined and analysed as a unit, it should be possible to distinguish surface layer contributions from that of subsurface layers.

In combination, the results of RIS and MA-XRF can be used to differentiate between pigments present in the surface and pigments present in subsurface layers. None of the tested methods provide information as for further quantification of the paint layer stratigraphy.

6.3 Overall

Based on the results achieved, it is believed that a combined MA-XRF/RIS approach would be a useful tool for paint layer stratigraphy and composition analysis. VNIR-RIS allows for pigment identification and composition analysis on surface layers. Having this information, if subsurface pigments are distinct enough from those in the surface layer, MA-XRF or SWIR-RIS could be used for determination of the surface layer thickness. If there is only one subsurface layer to analyze, MA-XRF could be used for quantification of its paint composition and thickness.

If there is more than one subsurface layer or a single subsurface layer with elemental or molecular overlap with the surface layer, differentiating between them becomes more difficult. Comparing signal intensity for different fluorescence lines of the same element, similarly to what is proposed for surface pigment identification with MA-XRF, could be useful for distinguishing subsurface layers. However, this would only work if an accurate description of the surface layer and its mass absorption coefficient is possible.

Given that most of the challenges identified during the research come from a lack of context for the data, it is believed that integrating into the process any other paint layer stratigraphy and composition data would greatly increase the accuracy of the results. Data from cross section samples or from depth discriminating methods like CXRF or THz Imaging, would be particularly useful for this purpose. Setting this information as a prior to a specific pixel in the acquired data set and working outwards from that pixel would increase the chances of successfully identifying the composition and stratigraphy.

It is also important to note that the results acquired in this research represent a best-case scenario for both MA-XRF and RIS analysis, as the samples are based on three pigments which are easily differentiable with all three considered methods. For pigments which have overlaps in either their elemental profile or their absorption features, or for pigments which lack any characteristic absorbance feature in the measured range or element measurable by MA-XRF, analysis with these methods would be significantly more difficult.

Chapter 7

Conclusion

Regarding the primary goal of this research, the results acquired strongly support the effectiveness of a combined approach between MA-XRF and RIS for the semi-quantitative analysis of easel paintings. Each of the considered methods allows for varying kinds of analysis and quantification and complement each other well, within the context of the tested samples.

The samples created for this research provided significant insight into the challenges of each method as well as difficulties that must be considered when creating such samples. Paint layer shrinkage during drying, contribution of support material and pigment particle size distribution are all things that must be considered. Given that the samples could not be fully characterized using cross-section samples, the full accuracy of the quantitative results could not be confirmed. However, even though absolute results were not possible, the relative results still support the effectiveness of the methods.

MA-XRF again proved to be a very useful tool for elemental analysis of easel paintings. The signal intensity for the different fluorescence lines is considered the main avenue for acquiring quantitative results. Regarding paint layer stratigraphy, it was possible to determine the likelihood of a pigment being present at the surface using either the intensity of surface specific fluorescence lines or the ratio between two different fluorescence lines of the same element. Gathering further information on subsurface layers is possible but requires prior information. For single layer samples, it was possible to determine the relative concentration of a specific pigment by comparing it to a known sample of the same thickness. For paint layers of a known composition, determining the layer thickness is possible. If both the paint layer composition and thickness are unknown, determining either becomes more complicated, and it is believed in such situations a combined approach with RIS would prove greatly beneficial.

VNIR-RIS is different from the other methods in that the penetration depth is very low, particularly in the visible range. This makes it particularly useful for differentiating surface layer compounds. Previous research has proved it is possible to determine paint composition based on unmixing of visible spectra. The results achieved in this thesis show that it is possible to differentiate between different paint compositions via PCA. The results of that analysis showed that the paint layer thickness does not have a very significant effect on the signal. However, using SAM it was possible to see that in some cases, features from underlying layers could also have slight contributions to the measured spectra, which could affect the accuracy of a quantitative values of paint composition.

SWIR-RIS has already proven its usefulness for pigment identification, but the results acquired also show its potential for quantitative analysis. Thanks to its higher penetration depth, this method allowed distinguishing not only between different paint compositions, but also different paint layer thicknesses and stratigraphies, albeit with limited accuracy. Using NNLS and NMF provided some quantification avenues for paint composition and layer thickness for single-layer samples. The results of these methods also proved that paint layering does have an effect on the magnitude of the reflectance features which, if further researched, could provide an avenue for quantitative analysis.

Several challenges were identified during the research which make quantitative analysis with these methods difficult. Limited information regarding the radiation source used for the MA-XRF measurements and the model simplifications made because of it are considered the main obstacle which thwarted the attempted quantification methods. The uneven effect of sensor dead time during MA-XRF scanning was also identified as a possible obstacle, but this is expected to only have a limited effect when compared to the previously mentioned issues. The dependence of reflectance on pigment particle size distribution and packing density makes absolute quantitative analysis with RIS difficult, but the relative results could still be used to verify results based on MA-XRF readings. The greater penetration depths of SWIR-RIS and MA-XRF make it difficult to distinguish between different subsurface layers, but it is believed that providing more context from other sources, like cross-section sampling or selective analysis with depth-discriminating methods like CXRF, would help address this.

More research is required before any practical quantitative analysis algorithms become available. Further research is recommended to focus on

a broader selection of pigments and more complex sample compositions and stratigraphies. Given that so far most research into quantitative RIS analysis has focused on the VNIR range, it is recommended to focus future research on an extended range which includes both the VNIR and SWIR ranges or to conduct research specifically on the SWIR range.

The success of neural networks in quantification of VNIR-RIS results gives good reason to believe that applying similar methods to MA-XRF and SWIR-RIS would also prove successful. A very similar method to that used by Rohani et al.[62] for VNIR-RIS could be applied to MA-XRF, as a theoretical model describing the XRF signal is available. However, the lack of an accurate model for definition of SWIR reflectance means that the databases required for training such a network would have to be mostly based physical mock-ups, which would be very time consuming, but very likely worth the effort.

Expanding such efforts to include other machine learning and spectral imaging methods is also believed to be a very promising avenue for quantitative analysis of paint layer composition and stratigraphy. For example, the use of Bayesian Networks with RIS and XRF could provide a useful tool for pigment identification and probabilistic layer composition and stratigraphy determinations. THz imaging is considered to have the most potential for determination of paint stratigraphy and using it in combination with RIS and XRF has the potential to significantly increase the accuracy of paint layer composition and stratigraphy determinations.

Bibliography

(1) Gombrich, E., *The Story of Art - 16th Edition*; Phaidon Press: 1995.

(2) Kuniholm, P.; Taft, W.; Newman, R.; Mayer, J.; Stulik, D., *The Science of Paintings*; Springer New York: 2006.

(3) Equestrian Portrait of Frederick Henry, anonymous, in or after 1631 Rijksmuseum, `http://hdl.handle.net/10934/RM0001.COLLECT.12013` (accessed 07/29/2020).

(4) Brommelle, N. S. Art conservation and restoration - Paintings on ivory | Britannica Encyclopædia Britannica, Inc., `https://www.britannica.com/art/art-conservation-and-restoration/Paintings-on-ivory` (accessed 07/29/2020).

(5) Brommelle, N. S. Art conservation and restoration - Paintings | Britannica Encyclopædia Britannica, Inc., `https://www.britannica.com/art/art-conservation-and-restoration/Paintings` (accessed 07/29/2020).

(6) Alfeld, M.; Broekaert, J. *Spectrochimica Acta Part B Atomic Spectroscopy* **2013**, *88*, 211–230.

(7) Van Asperen de Boer, J. R. J. *Nederlands Kunsthistorisch Jaarboek (NKJ) / Netherlands Yearbook for History of Art* **1975**, *26*, 1–40.

(8) Alfeld, M.; de Viguerie, L. *Spectrochimica Acta Part B: Atomic Spectroscopy* **2017**, *136*, 81 –105.

(9) van Loon, A.; Vandivere, A.; Delaney, J.; Dooley, K.; De Meyer, S.; Vanmeert, F.; Gonzalez, V.; Janssens, K.; Leonhardt, E.; Haswell, R.; de Groot, S.; D'Imporzano, P.; Davies, G. *Heritage Science* **2019**, *7*, DOI: `10.1186/s40494-019-0344-0`.

(10) Delaney, J.; Dooley, K.; van Loon, A.; Vandivere, A. *Heritage Science* **2020**, *8*, 4.

(11) Johnson, D. H.; Richard Johnson, C.; Erdmann, R. G. *Signal Processing* **2013**, *93*, Image Processing for Digital Art Work, 527 –540.

(12) Cabal, A.; Pernía, D.; Schalm, O.; Van Espen, P. *Analytical and bioanalytical chemistry* **2011**, *402*, 1471–80.

(13) Fisher, S. L.; Holmes, D. J.; Jørgensen, J. S.; Gajjar, P; Behnsen, J; Lionheart, W. R. B.; Withers, P. J. *Measurement Science and Technology* **2019**, *30*, 035401.

(14) Dik, J.; Reischig, P.; Krug, K.; Wallert, A.; Coerdt, A.; Helfen, L.; Baumbach, T. *Journal of the American Institute for Conservation* **2009**, *48*, 185–197.

(15) BRIDGMAN, C. F.; KECK, S.; SHERWOOD, H. F. *Studies in Conservation* **1958**, *3*, 175–182.

(16) Bridgman, C. F.; Michaels, P.; Sherwood, H. F. *Studies in Conservation* **1965**, *10*, 1–7.

(17) Van Asperen de Boer, J. R. J. *Applied optics* **1968**, *7*, 1711–4.

(18) Rie, E. **1982**, *27*, 102–108.

(19) Ludwig, N.; Orsilli, J.; Bonizzoni, L.; Gargano, M. *Archaeological and Anthropological Sciences* **2019**, *11*, 6841–6850.

(20) Invernizzi, C.; Fichera, G.; Licchelli, M.; Malagodi, M. *Microchemical Journal* **2018**, *138*, 273–281.

(21) Van Grieken, R.; Markowicz, A. A, *Handbook of X-Ray Spectrometry, second edition*, 2002.

(22) Haschke, M. In *Laboratory micro X-ray Fluorescence - Instrumentation and Application*, 2014; Chapter 3: Special Requirements for l-XRF.

(23) Reiche, I.; Eveno, M.; Müller, K.; Calligaro, T.; Pichon, L.; Laval, E.; Mysak, E.; Mottin, B. *Applied Physics A* **2016**, *122*, 947.

(24) Van Loon, A.; Noble, P.; Krekeler, A.; Van der Snickt, G.; Janssens, K.; Abe, Y.; Nakai, I.; Dik, J. *Heritage Science* **2017**, *5*, 1.

(25) Nakai, I.; Abe, Y. *Applied Physics A* **2011**, *106*, DOI: 10.1007/s00339-011-6694-4.

(26) Casadio, F.; Daher, C.; Bellot-Gurlet, L. *Topics in Current Chemistry* **2016**, *374*, 62.

(27) Picollo, M.; Bacci, M.; Casini, A.; Lotti, F.; Porcinai, S.; Stefani, L. In, 2002, pp 259–265.

(28) Brunetti, B.; Miliani, C.; Rosi, F.; Doherty, B.; Monico, L.; Romani, A.; Sgamellotti, A. *Topics in current chemistry* **2016**, *374*, DOI: 10.1007/s41061-015-0008-9.

(29) Fukunaga, K.; Marcello, P. *Applied Physics A* **2010**, *100*, 591–597.

(30) Fukunaga, K., *THz Technology Applied to Cultural Heritage in Practice*; Cultural Heritage Science; Springer Japan: 2016.

(31) Ching, M. C. H.; Giovannacci, D.; Gariani, G.; Brissaud, D.; Leroux, L.; Goubard, F.; Bouquillon, A.; Bormand, M. In *Optics for Arts, Architecture, and Archaeology VI*, ed. by Pezzati, L.; Targowski, P., SPIE: 2017; Vol. 10331, pp 95 –103.

(32) Van der Snickt, G.; Legrand, S.; Slama, I.; Zuien, E.; Gruber, G.; van der Stighelen, K.; Klaassen, L.; Oberthaler, E.; Janssens, K. *Microchemical Journal* **2018**, *138*, DOI: 10.1016/j.microc.2018.01.019.

(33) Saverwyns, S.; Currie, C.; Lamas-Delgado, E. *Microchemical Journal* **2017**, *137*, DOI: 10.1016/j.microc.2017.10.008.

(34) Walczak, M.; Tarsińska-Petruk, D.; Plotek, M.; Goryl, M.; Kruk, M. *X-Ray Spectrometry* **2017**, DOI: 10.1002/xrs.2949.

(35) Alfeld, M.; Pedroso, J.; Hommes, M.; Van der Snickt, G.; Tauber, G.; Blaas, J.; Haschke, M.; Erler, K.; Dik, J.; Janssens, K. *Journal of Analytical Atomic Spectrometry* **2013**, *28*, 760–767.

(36) Legrand, S.; Vanmeert, F.; Van der Snickt, G.; Alfeld, M.; De Nolf, W.; Dik, J.; Janssens, K. *Heritage Science* **2014**, *2*, 13.

(37) Gabrieli, F.; Dooley, K.; Facini, M.; Delaney, J. *Science Advances* **2019**, *5*, eaaw7794.

(38) Delaney, J.; Zeibel, J.; Thoury, M.; Littleton, R.; Palmer, M.; Morales, K.; de la Rie, R.; Hoenigswald, A. *Applied Spectroscopy* **2010**, *64*, 584–594.

(39) Delaney, J.; Zeibel, J.; Thoury, M.; Littleton, R.; Morales, K.; Palmer, M.; de la Rie, R. *Proceedings of SPIE - The International Society for Optical Engineering* **2009**, *7391*, 2–.

(40) Iwanicka, M In Bastidas, D.; Cano, E. *Advanced Characterization Techniques, Diagnostic Tools and Evaluation Methods in Heritage Science*, 2018; Chapter 4: Optical Coherence Tomography (OCT) for Examination of Artworks.

(41) Liang, H.; Peric, B.; Hughes, M.; Podoleanu, A.; Spring, M.; Saunders, D. *Proceedings of SPIE - The International Society for Optical Engineering* **2007**, *6618*, DOI: 10.1117/12.726032.

(42) Liu, P.; Hall-Aquitania, M.; Hermens, E.; Groves, R. M. In *Optics for Arts, Architecture, and Archaeology VI*, ed. by Pezzati, L.; Targowski, P., SPIE: 2017; Vol. 10331, pp 48 –55.

(43) Alfeld, M. Development of Scanning macro-XRF for the Investigation of Historical Paintings, Ph.D. Thesis, University of Antwerp, 2013.

(44) M6 JETSTREAM Micro- XRF- Spectrometer Instrument Information Book; Bruker Nano GmbH, Berlin, 2018.

(45) M6 JETSTREAM - Overview, large sample Micro-XRF analysis - M6 JETSTREAM | Bruker Bruker Nano GmbH, https://www.bruker.com/products/x-ray-diffraction-and-elemental-analysis/micro-xrf-and-txrf/m6-jetstream/overview.html (accessed 09/09/2020).

(46) Alfeld, M.; Janssens, K. *Journal of Analytical Atomic Spectrometry* **2015**, *30*, DOI: 10.1039/C4JA00387J.

(47) Alfeld, M. datamuncher download | SourceForge.net https://sourceforge.net/projects/datamuncher/ (accessed 07/27/2020).

(48) PyMca Home ESRF - The European Synchrotron Radiation Facility, http://pymca.sourceforge.net/ (accessed 07/27/2020).

(49) Janssens, K.; Van der Snickt, G.; Vanmeert, F.; Legrand, S.; Nuyts, G.; Alfeld, M.; Monico, L.; Anaf, W.; De Nolf, W.; Vermeulen, M.; Verbeeck, J.; De Wael, K. *Topics in Current Chemistry* **2016**, *374*, DOI: 10.1007/s41061-016-0079-2.

(50) Schreiner, M.; Frühmann, B.; Jembrih-Simbuerger, D.; Linke, R. *Powder Diffraction - POWDER DIFFR* **2004**, *19*, DOI: 10.1154/1.1649963.

(51) Operation Night Watch to start at the Rijksmuseum - Press releases - Press Rijksmuseum, https://www.rijksmuseum.nl/en/press/press-releases/operation-night-watch-to-start-at-the-rijksmuseum (accessed 07/28/2020).

(52) SOC710 Series Hyperspectral Imaging Surface Optics Corporation, https://surfaceoptics.com/products/hyperspectral-imaging/soc710-portable-hyperspectral-camera/ (accessed 08/17/2020).

(53) Hyperspectral Sensors | Hyperspectral Cameras Headwall Photonics Inc., https://www.headwallphotonics.com/hyperspectral-sensors (accessed 08/17/2020).

(54) Delaney, J.; Ricciardi, P.; Glinsman, L.; Facini, M.; Thoury, M.; Palmer, M.; de la Rie, R. *Studies in Conservation* **2013**, *59*, DOI: 10.1179/2047058412Y.0000000078.

(55) Van Espen, P In Van Grieken, R.; Markowicz, A. A *Handbook of X-Ray Spectrometry, second edition*, 2002; Chapter 4: Spectrum Evaluation.

(56) Liang, H. *Applied Physics A* **2011**, *106*, DOI: 10.1007/s00339-011-6689-1.

(57) Kubelka, P.; Munk, F. *Zeitschrift für technische Physik* **1931**, 593–601.

(58) What is Kubelka-Munk? Molecular Materials Resource Center - California Institute of Technology, https://mmrc.caltech.edu/FTIR/Literature/Diff%20Refectance/Kubelka-Munk.pdf (accessed 07/29/2020).

(59) Ricciardi, P.; Delaney, J.; Facini, M.; Zeibel, J.; Marcello, P.; Lomax, S.; Loew, M. *Angewandte Chemie (International ed. in English)* **2012**, *51*, 5607–10.

(60) Dooley, k.; Coddington, J.; Krueger, J.; Conover, D.; Loew, M.; Delaney, J. *Analytical methods* **2016**, *9*, DOI: 10.1039/c6ay01795a.

(61) Ricciardi, P.; Delaney, J.; Glinsman, L.; Thoury, M.; Facini, M.; de la Rie, R. *Proceedings of SPIE - The International Society for Optical Engineering* **2009**, *7391*, DOI: 10.1117/12.827415.

(62) Rohani, N.; Pouyet, E.; Cossairt, O.; Katsaggelos, A.; Walton, M. *Angewandte Chemie* **2018**, *57*, DOI: 10.1002/anie.201805135.

(63) Gettens, R. J.; Kuhn, H.; Chase, W. T. In *Artists´ Pigments A Handbook of Their History and Characteristics*, Roy, A., Ed., 3 vols.; National Gallery of Art: Washington, 1993; Chapter Lead White.

(64) Miliani, C.; Rosi, F.; Daveri, A.; Brunetti, B. *Applied Physics A* **2012**, *106*, 296.

(65) Cucci, C.; Delaney, J.; Marcello, P. *Acc. Chem. Res.* **2016**, *49*, DOI: 10.1021/acs.accounts.6b00048.

(66) Eastaugh, N.; Walsh, V.; Chaplin, T.; Siddall, R., *The Pigment Compedium: A Dictionary of Historical Pigments*, 2004; Vol. 2004.

(67) Corbeil, M.-C.; Sirois, P. *Studies in Conservation* **2007**, *52*, 281–288.

(68) Gonzalez, V.; Cotte, M.; Wallez, G.; van Loon, A.; De Nolf, W.; Eveno, M.; Keune, K.; Noble, P.; Dik, J. *Angewandte Chemie* **2019**, DOI: 10.1002/ange.201902740.

(69) Stack Flake White (Dutch Method) Pigment Natural Pigments Inc., https://www.naturalpigments.com/stack-process-white-lead-dutch-method-pigment.html (accessed 06/03/2020).

(70) Li, D.; O'Connor, B.; Low, I.; van Riessen, A.; Toby, B. *Powder Diffraction* **2006**, *21*, 289–299.

(71) Hauff, P.; Kruse, F.; Thiry, M. *Chemical Geology - CHEM GEOL* **1990**, *84*, 267–270.

(72) 4-sided film applicator - VF2161 - TQC Sheen BV - prism type VirtualExpo Group, `https://www.directindustry.com/prod/tqc-sheen-bv/product-23214-1584715.html` (accessed 09/11/2020).

(73) Mindat.org - Mines, Minerals and More Hudson Institute of Mineralogy, `https://www.mindat.org/` (accessed 08/23/2020).

(74) Liquid Densities Engineering ToolBox, `https://www.engineeringtoolbox.com/liquids-densities-d_743.html` (accessed 08/23/2020).

(75) Alfeld, M. DataHandlerP download | SourceForge.net `https://sourceforge.net/projects/datahandlerp/` (accessed 08/15/2020).

(76) OpenCV OpenCV Team, `https://opencv.org/` (accessed 08/15/2020).

(77) Alfeld, M.; Pedetti, S.; Martinez, P.; Walter, P. *Comptes Rendus Physique* **2018**, *19*, DOI: `10.1016/j.crhy.2018.08.004`.

(78) Schoonjans, T. Home · tschoonj/xraylib Wiki · GitHub ESRF, `https://github.com/tschoonj/xraylib/wiki` (accessed 08/15/2020).

(79) Schoonjans, T.; Brunetti, A.; Golosio, B.; Sánchez del Río, M.; Solé, V.; Ferrari, C.; Vincze, L. *Engineering Structures - ENG STRUCT* **2011**, *66*, DOI: `10.1016/j.sab.2011.09.011`.

(80) De Vries, J. L.; Vrebos, B. A. R. In Van Grieken, R.; Markowicz, A. A *Handbook of X-Ray Spectrometry, second edition*, 2002; Chapter 5: Quantification of Infinitely Thick Specimens by XRF Analysis.

(81) Svane, P *Surface Coatings International Part B-coatings Transactions - SURF COAT INT PT B-COAT TRANS* **2006**, *89*, 327–331.

(82) Alfeld, M.; Wahabzada, M.; Bauckhage, C.; Kersting, K.; Wellenreuther, G.; Falkenberg, G. *Journal of Physics Conference Series* **2014**, *499*, 012013.

(83) Van Grieken, R.; Markowicz, A. A In *Handbook of X-Ray Spectrometry, second edition*, 2002; Chapter 6: Quantification in XRF Analysis of Intermediate-Thickness Samples.

Appendices

Appendix A

Areal Density Table

Sample	Thickness (µm)	Areal Density (g/cm^2)					
		YO	BV	LW	Fe	Cu	Pb
Single Layer YO	50	0.0094	0	0	0.0018	0	0
	100	0.0188	0	0	0.0036	0	0
		0.0189	0	0	0.0036	0	0
	150	0.0282	0	0	0.0055	0	0
Single Layer BV	50	0	0.0125	0	0	0.0069	0
	100	0	0.0250	0	0	0.0138	0
		0	0.0252	0	0	0.0139	0
	150	0	0.0376	0	0	0.0209	0
Single Layer LW	50	0	0	0.0255	0	0	0.0204
	100	0	0	0.0509	0	0	0.0408
		0	0	0.0516	0	0	0.0413
	150	0	0	0.0768	0	0	0.0620
Underlayer YO	50	0.0094	0	0	0.0018	0	0
	100	0.0188	0	0	0.00362	0	0
Underlayer BV	50	0	0.0125	0	0	0.0069	0
	100	0	0.0250	0	0	0.0138	0
Underlayer LW	50	0	0	0.0255	0	0	0.0204
	100	0	0	0.0509	0	0	0.0408
Overlayer YO	50	0.0094	0	0	0.0018	0	0
	100	0.0189	0	0	0.0036	0	0
Overlayer BV	50	0	0.0126	0	0	0.0070	0
	100	0	0.0252	0	0	0.0139	0
Overlayer LW	50	0	0	0.0258	0	0	0.0207
	100	0	0	0.0516	0	0	0.0413

Sample	Thickness (µm)	Areal Density (g/cm^2)					
		YO	BV	LW	Fe	Cu	Pb
95% YO, 5% BV	50	0.0090	0.0005	0	0.0017	0.0003	0
	100	0.0180	0.0010	0	0.0035	0.0006	0
	150	0.0269	0.0016	0	0.0052	0.0009	0
80% YO, 20% BV	50	0.0078	0.0022	0	0.0015	0.0012	0
	100	0.0156	0.0043	0	0.0030	0.0024	0
	150	0.0234	0.0065	0	0.0045	0.0036	0
50% YO, 50% BV	50	0.0052	0.0058	0	0.0010	0.0032	0
	100	0.0104	0.0115	0	0.0020	0.0064	0
	150	0.0156	0.0173	0	0.0030	0.0095	0
20% YO, 80% BV	50	0.0022	0.0098	0	0.0004	0.0054	0
	100	0.0044	0.0195	0	0.0009	0.0108	0
	150	0.0066	0.0293	0	0.0013	0.0162	0
5% YO, 95% BV	50	0.0006	0.0119	0	0.0001	0.0066	0
	100	0.0011	0.0239	0	0.0002	0.0132	0
	150	0.0017	0.0358	0	0.0003	0.0198	0
95% YO, 5% LW	50	0.0094	0	0.0006	0.0018	0	0.0005
	100	0.0189	0	0.0012	0.0036	0	0.0010
	150	0.0283	0	0.0018	0.0055	0	0.0014
80% YO, 20% LW	50	0.0094	0	0.0028	0.0018	0	0.0023
	100	0.0188	0	0.0057	0.0036	0	0.0045
	150	0.0281	0	0.0085	0.0054	0	0.0068
50% YO, 50% LW	50	0.0076	0	0.0092	0.0015	0	0.0074
	100	0.0153	0	0.0185	0.0029	0	0.0148
	150	0.0229	0	0.0277	0.0044	0	0.0222
20% YO, 80% LW	50	0.0038	0	0.0182	0.0007	0	0.0146
	100	0.0075	0	0.0364	0.0015	0	0.0292
	150	0.0113	0	0.0546	0.0022	0	0.0437
5% YO, 95% LW	50	0.0010	0	0.0237	0.0002	0	0.0189
	100	0.0021	0	0.0473	0.0004	0	0.0379
	150	0.0031	0	0.0710	0.0006	0	0.0568
95% BV, 5% LW	50	0	0.0125	0.0007	0	0.0069	0.0006
	100	0	0.0250	0.0014	0	0.0138	0.0011
	150	0	0.0375	0.0022	0	0.0207	0.0017
80% BV, 20% LW	50	0	0.0118	0.0032	0	0.0065	0.0026
	100	0	0.0236	0.0065	0	0.0131	0.0052
	150	0	0.0354	0.0097	0	0.0196	0.0078
50% BV, 50% LW	50	0	0.0090	0.0098	0	0.0050	0.0079
	100	0	0.0180	0.0197	0	0.0099	0.0157

Sample	Thickness (µm)	Areal Density (g/cm^2)					
		YO	BV	LW	Fe	Cu	Pb
50% BV, 50% LW	150	0	0.0270	0.0295	0	0.0149	0.0236
20% BV, 80% LW	50	0	0.0042	0.0185	0	0.0023	0.0149
	100	0	0.0085	0.0371	0	0.0047	0.0297
	150	0	0.0127	0.0556	0	0.0070	0.0446
5% BV, 95% LW	50	0	0.0011	0.0237	0	0.0006	0.0190
	100	0	0.0023	0.0474	0	0.0013	0.0379
	150	0	0.0034	0.0710	0	0.0019	0.0569

Appendix B

XRF Quantification Results

Fluorescence Line	Mixture	Theoretical Composition (%)	Calculated Composition (%)	Error (%)
Fe-Kα	YO/LW	95	95.00	0.00
		80	99.66	19.66
		50	49.96	0.04
		20	16.57	3.43
		05	04.28	0.72
	YO/BV	95	95.00	0.00
		80	79.29	0.71
		50	53.83	3.83
		20	21.48	1.48
		05	05.59	0.59
Fe-Kβ	YO/LW	95	95.00	0.00
		80	88.16	8.16
		50	45.95	4.05
		20	20.16	0.16
		05	07.05	2.05
	YO/BV	95	95.00	0.00
		80	77.87	2.13
		50	56.30	6.30
		20	22.64	2.64
		05	07.73	2.73
Cu-Kα	BV/LW	95	95.00	0.00
		80	159.17	79.17
		50	162.09	112.09
		20	83.28	63.28
		05	25.32	20.32

Fluorescence Line	Mixture	Theoretical Composition (%)	Calculated Composition (%)	Error (%)
Cu-Kα	YO/BV	95	95.00	0.00
		80	89.50	9.50
		50	69.54	19.54
		20	34.37	14.37
		05	11.43	6.43
Cu-Kβ	BV/LW	95	95.00	0.00
		80	167.92	87.92
		50	181.80	130.80
		20	98.35	78.35
		05	32.59	27.59
	YO/BV	95	95.00	0.00
		80	89.76	9.76
		50	70.92	20.92
		20	33.51	13.51
		05	10.12	5.12
Pb-Lα	YO/LW	95	95.00	0.00
		80	96.07	16.07
		50	69.04	19.04
		20	26.08	6.08
		05	10.97	5.97
	BV/LW	95	95.00	0.00
		80	79.43	0.57
		50	45.72	4.28
		20	13.03	6.97
		05	01.83	3.17
Pb-Lβ	YO/LW	95	95.00	0.00
		80	99.57	19.57
		50	69.10	19.10
		20	23.98	3.98
		05	09.51	4.51
	BV/LW	95	95.00	0.00
		80	81.29	1.29
		50	46.50	3.50
		20	13.05	6.95
		05	01.90	3.10
Pb-Lγ	YO/LW	95	95.00	0.00
		80	93.98	13.98
		50	68.75	18.75

Fluorescence Line	Mixture	Theoretical Composition (%)	Calculated Composition (%)	Error (%)
Pb-Lγ	YO/LW	20	25.33	5.33
		05	06.47	1.47
	BV/LW	95	95.00	0.00
		80	80.85	0.85
		50	45.84	4.16
		20	12.10	7.90
		05	02.59	2.41
Pb-M	YO/LW	95	95.00	0.00
		80	81.56	1.56
		50	50.76	0.76
		20	17.63	2.37
		05	06.03	1.03
	BV/LW	95	95.00	0.00
		80	79.12	0.88
		50	47.84	2.16
		20	15.60	4.40
		05	03.68	1.32

Appendix C

Dead Time Corrected XRF Quantification Results

Fluorescence Line	Mixture	Theoretical Composition (%)	Calculated Composition (%)	Error (%)
Fe-Kα	YO/LW	95	95.00	0.00
		80	91.80	11.80
		50	47.09	2.91
		20	16.32	3.68
		05	04.19	0.81
	YO/BV	95	95.00	0.00
		80	87.92	7.92
		50	83.04	33.04
		20	39.91	19.91
		05	11.41	6.41
Fe-Kβ	YO/LW	95	95.00	0.00
		80	77.64	2.36
		50	41.66	8.34
		20	19.79	0.21
		05	06.63	1.63
	YO/BV	95	95.00	0.00
		80	86.27	6.27
		50	91.86	41.86
		20	44.76	24.76
		05	15.61	10.11
Cu-Kα	BV/LW	95	95.00	0.00
		80	168.94	88.94
		50	117.15	67.15

Fluorescence Line	Mixture	Theoretical Composition (%)	Calculated Composition (%)	Error (%)
Cu-Kα	BV/LW	20	52.93	32.93
		05	15.33	10.33
	YO/BV	95	95.00	0.00
		80	80.76	0.76
		50	52.83	2.83
		20	18.76	1.24
		05	05.64	0.64
Cu-Kβ	BV/LW	95	95.00	0.00
		80	170.99	90.99
		50	132.72	72.72
		20	62.74	42.74
		05	19.73	14.73
	YO/BV	95	95.00	0.00
		80	81.51	1.51
		50	55.91	5.91
		20	18.13	1.87
		05	04.97	0.03
Pb-Lα	YO/LW	95	95.00	0.00
		80	98.75	18.75
		50	68.52	18.52
		20	24.99	4.99
		05	12.46	7.46
	BV/LW	95	95.00	0.00
		80	83.55	3.55
		50	54.30	4.30
		20	20.28	0.28
		05	02.97	2.03
Pb-Lβ	YO/LW	95	95.00	0.00
		80	103.46	23.46
		50	69.30	19.30
		20	22.97	2.97
		05	10.59	5.59
	BV/LW	95	95.00	0.00
		80	85.85	5.85
		50	56.02	6.02
		20	20.79	0.79
		05	02.91	2.09
Pb-Lγ	YO/LW	95	95.00	0.00

Fluorescence Line	Mixture	Theoretical Composition (%)	Calculated Composition (%)	Error (%)
Pb-Lγ	YO/LW	80	95.99	15.99
		50	67.61	17.61
		20	23.86	3.86
		05	06.26	1.26
	BV/LW	95	95.00	0.00
		80	85.04	5.04
		50	54.52	4.52
		20	17.45	2.55
		05	03.65	1.35
Pb-M	YO/LW	95	95.00	0.00
		80	80.17	0.17
		50	48.21	1.79
		20	16.18	3.82
		05	05.56	0.56
	BV/LW	95	95.00	0.00
		80	81.27	1.27
		50	53.55	3.55
		20	21.25	1.25
		05	05.55	0.55